Fall 12-18-2020

Polymeric Drug Delivery Systems for Cancer Therapy and Radionuclide Decorporation

Sameer A. Alshehri
University of Nebraska Medical Center

POLYMERIC DRUG DELIVERY SYSTEMS FOR CANCER THERAPY AND RADIONUCLIDE DECORPORATION

by

Sameer Alshehri

A DISSERTATION

Presented to the Faculty
of the University of Nebraska Graduate College
in Partial Fulfillment of the Requirements
For the Degree of Doctor of Philosophy

Pharmaceutical Sciences
Graduate Program

Under the Supervision of Professor Jered C. Garrison

University of Nebraska Medical Center

Omaha, Nebraska

December, 2020

Supervisory Committee:

Rongshi Li, Ph.D Dong Wang, Ph.D

Joseph A. Vetro, Ph.D. Maneesh Jain, Ph.

ACKNOWLEDGMENTS

First of all, this work could not have been finished without the help, support, and guidance of many people.

I would like to express my sincere appreciation to my advisor Dr. Jered Garrison, for the mentoring and continuous support of my Ph.D. study, for his patience, motivation, and immense knowledge. I could never have imagined having a better advisor and mentor for my Ph.D. study. Beside my mentor, I would like to convey my genuine thanks and appreciations to the rest of my dissertation committee members; Dr. Rongshi Li, Dr. Dong Wang, Dr. Joseph A. Vetro, and Dr. Maneesh Jain for their time, their encouragements, insightful comments to improve my work, and hard questions that force me to think critically.

Beside my mentor and my committee, I would like to express gratitude to Dr. Shana Garrison for their great assistance on manuscript preparation. I would also like to thank Dr. Wei Fan and Dr. Wenting Zhang for their valuable guidance and support on my Ph.D. Journey. I also would like to send many thanks to all my friends, classmates, and lab mates for their endless support and excellent company over the previous five and a half years.

Special thanks to the government of Saudi Arabia and Taif University for their supports, including monthly salaries, health insurance, and tickets back and forth. I have been truly touched by their generosity, and I hope to one-day give back just as they have.

Finally, I would like to dedicate this work to parents Mr. Amer and Mrs. Salmah, my wife, Mrs. Asrar, and my adorable, loving boy Badr for their endless love and continued support.

POLYMERIC DRUG DELIVERY SYSTEMS FOR CANCER THERAPY AND RADIONUCLIDE DECORPORATION

Sameer Alshehri

University of Nebraska, 2020

Supervisor: Jered C. Garrison, Ph.D.

ABSTRACT

The main objective of this body of work is to develop polymeric drug delivery systems for cancer radiotherapy and the decorporation of radiological materials. The polymeric systems for radiotherapy were evaluated *in vitro* and *in vivo* (in normal, prostate, and ovarian cancer mice models). The polymeric system for radionuclide decorporation was also evaluated *in vitro* and in a normal mouse model. Due to its attractive properties, the N-(2-Hydroxypropyl) methacrylamide (HPMA) copolymer was utilized as the main carrier for the developed systems.

Chapter 1 provides an overview of prostate and ovarian cancer, targeted radiopharmaceuticals, nanomedicine-based drug delivery for cancer, HPMA copolymers, and decorporation agents of radiological materials.

In chapter 2, we aimed to develop targeted HPMA copolymers to improve prostate cancer treatment. HPMA copolymers were modified with bombesin (BBN) peptide analogs to target the gastrin-releasing peptide receptor (GRPR) that is overexpressed in several tumors, including prostate cancer. Based on varying the content and charge, a total of ten BBN-HPMA copolymers were synthesized and evaluated in GRPR-overexpressing prostate cancer cell line (PC-3), and the biodistribution profile of the optimized copolymers was evaluated in a normal CF-1 mouse model. The *in vitro* results showed enhanced internalization via GRPR targeting was charge- and BBN density-dependent. While the negative and zwitterionic conjugates showed low PC-3 uptake values, the positively-charged BBN-polymeric conjugates revealed a direct relationship between

the extent of cellular internalization and BBN-incorporation density. *In vivo* studies of the positively-charged copolymers resulted in rapid blood clearance by the mononuclear phagocyte system (MPS)-associated tissues. Further optimization to avoid rapid MPS recognition is needed in the future.

In chapter 3, we aimed to improve the radiotherapy of ovarian cancer by developing a polymeric delivery system, using HPMA copolymer as a carrier, that overcomes the current drawbacks of radiolabeled nanomedicine (e.g., retention in MPS-associated tissues and long circulation times needed for tumor targeting). The new system (MP-90-TCO-C) combines two strategies in one system. The first strategy is to enhance the clearance of retained large polymers in the MPS-associated tissues via biodegradation, by cathepsin S enzyme (Cat S) that is abundantly expressed in these tissues, into small and easily cleared fragments from the body. The second strategy is based on employing bioorthogonal *in vivo* chemistry between a trans-cyclooctene- (TCO) modified polymer (MP-90-TCO-C) and a tetrazine- (TZ) based radiotracer. Kinetic and *in vitro* Cat S studies were evaluated. *In vivo* studies were performed using two ovarian cancer and a normal CF-1 mouse models. The kinetic studies revealed ultra-fast reactions between MP-90-TCO-C, and the TZ-radiotracer while MP-90-TCO-C was also found to be cleaved *in vitro* by Cat S. The *in vivo* studies showed biodegradation of the copolymer in the CF-1 mouse model with excellent *in vivo* TCO/TZ reactivity in ovarian cancer models with improved tumor to non-target ratios observed. These results show the feasibility of this approach to enhance the treatment of ovarian cancer.

In chapter 4, we aimed to design a polymeric system that can be suitable for prophylactic applications to reduce the exposure to radioactive actinides, which can occur in case of accidental internal contamination. DTPA is approved for actinide decorporation after exposure, but due to its short half-life, DTPA is not ideal for prophylactic applications. To overcome this drawback, we developed a DTPA-based polymeric system (P-DTPA) based on an HPMA copolymer. We

evaluated its decorporation efficacy using an actinide model *in vitro* and in a normal CF-1 mouse model under prophylactic settings. The *in vitro* results showed the tolerability of P-DTPA and the ability to chelate the actinide model in the presence of competing biological metals. The *in vivo* results showed the superiority of P-DTPA over DTPA in enhancing the excretion of the radioactive material. This enhanced decorporation effect is mainly attributed to the longer circulation time of P-DTPA compared to DTPA.

In chapter 5, all results from the three projects will be summarized, and future research directions will be provided.

TABLE OF CONTENT

1 Chapter 1. Introduction 1
1.1 Prostate cancer 1
1.2 Ovarian Cancer 3
1.3 Imaging and treatment of cancer using targeted radiopharmaceuticals 7
1.4 Nanomedicine-based drug delivery for cancer 9
1.5 Decorporation in the case of the release of radiological materials 35
2 Chapter 2. *In Vitro* Evaluation and Biodistribution Studies of HPMA Copolymers Targeting the Gastrin Releasing Peptide Receptor in Prostate Cancer 39
2.1 Introduction 39
2.2 Materials and methods 41
2.3 Results 51
2.4 Discussion 70
3 Chapter 3. Bioorthogonal pretargeting of multi-block cathepsin S-cleavable HPMA copolymers: *In vitro* and *in vivo* evaluations for improved ovarian cancer treatment 74
3.1 Introduction 74
3.2 Materials and methods 77
3.3 Results and discussion 90
3.4 Conclusion 134
4 Chapter 4. Prophylactic Chelation Therapy Using DTPA-HPMA Copolymer (P-DTPA): *In vitro* and *In vivo* Evaluations 135
4.1 Introduction 135
4.2 Materials and methods 137
4.3 Results and discussion 143
4.4 Conclusion 161
5 Chapter 5. Summary and future directions 162
5.1 Summary 162
5.2 Future directions 165

LIST OF FIGURES

Figure 1.1 The proposed reaction mechanism between the tetrazine and dienophile. 16
Figure 1.2 Photochemical isomerization of Cis-cyclooct-4-enol to provide the two possible TCO diastereomers. 17
Figure 1.3 Illustration for steps of in vivo IEDDA chemistry using antibody. 19
Figure 1.4 Small animal SPECT/CT imaging colon carcinoma animal model preinjected with TCO-modified CC49 monoclonal antibody followed 72 h later by ^{111}In-labeled TZ probe. 20
Figure 1.5 Example for the synthesis of a multifunctional HPMA copolymer intermediate for further post-modification. 25
Figure 2.1 Structures of synthesized peptides (BBN-RR, D-BBN-RR, and BBN-EE). 53
Figure 2.2 Schematic representation of A) RAFT polymerization, B) Thiol deprotection, C) BBN peptide conjugation, D) Deprotection of DOTA-tris(tBu) and E) radiolabeling with ^{177}Lu. 56
Figure 2.3 MS spectra of the synthesized BBN peptides. 58
Figure 2.4 ^{1}H-NMR spectra of HPMA-SS and HPMA-SH 1. 60
Figure 2.5 ^{19}F-NMR spectra of both BBN-RR and P-RR-3. 61
Figure 2.6 Cellular internalization of positive BBN-HPMA conjugates (A), negative BBN-HPMA conjugates (B), zwitterionic BBN-HPMA conjugates (C), and GRPR blocking experiments after 1 h (with or without BBN-Anta) (D) 64
Figure 2.7 Confocal microscopy images of P-D-RR-3 and P-RR-3 66
Figure 2.8 Biodistribution profiles (in selected organs) of P-RR-1, P-RR-2, P-D-RR-3, P-RR-3, and P-RR-4 after 4 h in normal mice. 68
Figure 3.1 Synthesis and structures of TCO-linkers. 92
Figure 3.2 ^{1}H-NMR and ^{13}C-NMR spectra of CCO, TCO major, and TCO minor. 93
Figure 3.3 ^{1}H-NMR, ^{19}F-NMR, and MS spectra of Fmoc-D-Asp(OtBu)-NH-F_3 and MS spectrum of Fmoc-D-Asp(OH)-NH-F_3 94
Figure 3.4 MS spectra of linker-B and TCO-B 95
Figure 3.5 MS spectra of linker-C, TCO-C, and TCO-C-TFP and ^{19}F-NMR spectrum of TCO-C 96
Figure 3.6 Synthesis of DTOA-TZ probes. 98
Figure 3.7 Profiles of intermediates for the synthesis of DOTA-TZ probes. 99
Figure 3.8 ^{1}H-NMR and MS spectra of DOTA-TZ 1 and MS spectrum of ^{nat}Lu-TZ 1. 100
Figure 3.9 ^{1}H-NMR, MS, ^{13}C-NMR spectra of DOTA-TZ 2 and MS spectrum of ^{nat}Lu-DOTA-TZ 2. 101
Figure 3.10 Schematic representations for the synthesis of non-cleavable and cleavable TCO-HPMA copolymers. 103
Figure 3.11 ^{1}H-NMR spectra of NP-82 and NP-TCO-A, and ^{19}F-NMR of NP-TCO-C. 106
Figure 3.12 Synthesis and MS spectrum of CTA 2 and MS spectrum of Cat S cleavable peptidic linker (CL) 108
Figure 3.13 SEC-HPLC chromatograms of MP-90 and MP-90-TCO. 109
Figure 3.14 Synthesis of DP-TZ. 111
Figure 3.15 Radio-HPLC chromatograms for the reactions between TCO-C and ^{177}Lu-DOTA-T 1 and ^{177}Lu-DOTA-TZ 2, and profiles of kinetic studies between DOTA-TZ probes and TCO-linkers / TCO-HPMA copolymers.. 117
Figure 3.16 LC/MS profile for the reaction between TCO-C and DOTA-TZ 1. 118
Figure 3.17 The selected region of interest (ROI) used for the dual-radioisotope studies. 130
Figure 3.18 Effect of DP-TZ on tumor / normal tissues (T/NT) ratios. 133

Figure 4.1 ^{1}H-NMR and MS spectra of APMA-DTPA and ^{1}H-NMR spectrum of P-DTPA 146
Figure 4.2 Selectivity study profiles of DTPA and P-DTPA after 15 mins incubation with 1X and 10X solutions containing ^{177}LuCl3. 150
Figure 4.3 Cell viability profiles of DTPA and P-DTPA after two days incubation with HUVEC cell line..... 153
Figure 4.4 Schematic representation of *in vivo* studies and the excretion profiles. 157
Figure 4.5 Total ^{177}Lu body content and distribution after 14 and 15 days of ^{177}Lu contamination for the 6-h and 24-h prophylactic treatments, respectively. 160

LIST OF TABLES

Table 1.1 Examples of marketed polymer-drug conjugates..... 23
Table 1.2 HPMA-drug conjugates in clinical trials 34
Table 2.1 Feed BBN peptide amount for BBN-HPMA conjugation reaction 47
Table 2.2 Mass spectrometric identification and IC_{50} values of the peptides 57
Table 2.3 Characteristics of HPMA copolymers 59
Table 2.4 Biodistribution of BBN-HPMA conjugates in CF-1 female mice after 4 h..... 69
Table 3.1 Characteristics of TCO-HPMA copolymers and their polymeric precursors 104
Table 3.2 The characteristics of kinetic studies for the reactions between TCO-compounds and DOTA-TZ probes..... 116
Table 3.3 Biodistribution of TCO-HPMA copolymers in normal (CF-1) mice..... 129
Table 3.4 Biodistribution and TCO/TZ reactivity profiles of selected TCO-HPMA copolymers and biodistribution of ^{177}Lu-DOTA-TZ 2in NOD-SCID mice (%ID/g)..... 131
Table 3.5 Biodistribution and *in vivo* TCO/TZ chemistry profiles of the capped TCO-HPMA copolymers in SCID mice based on dual-radioisotope study (111In-TCO-HPMA copolymer and ^{177}Lu-DOTA-TZ 2 probe) 132
Table 4.1 Characteristics of P-DTPA 147

LIST OF ABBREVIATIONS

AIBN	2,2′-Azobis(2-methylpropionitrile)
APMA	N-(3-aminopropyl)methacrylamide
APMA-DTPA	APMA reacted with p-SCN-Bn-DTPA
BBN	Bombesin
BBN-EE	Bombesin peptide modified with two negatively charged amino acids
BBN-RR	Bombesin peptide modified with two positively charged amino acids
CL	Cathepsin S susceptible linker
CTA	Chain transfer agent
DOTA	1,4,7,10-tetraazacyclododecane-1,4,7,10-tetraacetic acid
DTPA	Diethylenetriaminepentaacetic acid calcium trisodium salt
FITC	Fluorescein isothiocyanate
GRPR	Gastrin-Releasing Peptide Receptor
HPMA	N-(2-Hydroxypropyl) methacrylamide
IC_{50}	Half maximal inhibitory concentration
In	Indium
Lu	Lutetium
NHS	N-Hydroxysuccinimide
NMR	Nuclear magnetic resonance
NOD	Non-Obese Diabetic
OVCAR-3	Ovarian adenocarcinoma cell line
PEG	Polyethylene glycol
PC-3	Prostate cancer cell line
P-D-RR	HPMA copolymer modified with D-BBN-RR
P-DTPA	HPMA copolymer contains APMA-DTPA

P-EE	HPMA copolymer modified with BBN-EE
P-RR	HPMA copolymer modified with BBN-RR
P-RREE	HPMA copolymer modified with BBN-RR and BBN-EE
p-SCN-Bn-DTPA	S-2-(4-Isothiocyanatobenzyl)-diethylenetriamine pentaacetic acid
SCID	Severely combined immunodeficient
SEC	Size exclusion chromatography
TCO	Trans-cyclooctene
TFP	2,3,5,6-tetrafluorophenyl ester
TZ	Tetrazine

1 Chapter 1. Introduction

1.1 Prostate cancer

According to the American Cancer Society, prostate cancer is the most common type of cancer diagnosed (except for certain skin cancers) in men in the United States (US). (1). More than 191,000 and 33,000 new prostate cancer cases and deaths are expected in the US by the end of this year. The 5-year relative survival rate for men diagnosed with early stage disease is nearly 100%, but this percentage drops to nearly 31% in patients diagnosed at later stages of the disease.

1.1.1 Diagnosis of prostate cancer

Unfortunately with prostate cancer, there are no obvious symptoms associated with the disease in the early stages. However, urinary (e.g., hesitancy and retention) and systemic symptoms (e.g., fatigue and bone pain) are observed in patients with advanced disease (2). Fortunately, most prostate cancer cases are diagnosed at the early stage through routine screening via a prostate antigen test (PSA) or digital rectal examination (3). PSA is a glycoprotein produced by the epithelial cells of normal prostate and prostatic cancer tissue (4). Although it is not definitive, a high serum level of PSA (10 ng/mL) indicates a more likely (> 50%) issue of prostate cancer presentation (3). A prostate biopsy is necessary to confirm the diagnosis.

The American Joint Committee on Cancer (AJCC) TNM system is the standard staging system for staging prostate cancer (5). In cases of high risk for metastasis, conventional bone scans using ^{99m}technetium methylene diphosphonate and cross-sectional body imaging (computed tomography (CT) or magnetic resonance imaging (MRI)) are recommended (3). These imaging modalities have limited sensitivity in detecting small malignant lesions (3). Therefore, there is a growing interest in using highly sensitive nuclear medicine imaging modalities to detect disease recurrence via the employment of radiotracers (6). ^{11}C-choline and ^{18}F-fluciclovine (a non-natural

amino acid) radiotracers are examples of recently approved agents by the US Food and Drug Administration (FDA) for detecting the recurrence of prostate disease (6). The sensitivity and specificity of the currently approved drugs vary depending on several factors, including PSA level and the location of the tumor (lymph nodes versus bone). For example, the sensitivity of ^{11}C-choline ranges from 38% to 98%, and its specificity ranges from 50% to 100% (3). Interestingly, a recent report showed that the incidence of diagnosis with metastatic prostate cancer in the US was increased between 2004 to 2013 (7). Therefore, the development of improved screening and diagnostic tests are needed.

1.1.2 Treatment of prostate cancer

The treatment options for prostate cancer depends on the stage at which diagnosis occurs (localized versus distant). For localized cancer cases (low, intermediate, and high risk), the options include active surveillance, radical prostatectomy, and radiotherapy (8). Classification of patients into the risk groups is dependent on PSA levels and Gleason score (9). Low-risk patients under active surveillance undergo monitoring for disease progression with the intent to cure. However, intermediate- and high-risk patients undergo either radical prostatectomy or radiotherapy treatments (9). Reports indicated no difference in the mortality rates due to prostate cancer between patients who underwent radical prostatectomy or radiotherapy (3). External-beam radiation therapy (EBRT) is the standard approach for radiotherapy in prostate patients (9). Dose-escalated intensity-modulated radiation therapy (IMRT) is the most common technique for delivering EBRT. Unlike conventional EBRT techniques, IMRT involves the delivery of multiple radiation beams from different angles to intersect within the target volume. This technique is associated with a reduction in the toxicities of adjacent tissues (9). However, short- and long-term urinary incontinence, bowel toxicity, and erectile dysfunction are still commonly observed following radiotherapy. In addition, treatment of metastatic disease using EBRT techniques remains a major challenge. Alternative

strategies (e.g., radiopharmaceuticals) targeting the tumor cells and other cells in the tumor microenvironment in the metastatic disease are needed (10, 11).

The standard treatment strategy of metastatic prostate cancer includes androgen deprivation therapy (e.g., luteinizing hormone-releasing hormone (LHRH) therapy) (3, 8). However, metastatic prostate cancer patients, eventually, become castration-resistant necessitating the progression to other types of disease management strategies (8). Radiotherapy is generally not recommended for metastatic prostate cancer patients. A recent clinical trial showed that performing radiotherapy to the prostate of newly diagnosed metastatic patients failed to improve overall survival rates (12). Other available treatment options mainly include chemotherapeutic and hormonal agents. For example, docetaxel is a commonly prescribed chemotherapeutic drug for metastatic prostate cancer patients (8). Docetaxel is an antimicrotubular agent that acts by stabilizing the mitotic spindle during mitosis and interphase, which leads to mitosis and cell proliferation arrest. Examples of hormonal agents include abiraterone and enzalutamide that have gained FDA approval for the treatment of metastatic castration-resistant prostate patients in 2011 and 2012, respectively (8). However, despite these recent efforts, metastatic prostate cancer is still considered a non-curable disease with the need for the development of new and innovative treatment strategies.

1.2 Ovarian Cancer

According to the American Cancer Society, ovarian cancer accounts for the highest number of deaths among gynecological tumors and ranks fifth in death-related cancer among American women (1). It is estimated that 21,750 individuals will be diagnosed, and 13,940 patients will die in the US in 2020 due to ovarian cancer (1). The 5-year relative survival rate for women diagnosed at the localized stage is about 92% (13). However, this rate drops to nearly 30% with a metastatic stage diagnosis. Unfortunately, nearly 58% of ovarian cancer patients are diagnosed with metastatic disease.

Based on the cell origin, ovarian cancer is categorized into either epithelial, germ cell, or stromal tumor types. Epithelial ovarian cancer (EOC) is the most common type, and it accounts for nearly 90% of cases (14). The majority of EOC patients are diagnosed at the advanced stages with only 20% of patients being diagnosed with early stage disease (15). The 5-year relative survival rate of EOC patients is about 70% if the disease is detected at the early stages; this rate drops to nearly 35% in patients diagnosed at the advanced stages. EOC is a heterogeneous disease, which is subclassified into high-grade serous carcinoma (70%), endometrioid (10%), clear-cell (10%), mucinous (3%), and low-grade serous carcinomas (<5%) (16). These statistics highlight the lack of effective screening tests for the disease at the early stages and the need for alternative therapeutic agents for the patients at the advanced stages.

1.2.1 Diagnosis of ovarian cancer

There are no specific symptoms associated with ovarian cancer (14). Patients may experience pelvic and abdominal pain, abdominal bloating, and other nonspecific gastrointestinal symptoms (e.g., nausea and vomiting). A study reported that ovarian cancer patients might experience these symptoms for 12 months before diagnosis (17). Currently, the only available screening tests include performing a transvaginal ultrasound and a blood test for the ovarian cancer marker CA125 (mucin 16) (18).The transvaginal ultrasound is not specific for the detection of cancer, and the majority of masses found by transvaginal ultrasound are not malignant (19). Also, an increase in the blood levels of the CA125 marker is observed in only 50% of patients with stage I ovarian cancer (20). A randomized controlled trial of over 202,000 women divided into three screening test groups (CA125 versus transvaginal ultrasound versus no screening test) was performed to investigate the effects of early detection by screening on the resultant mortality rates. After 11 years of follow-up, there was found to be no difference in the mortality rates between the three groups (21). A follow-up trial (NCT00058032) is currently ongoing to investigate the late

benefits (7–14 years after an index screening event) of the screening tests (CA125 and transvaginal ultrasound) in postmenopausal women because of the stage shift of the cancer.

The International Federation of Obstetricians and Gynecologists (FIGO) differentiates ovarian cancer based on surgical-pathological findings into four stages (22). Stage I represents confined tumor in the ovaries. Stage II represents when tumor involves one/both ovaries with pelvic extension or primary peritoneal cancer. Stage III represents when tumor spreads to the peritoneum outside the pelvis and/or metastasis to the retroperitoneal lymph nodes. Stage IV represents when there is distant metastasis. Pre-operative imaging (at the primary disease site) is also used to identify unresectable or difficult to resect disease, which employs CT, positron emission tomography (PET)/CT and MRI (23). PET/CT has a major role in N and M staging, with a limited role in T staging (23).

1.2.2 Treatment of ovarian cancer

The treatment of newly diagnosed ovarian cancer patients depends on the pathological stage determined at diagnosis (24). The available options for treatment include chemotherapy, radiation therapy, and surgery. The standard course of treatment is to perform surgical tumor debulking, followed by chemotherapy (18). Neoadjuvant chemotherapy can also be used, although its benefits are controversial (25). The chemotherapeutic agents are administered intraperitoneally (i.p.), intravenously (i.v.), or both (mainly when the disease is already spread to the peritoneal cavity) (25). One of the most frequently prescribed chemotherapeutics is a platinum agent (carboplatin or cisplatin) as a monotherapy or in combination with a taxane (e.g., paclitaxel). Platinum drugs act by forming DNA crosslinks with biomolecules such as proteins and lipids that disrupt the cellular function of DNA, leading to the apoptosis of cancer cells (26). The majority of ovarian cancer patients (70 – 80%) treated with a platinum-based therapy as a first-line chemotherapy show response with an improved overall survival rate at both the localized and metastatic stages (27). However, some patients are initially platinum-resistant, and most platinum-

sensitive patients will eventually acquire platinum-resistance (26). Multiple mechanisms have been proposed for the development of platinum resistance. These mechanisms are found to involve transporters (i.e., interfere with the transport of platinum drugs into the cancer cell), on-target (repair mechanisms), post-target, and off-target (signaling pathways leading to interfering with the apoptosis caused by platinum drugs) (26). Alternative chemotherapeutics include the use of doxorubicin (e.g., pegylated liposomal formulation) and antiangiogenic agents (e.g., bevacizumab) (25). However, despite the initial response after chemotherapy, most patients develop a recurrence of the disease (28). In the past six years, three poly-ADP-ribose polymerase (PARP) inhibitors (olaparib, niraparib, and rucaparib) have gained approval from the FDA (29). These agents act by trapping the PARP enzymes at the damaged DNA leading to an increase impairment of already deficient DNA repair mechanisms (due to gene mutations in BRCA and homologous recombination deficiency (HRD)) which are present in nearly 50% of ovarian cancer patients (15). Currently, PARP inhibitors are only approved for patients with advanced stages, and their efficacy as a first-line therapy is still under evaluation (29). Unfortunately, multiple acquired drug resistance mechanisms have already been associated with the use of PARP inhibitors, including ABCB1 fusions and BRCA mutation reversions (15). Therefore, alternative strategies to improve the clinical outcomes of ovarian cancer patients are needed.

1.2.3 Radiotherapy as a treatment option for ovarian cancer

The use of radiotherapy in patients as a treatment strategy was frequently used three decades ago in adjuvant and consolidation settings (18, 30). However, over time, it has been replaced with more effective chemotherapy-based strategies (platinums and taxanes) due to the consistently high toxicity profiles and contradictory antitumor efficacy results reported in clinical trials (31). Whole abdomen irradiation (WAI) via conventional external beam was the standard type of radiotherapy for ovarian cancer. Its acute (e.g., gastrointestinal and hematological) and long-term (e.g., liver damage and pneumonitis) toxicities caused treatment interruptions.

Performing WAI using a recent technique, IMRT, may provide an effective alternative radiotherapy strategy due to its benefits in dose homogeneity and sparing organs at risk (31). A recent study evaluating WAI via IMRT in advanced ovarian cancer patients in the consolidation setting (following chemotherapy) showed no grade 4 toxicities and no treatment interruptions (32). While these results indicate an enhancement in the safety profiles of WAI by IMRT, the efficacy in such patients is yet to be determined.

1.3 Imaging and treatment of cancer using targeted radiopharmaceuticals

1.3.1 Imaging

Imaging modalities are valuable in cancer for the early detection, development of appropriate treatment strategies, and monitoring the response of these treatments. The commonly used modalities are based on ultrasound, CT, MRI, PET, and single photon emission computed tomography (SPECT) (33, 34). PET (using positron emitting radionuclides) and SPECT (using gamma emitting radionuclides) offer advantages over the other modalities because of their high sensitivity and accuracy. A targeted radiopharmaceutical consists of a tumor targeting vehicle and a radionuclide. After the injection of a targeted radiopharmaceutical, PET and SPECT provide information about the distribution of the tracer, which reflects the tumor locations. Therefore, effective PET or SPECT imaging is limited by the ability of the radiotracer to distinguish between the malignant and non-malignant cells. While examples of radionuclides for PET imaging include ^{64}Cu, ^{68}Ga, and ^{18}F, radionuclides for SPECT imaging include ^{123}I, ^{99m}TC, and ^{111}In (35). An example of a targeted radiopharmaceutical that was approved recently for PET imaging is ^{68}Ga-DOTA-TOC (36). It binds to somatostatin receptor, which is overexpressed in some neuroendocrine tumors (36). Therefore, its approval is for PET imaging of somatostatin receptor positive gastroenteropancreatic neuroendocrine tumors. Emerging targeted radiotracers are based on exploiting the overexpression of biomarkers found on cancer cells. For instance, targeting the

overexpression of the $\alpha_v\beta_3$-integrin receptor, gastrin-releasing peptide receptor (GRPR), folate receptor, and prostate-specific membrane antigen (PSMA) has shown promise for cancer diagnosis (37-39).

1.3.2 Therapy

It is estimated that nearly 50% of cancer patients receive radiotherapy as a monotherapy or in combination with other strategies (e.g., chemotherapy and surgery) (34). The ionizing radiation effect includes damaging the tissue structure, ionization of cellular water, generation of free radicals, and irreversible breaks of mitochondrial and nuclear DNA (34). EBRT is the most common type of radiotherapy and involves the delivery of radiation into tumor tissues via an external source using a linear accelerator (40). The other commonly used radiotherapy type is brachytherapy, which involves surgically installing a radioactive source (e.g., radioactive wires and seeds) internally in close proximity to tumor tissues. Recent advances in radiotherapy have led to the introduction of new technologies that include intensity-modulated radiotherapy and image-guided radiotherapy (40). Despite these ongoing efforts, the inability to accurately target the metastatic disease and the resulting toxicity to healthy tissues (especially the organs at risk) remain significant challenges. The degree of toxicity depends mainly on the site of radiotherapy (40). For example, radiotherapy at the pelvis region for the treatment of reproductive cancers has been shown to cause male infertility and pre-term birth in females (40). Another example is radiotherapy for the treatment of brain tumors directed at the central nervous system which showed cognitive and neurosensory impairments (40).

The development of targeted radiotherapeutics for cancer therapy has been an active area of research (41). Similar to a targeted radiotracer, targeted radiotherapeutics consist of a radionuclide and a targeting vector (e.g., peptide, or antibody) that specifically binds to cells or extracellular targets in the tumor microenvironment. As with any radiotherapeutic approach, the objective for the development of targeted radiotherapeutics is to deliver a high radiation dose to the

tumor while limiting radiotoxicities to healthy cells, especially for tumors that are difficult to surgically excise or irradiate by conventional radiation such as metastatic tumors. Numerous clinical trials are currently under evaluation using targeted radiotherapeutics that bind to tumor cells (41-44). These efforts have led to the approval of two radio-immunotherapeutics, Bexxar® (^{131}I) and Zevalin® (^{90}Y) based on a monoclonal antibody that binds to the CD20 antigen, which is explicitly expressed by B cells (45). Nearly 85% of lymphomas are derived from B-cells (45). Although these two drugs were approved for the treatment of non-Hodgkin's lymphoma, their use in the clinic remains limited due to problems related to therapeutic (e.g., hematological toxicities) and commercial reasons (46). In 2018, the FDA approved the first peptide-based radiotherapeutic (^{177}Lu-dotatate) to treat patients with somatostatin-positive gastroenteropancreatic neuroendocrine tumors (47). Later, in this chapter, we will discuss an emerging strategy (a pretargeted approach) currently under preclinical evaluation for improving the radiotherapy outcomes by minimizing non-target toxicities.

1.4 Nanomedicine-based drug delivery for cancer

The development of drug delivery systems at the nanometric size range (commonly, 10 – 100 nm) for therapy has shown significant progress over the last few decades (48). These nanometric drug delivery systems offer attractive properties such as the capacity to incorporate multiple agents (e.g., chemotherapeutics, radionuclides, targeting agents, sensing agents), modifying the physiochemical properties and pharmacokinetics of drugs (e.g., improving solubility, increasing the circulation half-life), and enhancing the preferential drug delivery into tumor tissues (48). Examples of drug delivery systems include liposomes, polymeric micelles, inorganic nanoparticles, solid lipid nanoparticles, dendrimers, protein nanoparticles, and polymer-drug conjugates (49, 50). The first nanomedicine approved by the FDA for cancer therapy was a liposomal formulation incorporating doxorubicin (Doxil®) in 1995 (51). To this date, various

nanomedicines have been approved for cancer treatment, with most of them being liposomal-based formulations (52).

1.4.1 Drawbacks of conventional chemotherapeutics

Conventional small chemotherapeutics suffer from several drawbacks such as low solubility, short-plasma half-life, and uncontrolled tissue distribution (48). These drawbacks can lead to poor safety and efficacy profiles. For example, paclitaxel is a commonly prescribed chemotherapeutic drug. It has low water solubility that requires the use of an organic solvent (cremophor), which causes hypersensitivity reactions upon administration (53). Incorporation of paclitaxel into albumin nanoparticles (Abraxane®) improves its solubility and prevents the use of the toxic solvent. Also, the use of Abraxane® allows the clinical dose of paclitaxel to be increased by nearly 50% (175 mg to 260 mg) compared to the smaller molecular weight formulation (Taxol®) (53). However, Abraxane® does not show significant improvements in terms of antitumor efficacy (53). Currently, many clinical and preclinical trials are on-going to evaluate nanomedicines that further exploit the abnormality of tumors (e.g., receptor overexpression, extracellular acidity) in order to improve antitumor efficacy.

1.4.2 Biological barriers to drug delivery systems

The design of an effective drug delivery system is faced with many biological challenges that may slow the clinical translation of these systems. These challenges can be generally categorized into tumor-related and non-tumor related (54). Examples of tumor-related barriers include tumor heterogeneity, hypoxia, and high interstitial fluid pressure. Non-tumor related barriers include easy recognition by immune cells leading to premature sequestration by the mononuclear phagocytic system (MPS).

1.4.2.1 Uptake by the mononuclear phagocytic system (MPS)

The first step of clearance by the MPS is the adsorption of opsonins to the nanoparticles. In general, opsonins are blood plasma proteins that aid in phagocytic recognition (55). The most known opsonins are immunoglobulins and the complement proteins C3, C4, and C5 (55). The second step involves the engulfment of the opsonin-nanoparticle by the phagocytes. Both blood-derived and tissue-resident (e.g., splenic macrophages and Kupffer cells in the liver) macrophages are involved in the rapid removal of nanoparticles (55, 56). Most nanoparticles taken up by the MPS end up retained in the liver and spleen. This process does not only lead to reducing the amount of delivered incorporated drugs (or imaging agents) into the tumor but also causes toxicity to these organs by the formation of lesions, microgranulation of hepatocytes and chronic inflammatory responses (55).

Several strategies have been developed to reduce the MPS uptake, such as modifications made to the physiochemical properties of nanomedicines and MPS blockage by another nanosized formulation (55, 57, 58). Surface modification of nanoparticles with a hydrophilic (neutral or zwitterionic) polymer has shown to reduce the MPS uptake via the reduction of opsonin adsorption (steric hindrance). PEG polymer is the most investigated polymer to date for this purpose. In fact, Doxil® is a PEGylated doxorubicin-liposomal formulation. Early studies using unmodified doxorubicin-loaded liposomes (no PEG polymer) showed lower circulation times and higher MPS uptakes than the PEGylated liposomes (51). Despite its popularity, surface PEGylation has several drawbacks, including reducing tumor cellular internalization of nanoparticles and eliciting an immune response (e.g., production of anti-PEG antibodies after repeated administration) (59, 60).

Additional other strategies for reducing the MPS uptake have already been explored. Examples of these strategies include optimizing the size (larger nanoparticles are more rapidly taken up) and the charge (positive nanoparticles are taken up faster than negative and neutral

nanoparticles) (55, 61). Recent efforts to accelerate the release of already sequestered nanomedicines from the MPS organs will be discussed later in this chapter.

1.4.3 Enhanced permeability and retention (EPR) effect in drug delivery

One of the significant differences between tumor and healthy tissues is the abnormality of tumor vasculature. When a tumor reaches a specific size (1- 2 mm^3), the normal blood vessels become insufficient to supply oxygen and nutrients (62). Therefore, new blood vessels are formed in an irregular manner resulting in abnormal features, including the presence of fenestrations between the endothelial cells. These fenestrations can range from 0.3 to 4.7 μm (depending on the type, environment, and localization of the tumor). These leaky blood vessels allow the transport of nanomedicines into tumor tissues (63). Also, due to the lack of normal lymphatic drainage in the tumor tissues, nanomedicines can reside (inability to diffuse back into circulation) for a longer time in these tissues when compared to than smaller molecules (63).

The enhanced permeability and retention (EPR) effect term was coined to describe the inherent selective targeting of macromolecular agents to tumors due to the presence of vascular fenestrations and the lack of lymphatic drainage described above (64). The delivery of nanomedicines via the EPR effect is also referred to as passive delivery because the transport mechanism does not require energy. The EPR effect was first reported in 1986 by the Maeda group (64), and to date, it is considered by many investigators as the primary mechanism for the delivery of nanomedicines (65-67).

However, the clinical practicality of the EPR effect is still controversial due to the relatively limited clinical success of the nanomedicine field (68). A published report in 2016 showed the median percentage of the injected dose (%ID) of nanomedicines into tumor tissues (regardless of cancer type) in preclinical trials was nearly 0.7%, with no change in this percentage between 2005 and 2015 (69). Furthermore, a recent report showed that tumor blood vessels (ovarian, glioblastoma, and breast) from cancer patients were continuous, with fenestrations rarely being

observed (70). Additionally, the authors of the same study injected gold nanoparticles (15, 50, and 100 nm) in tumor-bearing mice to show that the primary entry mechanism of nanoparticles was transcytosis (active transport requires energy) instead of passive delivery. These results need to be considered in order to improve the drug delivery efficiency of nanomedicines.

1.4.4 Beyond the EPR effect (active targeting and pretargeted therapy as examples)

The modifications of nanomedicine systems with the addition of a targeting agent (e.g., antibody, aptamer, peptide, small molecule) has been widely investigated (71). These targeting agents are mainly selected based on the expression of specific biomarkers within the tumor microenvironment and/or tumor endothelial cells. Numerous nanocarriers with incorporated targeting ligands have demonstrated enhanced tumor accumulation when compared to analogous non-targeted nanocarriers (71). Despite these efforts, the toxicity of the incorporated agents (e.g., radionuclides and chemotherapeutics) to the non-target tissues (e.g., liver and spleen) remains a significant challenge. To address this challenge, a pretargeted approach has been utilized to selectively deliver radio- and chemotherapeutics to tumor cells (72, 73). In our work, we have explored both active targeting using the GRPR and pretargeted constructs. In the next sections, we will summarize the field specifically for the utilization of the GRPR and pretargeted approach for nanomedicine constructs.

1.4.4.1 Targeting GRPR

GRPR is a G protein-coupled receptor expressed in the gastrointestinal tract and central nervous system (74). Stimulation of GRPR causes a variety of biological responses, including contractions of smooth muscles in the gastrointestinal/urogenital tract, stimulation, and secretion of hormones (e.g., insulin), and exhibiting potent CNS effects (e.g., regulation of circadian rhythm) (74). Relative to normal tissues, GRPR is overexpressed in several tumors, including prostate, pancreatic, small-cell lung cancer, and colorectal cancers (38). The elevated expression of GRPR

promotes the proliferation and invasion of tumor cells by activating epidermal growth factor receptor pathways, intermediate early genes c-fos 9, and transcription factors, Elk-1 (75).

Due to this overexpression, the GRPR has been widely investigated as a means to improve cancer imaging and therapy (38, 76). Bombesin (BBN) is a 14-amino-acid amphibian peptide that exhibits a high affinity and specificity towards GRPR. Studies have shown that truncated BBN peptides containing BBN(7-14)NH_2, Gln-Trp-Ala-Val-Gly-His-Leu-Met-NH_2, retain nanomolar binding affinities (38, 77). Currently, several GRPR-targeted constructs are undergoing clinical evaluations (38).

The majority of work regarding GRPR-targeted constructs has focused on developing small molecular BBN-based peptides for radioimaging and radiotherapy (38). Recent studies have investigated the incorporation of GRPR-targeted peptides as targeting ligands to improve the tumor accumulation of nanomedicines, mainly nanoparticles, and showed promising results (38, 78-81). For example, compared to unmodified nanoparticles, ^{64}Cu-sulfide nanoparticles affixed with BBN peptide moieties had nearly three times higher tumor accumulation in an orthotopic prostate cancer model after 1 and 6 hours (h) of administration (82). Interestingly, the uptakes in the liver and spleen were lower for the BBN-modified versus unmodified ^{64}Cu-sulfide nanoparticles. These results indicate the potential of using GRPR-targeted peptides as targeting ligands for improving the performance of nanomedicines.

1.4.4.2 Pretargeted approach: Bioorthogonal reactions via inverse electron-demand Diels–Alder reaction (IEDDA)

The term bioorthogonal reaction describes a chemical reaction between two functional groups that can occur inside the cell/body. There are certain requirements for the bioorthogonal reactions to be utilized in the development of radiopharmaceuticals. These requirements include reaction selectivity between the two functional groups, inertness and non-toxic functional groups, and fast reaction kinetics at submicromolar concentrations (83). Early work in the field of

bioorthogonal chemistry was based on strain-promoted alkyne–azide cycloaddition (SPAAC) (84). This reaction is faster than previously tested click chemistry reactions (e.g., Staudinger ligation), and it does not require a catalyst (Cu-catalyzed azide–alkyne cycloaddition). SPAAC can proceed *in vitro* and *in vivo*. However, its second-order rate constants (K_2) are generally less than 1 $M^{-1} S^{-1}$ (K_2 = 0.0076 – 0.96 $M^{-1} S^{-1}$), which is not suitable for *in vivo* applications at the radiotracer level (73). In contrast, the inverse electron-demand Diels–Alder reaction (IEDDA) is very fast with K_2 values ranging between 100 and 1000,000 $M^{-1} S^{-1}$ (depending on the system type), which makes this reaction ideal for tracer level bioorthogonal chemistry (85).

Joseph Fox's group pioneered the development of constructs for IEDDA, and the first report by the group was published in 2008 (86). Fox's group demonstrated that the reaction between trans-cyclootenes (TCOs) and tetrazines (TZs) is fast (K_2 = 1000 $M^{-1} S^{-1}$) and selective, and can be performed under physiological conditions (87). The only byproduct of the reaction is N_2. The proposed TCO/TZ mechanism is shown in Figure 1.1**.** Interestingly, the *cis*-analog (CCO) of TCO is at least seven-folds lower in reactivity than TCO. Therefore, the CCO isomer must be converted into TCO to obtain a fast reaction with TZ, mainly by a photochemical isomerization. Upon irradiating the CCO moiety, two TCO isomers (major and minor) are produced (Figure 1.2)Error! Reference source not found..

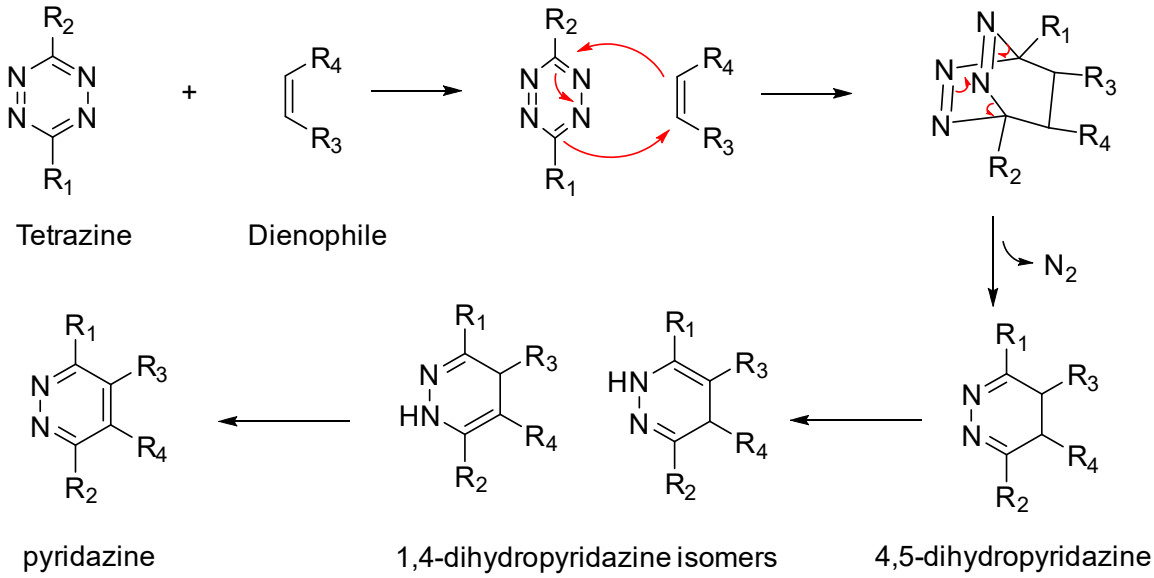

Figure 1.1 The proposed reaction mechanism between the tetrazine (TZ) and dienophile (e.g., TCO).

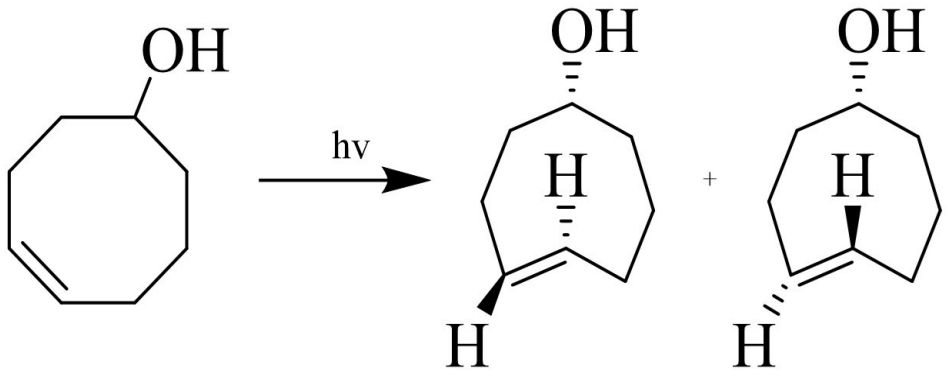

Figure 1.2 Photochemical isomerization of Cis-cyclooct-4-enol to provide the two possible TCO diastereomers.

The attractive properties of IEDDA using TCO/TZ chemistry allows for broad biological and biomedical applications, including *in vivo* drug activation and *in vivo* pretargeted radioimaging and radiotherapy (73). In particular, the latter has gained interest over the last decade because of the drawbacks related to radioimmunotherapy. The long-circulation times of radiolabeled monoclonal antibodies are known to increase radiotoxicities to non-targeted tissues, particularly hematological toxicities (73). To limit these toxicities, a two-step strategy is employed with *in vivo* IEDDA. The initial step involves injecting a non-radiolabeled antibody modified with TCO tags. After a certain time (e.g., 3 days), the antibody is expected to be cleared from blood circulation and accumulated in the tumor tissues at a high tumor to non-target ratio. The second step involves injecting a radiolabeled TZ probe that reacts with the TCO-tagged antibody accumulated in the tumor tissues (Figure 1.3). The TZ probe has a short plasma half-life (several minutes (min)), and therefore unreacted radiolabeled probe will be cleared (mainly via kidneys) from the body rapidly (88). The utilization of TCO-masking agents (e.g., TZ-modified dextran polymer) to further enhance the tumor to normal tissue (T/NT) ratio has been also explored (89, 90). This strategy is based on the injection of compounds that can deactivate the residual TCO in the blood without a significant effect on TCO in the tumor tissues.

The validity of the IEDDA pretargeted approach has been demonstrated in several tumors, such as prostate, pancreatic, colorectal, and ovarian cancers (91). For example, the TCO-modified CC49 monoclonal antibody, which targets the pan-adenoma TAG-72 antigen, was injected into mice implanted with a human colon cancer cell line (LS174T) (92). After three days, ^{111}In-labelled TZ-PEG$_{11}$-DOTA was injected and followed up by performing SPECT/CT imaging at two time points, 1.5 h and 3 days later. After the first time point (1.5 hr), there was already a high tumor radiation signal with low background except for the bladder (due to rapid renal clearance) (Figure 1.4). After the second time point (3 days), the radiation signal was still observed in the tumor with no background signal from the non-target tissues.

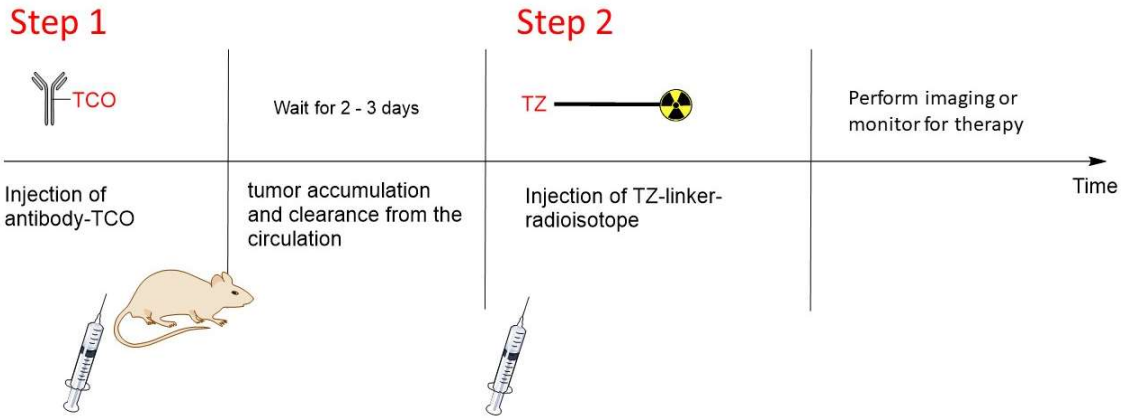

Figure 1.3 Illustration for steps of *in vivo* IEDDA chemistry using antibody.

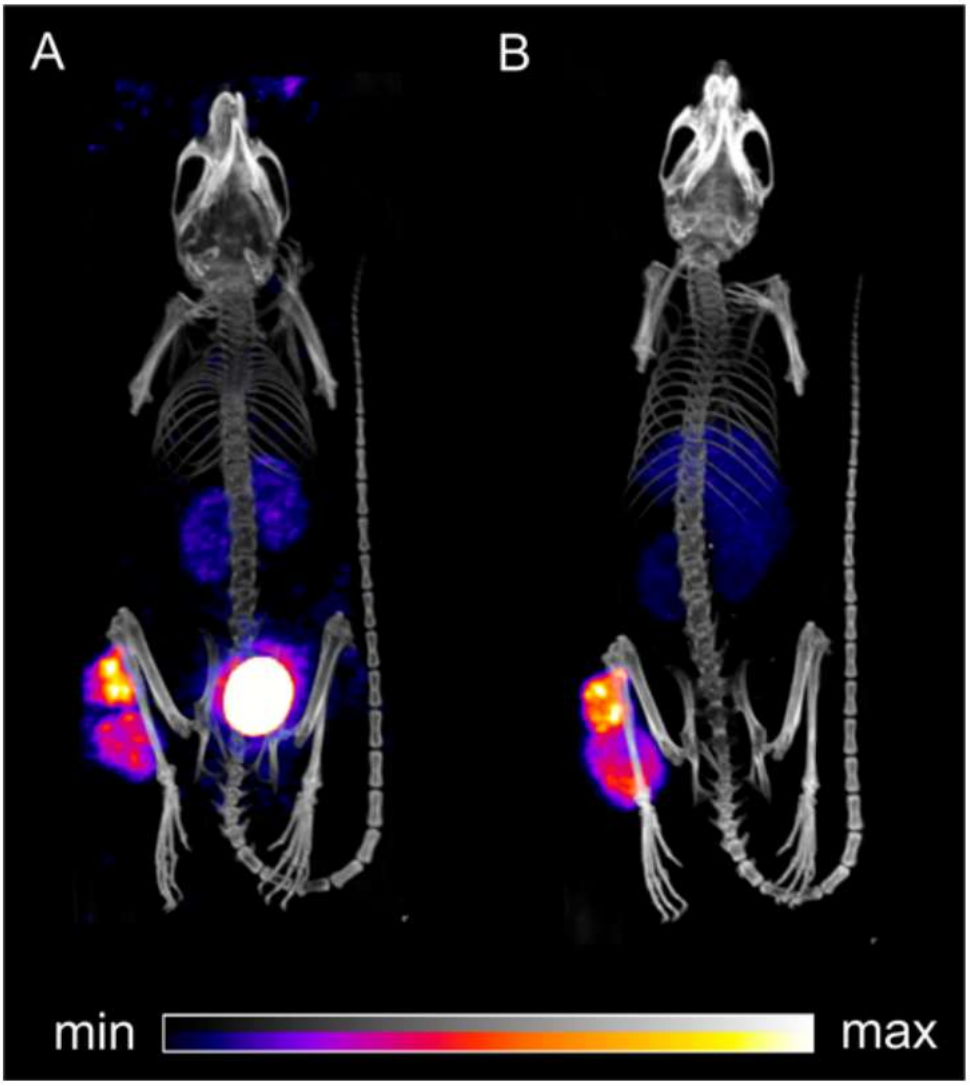

Figure 1.4 Small animal SPECT/CT imaging colon carcinoma animal model preinjected with TCO-modified CC49 monoclonal antibody followed 72 h later by ^{111}In-labeled TZ probe. The imaging was performed 1.5 h (A) and 3 days after injection of the radiolabeled probe. This figure was adapted from *(92)*.

1.4.4.2.1 The rationale for the development of bioorthogonal nanomedicines

Unlike antibodies, drug delivery systems can be multifunctional. They can be designed to carry several agents, including a targeting ligand, imaging agent and therapeutic agent (e.g., small molecular drugs or radioisotopes). Furthermore, unlike antibodies, drug delivery systems can be manipulated (e.g., size, charge, architecture, and functionalities) to achieve the optimal *in vivo* performance. In addition, drug delivery systems can provide a higher loading capacity than antibodies. The average number of TCO units per antibody is generally ≤ 7 units (93, 94). On the contrary, the TCO capacity of drug delivery systems can be several folds higher (depending on the system). There is limited research regarding the use of bioorthogonal IEDDA drug delivery systems, but early data indicates great promise in this field (91). For instance, a recent paper reported the synthesis and biodistribution studies of polymeric crosslinked nanostars (13 nm) modified with an average of 20 TCO units (90). The nanostars were injected into colorectal tumor-bearing mice. After 3 days, the mice were injected with the radiolabeled TZ probe (^{18}F-TZ-PEG$_{11}$-NODA) and the animals were sacrificed 4 h later. The results showed *in vivo* reactivity at the tumor tissues with high tumor to muscle and tumor to spleen ratios (> 1) and good tumor to liver ratio (= 1). However, the tumor to blood ratio was less than 1. These results indicate the feasibility of the *in vivo* IEDDA, but further improvements are needed.

1.4.5 Polymer-drug conjugates as drug delivery systems

Polymer-drug conjugates, a type of drug delivery system, are macromolecular constructs containing bioactives (e.g., small molecules and proteins) bound via covalent bonds. The concept of the polymer-drug conjugate was first proposed in 1955 by Von Horst Jatzkewitz (95). Jatzkewitz reported that by conjugating a small molecular agent (a psychedelic alkaloid called mescaline) to a copolymer of N-vinylpyrrolidone and acrylic acid resulted in increasing the mescaline residence time in mice. However, most current work using polymer-drug conjugates was based on a report by Helmut Ringsdorf in 1975 (96). He proposed using a biocompatible and biodegradable polymer containing three elements: soluble monomeric units or polymeric blocks, a drug bound via a linker, and a targeting agent.

In the 1970s, Jindřich Kopeček pioneered the synthesis of N-(2-Hydroxypropyl) methacrylamide (HPMA) copolymer, which later in 1994 became the first polymer to enter into clinical trials as a polymer conjugating a chemotherapeutic drug (doxorubicin) (97). In 1990, PEG polymer-adenosine deaminase conjugate was the first approved polymer-drug conjugate, classified as a polymer-protein conjugate, used in the treatment of severe combined immunodeficiency caused by an inherited deficiency of the adenosine deaminase enzyme (98). There are various polymer conjugates (mainly based on PEG polymer conjugating proteins) approved by the FDA and currently in the market (Table 1.1). The majority of polymer conjugates under clinical evaluations are based on two polymers, PEG polymers and HPMA copolymers.

Table 1.1 Examples of marketed polymer-drug conjugates *(99)*

Tradename	**Type of polymer carrier**	**Drug**	**Indication**	**Year of approval**
Esperoct	PEG	Factor VIII	Hemophilia A	2019
Palynziq	PEG	Phenylalanine ammonia lyase	Phenylketonuria	2018
Movantik	PEG	Naloxone	Opioid-induced constipation	2014
Krystexxa	PEG	Uricase	Chronic gout	2010
Oncaspar	PEG	L- asparaginase	Acute lymphoblastic leukemia	1994
Smancs	Poly(styrene-co-maleic acid)	Neocarzinostatin	Renal and liver cancer	1993 (Japan)

1.4.6 HPMA copolymer as a polymer-drug conjugate

The HPMA copolymer is a water-soluble polymer that has been demonstrated to be effective in carrying biological and non-biological agents, including proteins, peptides, low molecular weight drugs, imaging agents, and radioisotopes (97, 100). It possesses attractive properties, including non-immunogenicity, biocompatibility, and ease of multifunctionality. An example of a multifunctional HPMA copolymer is shown in Figure 1.5. In this example, an HPMA copolymer incorporates a chelator (used either for radioimaging and/or radiotherapy), a fluorescent imaging agent, a monomer with free amine (used for conjugating carboxylic acid derivatives of agents such as drugs or ligands), and thiol groups on both copolymer ends for post modifications (e.g., maleimide-containing peptides)

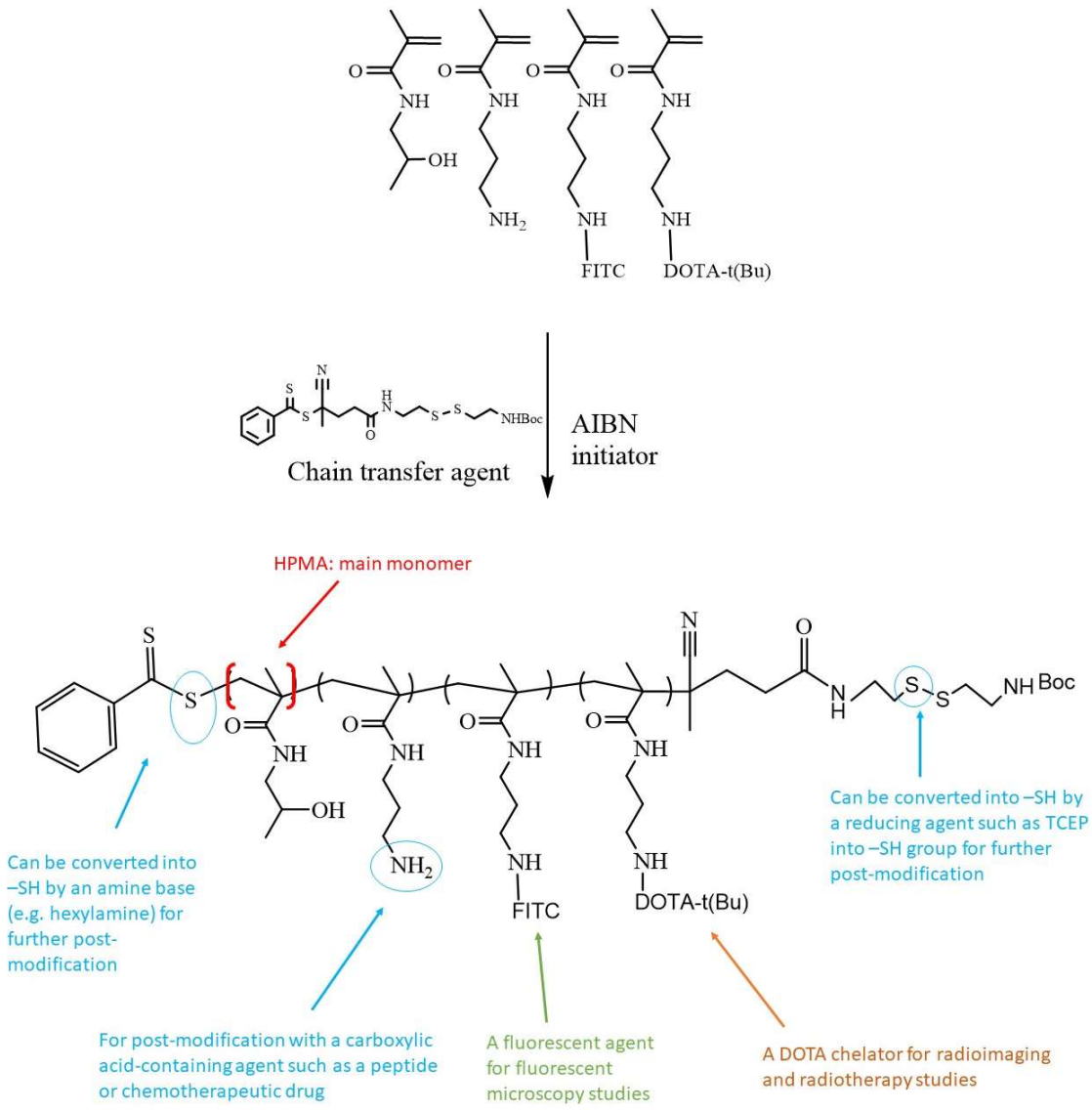

Figure 1.5 Example for the synthesis of a multifunctional HPMA copolymer intermediate for further post-modification.

1.4.6.1 Synthesis of HPMA-drug conjugates

The Kopecek group in the 1960s conducted a series of studies to develop a water-soluble polymeric carrier that can improve the physiochemical properties of drugs (97). These efforts resulted in the development of the HPMA monomer used for the synthesis of HPMA polymers, as first reported in 1973 (97). HPMA-drug conjugates are synthesized via either copolymerization or polymer-analogous reaction routes (97, 101). Copolymerization, which is a polymerization that involves more than one monomer, is a one-step synthetic route. A polymerizable derivative of the therapeutic agent (or targeting ligand/imaging agent) is copolymerized with the HPMA monomer (100). The final concentrations of the agent on the copolymer is controlled by adjusting the comonomer to the HPMA monomer feed ratio. The copolymerization reaction can be performed by employing several polymerization reactions, including reversible addition-fragmentation chain transfer (RAFT), atom transfer radical polymerization (ATRP), or polymerization free radical-mediated polymerization (SFRP) (100).

RAFT polymerization is commonly employed because it offers the advantages of producing polymers with a predetermined controlled molecular weight with narrow dispersity as well as the ease of introducing reactive terminal groups (for post-modification) at the two ends of the HPMA copolymer (102). With this polymerization, a chain transfer agent (CTA) and a polymerization initiator (e.g., 2,2′-Azobis(2-methylpropionitrile) (AIBN)) are dissolved in a solution containing the monomers followed by purging with N_2 and finally heating the mixture (40 – 80 °C) (102). The feed ratio of the monomers, CTA: AIBN, determines the final molecular weight of the copolymer. The type of CTA determines the terminal groups of the copolymer. For example, RAFT polymerization using a CTA agent with a disulfide group results in yielding a copolymer with a terminal thiol (protected) functionality as depicted in Figure 1.5.

After the synthesis, the HPMA copolymer is efficiently purified from the unreacted comonomers and characterized using size exclusion chromatography (SEC). While

copolymerization itself is only one step, it requires prior modifications made to the comonomers (e.g., therapeutic agent) that can become expensive and time-consuming. Also, in some cases, it is challenging to synthesize polymerizable therapeutic agents (e.g., proteins) that are stable under the polymerization conditions (e.g., high temperatures) (103, 104). Alternatively, the polymer-analogous reaction provides an effective way of synthesizing HPMA-drug conjugates (100). This method requires the synthesis of an intermediate HPMA copolymer containing a comonomer with the appropriate chemical handle. For example, a copolymer contains an amine group that can react with a carboxylic acid-containing drug. Another advantage of the polymer-analogous reaction is the synthesis of multiple HPMA-drug conjugates (with variations in the density of conjugated agent) from only one intermediate copolymer simply by reacting with varying concentrations of a drug (103).

1.4.6.2 Physiochemical factors affecting the *in vitro* and *in vivo* performance of HPMA copolymers

Several factors affect the *in vitro* and *in vivo* performance of HPMA copolymers, including the architecture (e.g., linear versus dendrimer), type and number of conjugated hydrophobic agents, and presence of conjugated ligands. However, the size and charge of the copolymer are the most addressed factors.

1.4.6.2.1 Charge: Effect on the *in vitro* and *in vivo* behavior

The HPMA homopolymer, which only consists of the HPMA monomer, is neutral since the HPMA monomer does not have a charged group. The inclusion of charged peptides, proteins, small molecules, and/or charged functional groups (e.g., amines and carboxylic acid) would impact the overall charge of the resulting copolymer. It is known that the overall charge of the polymeric construct can substantially impact cellular uptake. For example, the Kopecek group reported the charge effect on the cellular uptakes of HPMA copolymers (105). The cellular uptakes of five HPMA copolymers, having similar molecular weights (nearly 60 kDa) but varying in charge type

and content (weak negative, strong negative, weak positive, strong positive, and neutral charge) were investigated in a prostate cancer cell line (C4-2 cells). Compared to the neutral copolymer, the weak and strong negative copolymers had nearly 30% and 45% lower cellular uptakes (due to repulsive interactions with the negatively charged cell membranes) after 12 h of incubation. In contrast, the weak and strong positive copolymers had 17- and 28-fold increased cellular uptakes due to the electrostatic interactions with the negatively charged membranes.

The presence of positive charges on HPMA copolymers is also associated with enhancing the *in vitro* cellular uptake when incorporated with receptor-targeted agents. The Huang group reported the cellular uptake of folic acid (a small molecular ligand that binds to folate receptors) incorporated into neutral (contains no N-(3-aminopropyl)methacrylamide (APMA) monomer) and positive (contains ~22% mol. of APMA monomer) HPMA copolymers and examined these agents in a folate receptor-overexpressing cell line (106). The cellular uptake due to folic-acid receptor binding was more than two-fold higher for the positive than neutral copolymers. In competitive binding studies using a folic acid receptor monoclonal antibody (Mov-18) as a competitor, the cellular uptakes of positive and neutral copolymers were reduced by nearly 60 and 15%, respectively. The authors concluded that the receptor-mediated uptake was amplified in the positive copolymer because of the proximity of the positive charge to the cell surface increased the electrostatic interactions with the negatively charged cell membrane (106).

Furthermore, the charge of the polymer plays a significant effect on the *in vivo* behavior of the drug conjugate. A charged copolymer (positive or negative) is generally more efficiently cleared from circulation than its uncharged counterpart (107). In a study of three HPMA copolymers having similar molecular weights (nearly 30 kDa) but varying in charge, the blood circulation times were investigated after i.v. injection of the conjugates in tumor-bearing rats. Compared to the neutral copolymer, the positive and negative copolymers had lower blood level values by 50% and 15%, respectively, over the monitoring period (168 h) (107). Similarly, the

content of folic acid (negatively charged ligand) on the HPMA copolymer was associated with lower blood concentrations. The higher the folic acid content, the faster the copolymer is cleared from the circulation (107).

The retention of charged copolymers in the liver and spleen due to the MPS uptake has been demonstrated to be size and chemical group dependent (108-111). For instance, carboxylic acid- and hydrazide-modified copolymers generally have lower retention in MPS-associated tissues than neutral copolymers (due mainly to the efficient body clearance) (108, 109). In contrast, the quaternary amine-modified copolymers are taken up by the MPS more efficiently. A study reported that nearly 70% of the i.v. injected dose (in rats) of the HPMA copolymer (62 kDa) containing 16.3% mol. of a quaternary comonomer (trimethylammonioethyl methacrylate) accumulated in the liver after only 30 mins (110). Another study from the same group using the same copolymer and animal model reported more than 50% of the dose found in the liver after 5 min compared to only 4% for a neutral copolymer with a similar molecular weight (111).

1.4.6.2.2 Size: Effect on the *in vitro* and *in vivo* behavior

An inverse relationship between the cellular uptake and the molecular weights of HPMA copolymers is observed (105). A report explored the cellular uptakes of ten narrowly polydisperse HPMA copolymers with molecular sizes of the smallest and largest copolymers between 10 and 200 kDa, respectively. The separation of these ten fractions was performed using SEC, which elutes the larger copolymer first followed by smaller copolymers. The fractions containing the small copolymeric sizes (e.g., fraction 8) had higher uptakes than the fractions containing the larger copolymeric sizes (e.g., fraction 4). However, the charge effect generally has more impact on the cellular uptake than the molecular size.

It is generally accepted that the renal clearance threshold for the non-biodegradable polymers is < 50 kDa (97). A polymeric construct with a higher molecular weight has longer circulation times and a lower renal clearance rate relative to a polymeric construct with less than

50 kDa molecular weight. The longer circulation time of a large copolymer leads to higher liver and spleen retentions (100). Since the HPMA copolymer is non-biodegradable, choosing a lower molecular weight to overcome the renal threshold limit is crucial. However, larger HPMA constructs circulate for longer times leading to enhanced tumor accumulation (100). A study reported the effect of molecular size of the polymer on the biodistribution in tumor-bearing rats by testing three HPMA copolymers of various sizes (23, 31, and 65 kDa) (109). After 168 h, there was observed a direct relationship between the molecular size and the concentration of the copolymers in the blood (and most of the organs including liver, spleen, lungs, heart, and kidneys). The tumor accumulation for the largest copolymer (65 kDa) was nearly three and six folds higher than the 31 and 23 kDa-sized copolymers, respectively. Therefore, HPMA copolymers with higher molecular weights than the renal threshold limit can improve the efficacy of the conjugated drug (by enhancing the tumor accumulation) but an increase in side effects (due to the retention in off-target tissues) is a consequence.

1.4.6.3 Overcoming the non-biodegradability and MPS retention of HPMA copolymers by the incorporation of a cathepsin S (Cat S) cleavable linker (CL)

Cysteine cathepsins are lysosomal proteases with diverse functions, but are mainly involved in protein degradation in the endolysosomes (112). The tissue distribution of these enzymes varies depending on the type of cysteine cathepsins. These enzymes can be found ubiquitously in most tissues (e.g., cathepsin B) or within specific tissues (e.g., cathepsin S (Cat S)). For example, cathepsin B is expressed at a higher level in the tissues of the liver, spleen, kidneys, and thyroid. On the other hand, Cat S is mainly expressed abundantly in immune cells such as macrophages and antigen-presenting cells (e.g., B cells and dendritic cells) (112).

Aside from their physiological roles, many of these cysteine cathepsins play roles in cancer development (112). For instance, Cat S is associated with driving angiogenesis in a hypoxic environment and promoting a pro-inflammatory tumor microenvironment by transcriptionally

regulating cytokine CCL2 via cleavage of CD74 (113). The expression of cysteine cathepsins is heterogenous across cancer types (112, 114, 115). For instance, cathepsin B is upregulated in breast, prostate, and ovarian cancers but downregulated in kidney cancer. Cat S is upregulated in prostate and lung cancers but downregulated in kidney cancer (112).

Efforts have been made to design large HPMA copolymers (> renal threshold limit) that have extended circulation times before being metabolized into smaller fragments (by the cathepsins) leading to their excretion by the kidneys (116-118). The Kopeček group published several papers regarding the use of long-circulating HPMA copolymers cleaved by lysosomal proteases (mainly, cathepsin B). For example, an extension for a doxorubicin-HPMA copolymer (20 kDa) with the peptidic linker (glycine, phenylalanine, leucine, and glycine (GFLG)) was reported (118). The resulting multi-block HPMA copolymer was fractionated into a series of segments using size exclusion chromatography to afford copolymers of 93, 184, and 348 kDa. These copolymers had higher antitumor efficacy when compared to the smaller studied copolymer (20 kDa) in tumor-bearing mice. A follow-up report from the same group investigated the biodistribution data of a smaller copolymer (48 kDa) and a multi-block copolymer (335 kDa) and illustrated the same conclusion (119). However, the multi-block copolymer had more than two-folds higher liver and spleen retention compared to the smaller copolymer.

Inspired by this work, Dr. Garrison's lab has started working on improving the imaging of pancreatic cancer by developing a multi-block HPMA copolymer containing a Cat S enzyme biodegradable linker (117, 120). Initially, the peptide sequence of PMGLP, a known Cat S substrate, was synthesized with two incorporated maleimide groups at each terminus to afford a Cat S susceptible linker (CL). A bis-thiol terminated HPMA telechelic copolymer (18 kDa) containing 1,4,7,10-tetraazacyclododecane-1,4,7,10-tetraacetic acid (DOTA), as a chelator, was synthesized. Finally, a thiol-ene click reaction was performed between the linker and the copolymer to obtain the multi-block HPMA copolymer (80 kDa). Compared to two copolymers having the

same molecular size but lacking CL, the Cat S cleavable multi-HPMA copolymer was observed to have lower retention values in the blood, liver, and spleen. After 72 h, the retention in these organs was already about 50% lower compared to the non-cleavable copolymers. Interestingly, tumor accumulation did not vary among the tested copolymers. These results indicate the benefits of incorporating a linker that is susceptible to Cat S in enhancing the safety and efficacy of large HPMA copolymers.

1.4.6.4 HPMA copolymers in clinical trials

To date, there is no approved drug based on HPMA copolymers. However, several conjugates are under clinical evaluations (Table 1.2). The first HPMA copolymer that was tested clinically was PK1 (doxorubicin-bound HPMA copolymer) reported in 1999 (97). PK1 had a molecular weight (30 kDa) of less than the renal threshold to allow for renal clearance. In preclinical trials, PK1 extended the circulation time of doxorubicin with better safety and efficacy profiles than free doxorubicin (97). In clinical trials (in patients with different types of cancer), PK1 showed extended blood circulation with improved overall safety profiles. Nevertheless, its antitumor efficacy was observed in only a subset of the population; 6 out of 56 patients had a partial response. These results led to the discontinuation of its further clinical testing (100).

PK2 is the second drug-HPMA conjugate to enter the clinical trials (121). It is also doxorubicin-based and has a molecular weight similar to PK1. However, PK2 is modified with a targeting ligand (galactosamine) that binds to the asialoglycoprotein receptor expressed mainly on hepatocytes. In liver cancer patients, the first phase clinical trial of PK2 showed nearly 17% of the injected dose accumulated in the liver, and 3.3% accumulated in the tumor after 24 h of administration. Interestingly, PK1 was used as a control and showed no liver targeting. The maximum tolerated toxicity doses for PK1 and PK2 were 320 and 160 mg/m^2, respectively and based on that, a dose of 120 mg/m^2 was recommended for PK2 in the phase 2 clinical trial. The

other clinical trials based on HPMA copolymer are in phase 1 and phase 2 stages, with no formulations having progressed to phase 3 studies to date (Table 1.2).

Table 1.2 HPMA-drug conjugates in clinical trials

Name	Drug	Cancer type	Clinical trial	Main results	Reference
PK1	Doxorubicin	Solid tumors	Phase 2	Improved safety profiles but minimal response is observed	(122)
PK2	Doxorubicin	Liver	Phase 1	Active targeting to the liver and tumor, compared to PK1. MTD is 160 mg/m2 (half of PK1).	(121)
PNU166945	Paclitaxel	Solid tumors	Phase 1	Water-soluble and therefore no organic solvent is needed Prolonged the plasma concentration of the drug	(123)
AP5280	Platinum	Solid tumors	Phase 1	MTD was found to be 4500 mg/m2 3300 mg/m2 was recommended for the phase 2 trial.	(124)
AP5346	Platinum	Solid tumors	Phase 1/2	Tolerable side effects	(125)
P-THP	Pirarubicin	Prostate (stage IV)	One case	No serious toxicities No relapse within 20 months of monitoring	(126)

1.5 Decorporation in the case of the release of radiological materials

Radionuclides are commonly used for industrial, commercial, and military (nuclear reactors and the production of nuclear weapons) purposes (127). Their uncontrolled release into the environment (due to accidents, natural causes, or terrorist attacks) remains a significant public health concern (127). For example, on March 11 of 2011, a catastrophic earthquake (with a magnitude of 9.0) and tsunami occurred in Japan that damaged the Fukushima Daiichi nuclear power plant (NPP). Due to the failure of the cooling systems of the nuclear reactor, explosions occurred that led to a release of radioactive materials (~ 900 PBq) into the atmosphere and subsequent deposition on the ground. This incident led to the immediate evacuation of people living within a 20 km radius surrounding NPP (128). Numerous studies over the following years were conducted to evaluate the potential health impact (e.g., water or crop contamination) of these released radioactive substances (129-132).

The radioisotopes of actinides (e.g., plutonium (Pu) and americium (Am)) are among the most highly used radionuclides (133). For example, ^{239}Pu is the main isotope for the production of nuclear weapons. It is produced from uranium-238 (^{238}U). It undergoes alpha decay with a half-life of 24,000 years. Another example is ^{238}Pu, mainly used as a heat source in radioisotope thermoelectric generators (e.g., applications in spacecraft). It also undergoes alpha decay with a half-life of 87.7 years. One last example is ^{241}Am, which is produced from ^{241}Pu. It undergoes alpha decay with a half-life of 430 years. It is used in the manufacturing of smoke detectors and the production of heavier americium isotopes.

Depending on the type of actinide, the internal biological contamination of radioactive substances can occur either via oral (ingestion), inhalation, or skin (open wound) routes (134). This internal contamination can lead to serious health effects, including genetic changes, impairment of organ function, carcinogenesis, fibrosis, and vascular pathology (135, 136). The radionuclides that emit alpha particles cause more damaging effects than beta and gamma emitters. Unfortunately, upon contamination, actinides deposit in various organs (e.g., kidneys, liver, and bone), leading to further local effects at the deposited organ (134). The pharmacokinetics and biodistribution profiles for actinides are different based on the radionuclide type. For example, the biodistribution profiles of the i.v. injected ^{239}Pu and ^{241}Am in rats showed high retentions in the liver and skeletons but at different percentages (135). The percentage of the injected dose of ^{239}Pu in the liver and skeletons was 11% and 60% after seven days. In contrast, the percentage of injected dose for ^{241}Am in the liver and skeletons were 40% and 31%, respectively. Nevertheless, only 29% of the injected doses for both radionuclides were either excreted or retained in other tissues.

Unfortunately, many actinides can be retained in the liver and skeleton for long term. ^{241}Am has been shown to have a slow excretion in nonhuman primates (baboon) with only 50% excreted after two years of administration. The estimated percentage of the injected dose in the skeletons and liver were 37% and 22.2%, respectively, three months post ^{241}Am injection (137).

1.5.1 Treatment of contaminated individuals

Currently, the chelator diethylentriamene pentaacetate (DTPA) is the only FDA approved agent (Ca-DTPA or Zn-DTPA formulations) for the treatment of contaminated individuals by the actinides: Pu, Am, or curium (Cm). Due to its low bioavailability (< 3%), it is given as either an injectable or inhalable (138). DTPA has a short plasma half-life (< 2 h), with the kidneys being the main route for clearance (139, 140). DTPA is a chelator, that has high affinity to complex actinides in physiological fluids. Unlike the free actinides, the DTPA-actinide complex does not remain retained in the bones and liver. This actinide complexation by DTPA leads to increasing the

clearance of internalized radioactive actinides. The dose of DTPA usually administrated is 1 g/day, but due to its short half-life (< 2 h) more than one daily dose may be needed (139). The most common side effect of DTPA is the loss of essential minerals (e.g., Ca, Zn, and Mg) which can lead to severe health issues (e.g., nephrotoxicity and instant cardiac arrest) (141).

The timing of DTPA treatment is crucial. The efficiency of DTPA to remove the internalized actinides from the body is inversely related to the time after contamination. DTPA is considered inefficient to remove the actinides already deposited in organs (e.g., liver and skeletons) due to poor DTPA distribution to such organs (134). A study reported that a delay in the initiation of the DTPA treatment from 1 h to 5 h post-contamination with ^{238}Pu resulted in a nearly 2.5 folds increase in the radioactivity retained in mice after one day (142). Therefore, DTPA can be administered at repeated daily or weekly doses for months, depending on the case. Despite the repeated administration, removal of only 50% of the already deposited actinides is considered a good result (143). Therefore, it is essential for the DTPA to be administered as soon as the internal contamination is confirmed to limit the organ deposition of the radionuclides.

1.5.2 The need for a prophylactic formulation

The current chelation therapy for actinide contamination is only based on post-exposure treatment using DTPA. A prophylactic formulation is an ideal solution to eliminate the lag time between internal contamination and DTPA administration. Such a formulation can be administered for high-risk individuals such as personnel who respond to emergency incidents where radionuclides have been or may be potentially released. Due to its short half-life, DTPA is not an appropriate drug to be administered for prophylaxis. To date, there is limited research concerning the development of such formulations. For example, a longer circulating DTPA formulation based on liposomal encapsulation of DTPA was investigated as prophylactic therapy in rats (144). The DTPA-liposomal formulation was injected as a 5 μmol/kg dose (based on DTPA content) three days before injection of ^{238}Pu. After seven days, the ^{238}Pu retention in the liver and bones was

reduced by 47% and 29%, respectively, compared to no treatment. Other studies were focused on developing strategies using small-molecular or nanoparticle-based formulations to improve the clearance of the already deposited actinides for treatment purposes (142, 145, 146).

2 Chapter 2. *In Vitro* Evaluation and Biodistribution Studies of HPMA Copolymers Targeting the Gastrin Releasing Peptide Receptor in Prostate Cancer

2.1 Introduction

Prostate cancer is currently the most prevalently diagnosed and second-deadliest form of cancer for men in the U.S. (1). The gastrin-releasing peptide receptor (GRPR) has been shown to be expressed on a large fraction of human prostate cancers (147). This has given the impetus for the development of GRPR-targeted diagnostic agents with the purpose of detecting, staging and/or monitoring therapeutic treatment efficacy as well as differentiating indolent from aggressive forms of prostate cancer (148). Bombesin (BBN) is a fourteen amino acid peptide that exhibits nanomolar binding affinity to the GRPR. Studies have shown that only the C-terminal fragment BBN(7-14)NH_2 (Gln-Trp-Ala-Val-Gly-His-Leu-Met-NH_2) is needed to retain nanomolar binding affinity (77). A number of truncated (e.g., BBN(7-14)) and modified BBN based agents have been developed (148-151) and several have entered clinical trials (e.g., NCT02624518 and NCT03872778) for imaging prostate and other GRPR-positive cancers (152-154).

Over the last few decades, the development of cancer diagnostic and therapeutic agents based on nanomedicine platforms have been explored by numerous laboratories (155-157). These constructs offer many attractive attributes for this purpose, including their drug loading capacity and ability to be multi-functional (e.g., theranostic). Nanomedicine platforms are able to selectively target cancers based on two distinct mechanisms: passive and active targeting. The passive targeting capability of nanomedicine constructs is due to the enhanced permeability and retention (EPR) effect which principally involves vasculature and lymphatic irregularities in cancerous tissue relative to normal tissue (158). Active targeting involves the modification of the nanomedicine construct with targeting vectors that are capable of recognizing molecular markers on the surface

of tumor cells or within the tumor microenvironment. Through this mechanism, actively targeted nanomedicine constructs are conceivably able to enhance the delivery of the construct to tumors.

To date, numerous targeting vectors have been explored including those based on small molecules, peptides and antibody (159). Indeed, several investigators have explored the utilization BBN peptides to enhance the delivery of nanomedicine constructs (e.g, gold, glycol chitosan, and copper sulfide nanoparticles) to GRPR-positive cancers (81, 82, 160, 161). The efficiency of active targeting has been found to be associated with molecular size (162, 163). Nanomedicine constructs with lower molecular sizes (< 50 nm) generally exhibit a higher level of tumor delivery enhancement due to active targeting (163).

N-(2-hydroxypropyl)methacrylamide (HPMA) copolymers have emerged as a promising nanomedicine platform due to their nontoxic and nonimmunogenic nature (97, 164). Our laboratory and others have explored HPMA copolymer constructs as nuclear medicine diagnostics (117, 120, 165-167). Furthermore, several laboratories have demonstrated that *in vivo* targeting using HPMA copolymers (i.e., < 50 nm) can be enhanced through the inclusion of targeting ligands (e.g., integrin targeting using cRGD) (165). In this work, we explore the development of HPMA copolymers incorporated with BBN(7-14)NH_2 peptides to examine if GRPR-targeting can enhance accumulation in GRPR-positive prostate cancer. Specifically, we examine what impact BBN incorporation density and peptide charge has on the biological performance of these constructs in an *in vitro* human PC-3 prostate cancer model and in an *in vivo* mouse model. By better understanding these parameters, we aim to develop improved diagnostic and therapeutic GRPR-targeted nanomedicine constructs for prostate and other GRPR-positive cancers.

2.2 Materials and methods

2.2.1 Chemicals

If not otherwise indicated, all solvents used for polymer reactions and silica gel purification were ACS grade and obtained from Fisher Scientific. Water was deionized using a Milli-Q® Integral Water Purification System (Millipore Corp., U.S.). Acetonitrile (ACN) and formic acid were HPLC grade and purchased from Fisher Scientific (U.S). Dichloromethane (DCM), N,N-dimethylformamide (DMF), trifluoroacetic acid (TFA) were peptide synthesis grade and purchased from Fisher Scientific (U.S). Fluorescein isothiocyanate (FITC), 1-Ethyl-3-(3-dimethylaminopropyl)carbodiimide (EDC), N-hydroxysuccinimide (NHS), triisopropylsilane (TIS), 4-cyano-4-(phenylcarbono-thioylthio)pentanoic acid (CTA), and 2,2′-Azobis(2-methylpropionitrile) (AIBN), Tris(2-carboxyethyl)phosphine (TCEP), ethylenediaminetetraacetic acid (EDTA), and methacrylic acid were purchased from Sigma-Aldrich (U.S). N-(2-Hydroxypropyl)methacrylamide (HPMA) and N-(3-Aminopropyl)methacrylamide (APMA) were obtained from Polysciences (U.S.). Unless indicated, Fmoc-protected amino acids were purchased from NovaBiochem. Boc-cystamine hydrochloride, Fmoc-D-His(Trt)-OH, Fmoc-D-Trp(Boc)-OH, Fmoc-D-Ala-OH, Fmoc-D-Leu-OH, and Fmoc-D-Val-OH were obtained from Chem-Impex Int'l Inc. (U.S.). Fmoc-D-Met and 6-Maleimidohexanoic acid were obtained from Alfa Aesar (U.S.). Fmoc-D-Gln was purchased from AstaTech (U.S.). Fmoc-D-Phe(4-F)-OH and N,N-Diisopropylethylamine (DIEA) were obtained from ChemPep (U.S.). Rink amide and 3-([ethyl-fmoc-amino]-methyl)-indol-1-yl]-acetyl am resins, Fmoc-NH-$(PEG)_2$-COOH, and O-(Benzotriazol-1-yl)-N,N,N',N'-tetramethyluronium tetrafluoroborate (HBTU) were purchased from NovaBiochem. L-Cysteine hydrochloride and sodium tetrafluoroborate ($NaBF_4$) were purchased from Acros (U.S.). Piperidine and phenol were purchased from Sigma-Aldrich (U.S). Phosphate buffered saline (PBS), and 1-piperazineethanesulfonic acid (HEPES) were purchased from Fisher Scientific (U.S.). Ham's F-12K Medium and fetal bovine serum (FBS) were obtained

from Gibco (U.S.). 5,5-dithio-bis-(2-nitrobenzoic acid) (Ellman's reagent), L-glutamine, Hoechst 33342, and LysoTracker® Red DND-99, sodium dodecyl sulfate (SDS) were purchased from Thermo Fisher Scientific (U.S.). CF-1 female mice were purchased from Charles River Laboratories. All procedures on animals were consistent with the Guide for the Care and Use of Laboratory Animals by the National Institutes of Health and were approved by the Institutional Animal Care and Use Committee (IACUC) at the University of Nebraska Medical Center.

2.2.2 Instrumentation

A Liberty microwave peptide synthesizer (CEM, U.S.) was used to synthesize peptides via solid phase peptide synthesis (SPPS). Equipped with a Waters 2489 absorption detector and a Waters Qtof Micro electrospray ionization mass spectrometer, a Waters (U.S.) e2695 system was used to perform reversed phase-high performance liquid chromatography/mass spectrometry (RP-HPLC/MS) analyses. A Bruker Avance-III HD 500 MHz instrument (U.S.) was used to record ^{1}H-NMR and ^{19}F-NMR spectra using either deuterated dimethyl sulfoxide or deuterium oxide as a solvent. A Phenomenex (U.S.) Jupiter C12 Proteo 250 x 10.0 mm semiprep column was used to purify peptides. Weight and size measurements of HPMA copolymers were performed using a Viscotek TDA max system (Malvern Instruments Inc., U.S.) equipped with Shodex Asahipak GF-510 HQ GPC column. Biochrom WPA Biowave II UV/Visible Spectrophotometer was obtained from Biochrom (U.S.). An LSM 710 confocal microscope (Carl Zeiss Microimaging, Inc., U.S.) was used to visualize stained cells. Multi-Wiper nuclear medicine gamma counter (LTI, U.S.) was used for counting the activity bound to cells. Gamma decay detection of injected radiolabeled conjugates was performed using NaI (Tl) well detector constructed by AlphaSpectra Inc. (U.S.).

2.2.3 Synthesis and characterization of BBN peptides and BBN-HPMA conjugates

2.2.3.1 Synthesis of BBN peptides

The synthesis of the BBN peptides (BBN-RR, D-BBN-RR, BBN-EE, and BBN-DOTA) was performed using an automated solid-phase peptide synthesizer on a Rink Amide resin. Briefly, the resin (100 μmol of the resin substituted peptide anchors) was first deprotected using 20% piperidine in DMF, resulting in the formation of the primary amine. Fmoc protected amino acids (0.5 mmol) were activated using HBTU and added to the growing peptide of the resin. The synthesized peptide was cleaved from the resin using a cleavage cocktail containing TFA/phenol/water/TIS (88/5/5/2). The cleaved peptide was precipitated in cold methyl-tert-butyl ether and filtered. The crude product was dried, and the desired peptide was purified using LC/MS. BBN-Anta was synthesized under similar conditions, except that 3-([ethyl-fmoc-amino]-methyl)-indol-1-yl]-acetyl am resin was used. Before any *in vitro* and *in vivo* studies, all peptides were purified to give ≥ 95% purity based on LC/MS.

2.2.3.2 Synthesis of monomers

FITC-APMA was synthesized according to a literature reports (168). A synthesized DOTA-tris(*t*Bu)-NHS (169) was reacted with APMA to synthesized DOTA-tris(*t*Bu)-APMA according to a literature report (170). To synthesize the *N*-*tert*-butoxycarbonyl-*N*′-methacryloyl-cystamine (Boc-Cyst-MA) monomer, methacrylic acid (46.5 mg, 0.54 mmol), EDC (115 mg, 0.6 mmol) and NHS (79.4 mg, 0.69 mmol) were dissolved in 500 μL of DCM and allowed to stir for 2 h. Boc-cystamine (0.45 mmol) was added followed by the addition of DIEA (0.9 mmol). After 16 h, the reaction mixture was washed with DI water three times, dried over $MgSO_4$, and concentrated under vacuum. The product was purified by silica gel chromatography using petroleum ether:acetone (10:1) as the eluent solvent system to yield the pure product (99.2 mg, 0.31 mmol, 71%). The product was characterized by ES-MS ($[M+H]^+ = 321.1$) and ^{1}H-NMR.

2.2.3.3 Synthesis of HPMA copolymers

With modifications made from a previously described method (117), reversible addition-fragmentation chain transfer (RAFT) polymerization was employed to synthesize two batches of HPMA-SS copolymers. Briefly, HPMA, Boc-Cyst-MA, APMA-FITC, and DOTA-tris(*t*Bu)-APMA monomers were dissolved in a dioxane/DI water (2:1) solution at a molar ratio of 84:15:0.5:0.5, respectively (with the total monomer amount summing to 0.5 mmol). AIBN initiator (0.33 mg, 2.01 μmol) and CTA (0.49 mg, 1.75 μmol) were added to make the final volume of 0.5 mL. The resultant mixture was transferred to a glass ampule and purged with nitrogen for 40 min. The ampule was subsequently flame sealed and the polymerization allowed to proceed at 50 °C for 48 h. The reaction mixture was cooled to room temperature and loaded onto an LH-20 column using methanol as an eluent to yield the HPMA polymer (71 mg, 82% yield). The molecular weight analysis was performed using gel permeation chromatography (GPC) with an elution mixture of ACN/PBS (40:60). To determine FITC content, a standard curve was prepared of known FITC-APMA monomer concentrations (0.92 to 14.65 μM, PBS) using a UV/Vis spectrophotometer (absorbance wavelength = 494 nm). Then, 667 μg of the HPMA copolymer was dissolved in 1 mL PBS, and the absorbance at 494 nm was recorded (n = 2). The FITC concentration was extrapolated from the prepared standard curve. The content of DOTA was determined by signal integration from ^{1}H-NMR spectroscopy.

2.2.3.4 Synthesis of BBN-HPMA conjugates

The BBN-HPMA conjugates were synthesized by coupling the HPMA-SH copolymer with BBN-RR (or D-BBN-RR), BBN-EE, or both BBN-RR and BBN-EE to give positive, negative, or zwitterionic conjugates, respectively. HPMA-SH-1 (batch 1) was used to synthesize the positive and zwitterionic BBN-HPMA conjugates, while HPMA-SH-2 (batch 2) was used for the synthesis of the negative BBN-HPMA conjugates.

The synthesis of BBN-HPMA conjugates was performed in two steps. First, the HPMA copolymer (10 mg) from either batch 1 or 2 was dissolved in DI water (500 μL), and TCEP (100 times more than the equivalent theoretical content of the Boc-Cyst-MA monomer) was added to the solution to generate the free thiol groups on the polymer side chains. After 4 h, the mixture was loaded on an LH-20 column using methanol as the eluent. The collected fractions were evaporated to give the HPMA-SH copolymers. To estimate cystamine incorporation, Ellman's reagent was utilized to estimate the thiol content of the HPMA-SH (batch 1 and 2) (171). Briefly, 2.5 mL of the reaction buffer (0.1 M sodium phosphate buffer (pH = 8.0) containing 1 mM EDTA) was mixed with 50 μL of a solution of Ellman's reagent (4 mg/1 mL reaction buffer). Then, 100 μg of either the HPMA-SH-1 or -2 copolymer (dissolved in 250 μL of the reaction buffer) was mixed with the previous solution and incubated at room temperature for 15 min. The absorbance (λ = 412 nm) was measured for the mixture using a UV/Vis spectrophotometer. The concentration of the free thiol groups was extrapolated from a standard curve prepared from the absorbance of known concentrations (0.1 – 1.0 mM) of L-cysteine hydrochloride reacted with Ellman's reagent under the same conditions.

Next, conjugation of the BBN peptides to the HPMA-SH copolymers was performed through thiol-ene "click" chemistry. The amount and type of BBN peptide used for the synthesis of each BBN-HPMA conjugate are displayed in Table 2.1. The desired amount of a BBN peptide was dissolved in DI water and added to a solution of HPMA-SH (5 mg) to make the final volume of mixture 500 μL. The reaction mixture was purged with N_2 for 40 min and stirred at room temperature for 16 h. The non-conjugated BBN peptide was removed by LH-20 column using methanol as an eluent. The fractions of the BBN-HPMA conjugates were collected and evaporated to dryness. P-RREE-1 and P-RREE-2 were synthesized similarly by adding the desired BBN-EE amount to a solution containing 7.30 mg of the already characterized P-RR-2. The amount of peptide content per BBN-HPMA conjugate was determined by ^{19}F-NMR spectroscopy using

$NaBF_4$ as an internal reference (average peptide conjugation yield for the synthesized BBN-HPMA conjugates: 76.6 ± 14.8%, n = 11). Before any radiolabeling experiments, the BBN-HPMA conjugates were exposed to a TFA cleavage cocktail (TFA/phenol/water/TIS (88/5/5/2)) to deprotect the DOTA-tris(*t*Bu). After 1 h, the TFA was evaporated under N_2 flow, and then the conjugates were solubilized in methanol and purified using an LH-20 column.

Table 2.1 Feed BBN peptide amount for BBN-HPMA conjugation reaction

BBN-HPMA conjugate[†] Group	Name	Type of BBN peptide[*] BBN-RR (μmol) ++	D-BBN-RR (μmol) ++	BBN-EE (μmol) −−
Positive	P-RR-1	0.17		
	P-RR-2	0.57		
	P-RR-3	1.14		
	P-RR-4	2.29		
	P-D-RR-3		1.14	
Negative	P-EE-1			0.17
	P-EE-2			0.57
	P-EE-3			1.14
	P-EE-4			2.29
Zwitterionic	P-RREE-1	0.57		0.17
	P-RREE-2	0.57		0.57

[†]The numbers 1 through 4 indicate the increasing peptide content with 1 and 4 being the lowest and highest peptide content in each group of BBN-HPMA conjugates.

[*]Values in the table are normalized based on the calculations for 1 mg of HPMA-SH.

++ and −− represent the number and type of charges added to the active moiety BBN(7-14)NH_2 .

2.2.4 Radiolabeling of the BBN-HPMA copolymer conjugates and BBN-DOTA peptides

Radiolabeling of BBN-HPMA copolymer conjugates was performed by dissolving 200 µg of the conjugates in 100 µL DI water, followed by the addition of 3.7 MBq of $^{177}LuCl_3$. The resultant solution was heated at 90 °C for 60 min. After cooling, the radiolabeled BBN-HPMA conjugates were purified using an Agilent PL aquagel-OH MIXED-H GPC column with an ACN/PBS (40:60) elution. A radio-HPLC equipped with a Bioscan flow count radiometric detector and Waters 2489 UV detector (λ = 494 nm) was used to identify the radiolabeled BBN-HPMA conjugates. After collection, the radiolabeled conjugates were buffer exchanged to PBS and concentrated using an Amicon Ultra-4 centrifugal filter (10 kDa) before continuing on to any *in vitro* or *in vivo* studies.

BBN-DOTA was radiolabeled by dissolving 25 µg of the peptide in an ammonium acetate buffer (0.5 M, 100 µL, pH = 5.5) followed by the addition of 3.7 MBq (100 µCi) of $^{177}LuCl_3$. The solution was heated to 90 °C for 60 min. To enhance the ease of purification of the radiolabeled BBN-DOTA from the unlabeled peptide, 4-6 mg of $CoCl_2$ was added, and the solution was heated for an additional 5 min at 90 °C. The radiolabeled BBN-DOTA was purified using radio-HPLC employing an analytical Proteo C12 column with a 1.5 ml/min flow rate and a gradient from 89% to 83% of ACN in DI water (containing 0.1% formic acid) over 15 min. The radiolabeled BBN-DOTA was concentrated using solid phase extraction employing a C18 extraction disk (3M Empore) with an ethanol/PBS (60/40) elution before any further studies were performed.

2.2.5 *In vitro* studies

2.2.5.1 Cell Culture

PC-3 cells were cultured in our laboratory, as per ATCC protocol, in Ham's F-12K medium containing 10% FBS, 2.5 mM L-glutamine, 15 mM HEPES, and 0.5 mM sodium pyruvate. Cells were incubated at 37 $^{\circ}$C at 5% CO_2.

2.2.5.2 Competitive cell-binding studies of BBN peptides

The inhibitory concentrations (IC_{50}) for the peptides (BBN-RR, D-BBN-RR, and BBN-EE) were determined using a PC-3 cell line. Before the day of experiment, PC-3 cells were plated in 6-well plates at a seeding density of 0.5 x 10^6 per well. The next day, the cells were washed with PBS and 1 mL fresh medium was added to each well. The cells were then incubated at 37 °C for 1 h in the presence of ^{177}Lu-radiolabeled BBN-DOTA (100,000 counts per minute) and at varying concentrations (3.33 10^{-12} to 3.33 10^{-6} M) of BBN-RR, D-BBN-RR, or BBN-EE, with each concentration point made in duplicate. At the end of the incubation period, the cells were washed three times with PBS to remove any unbound peptide. Cells were incubated with acidic buffer (50 mM glycine-HCl/0.1 M NaCl buffer, pH = 2.8) for 5 min and lysed with SDS to collect surface-bound and internalized fractions for the peptide, respectively. The radiation signal was measured using a gamma counter. The experiment was done in two biological replicates. One-binding site model Graphpad PRISM 7 (U.S.) was used to obtain the corresponding curves and determine the IC_{50} values.

2.2.5.3 Cellular uptake studies of BBN-HPMA conjugates

Cellular uptake studies were performed for all BBN-HPMA conjugates. PC-3 cells were plated in 6-well plates at a seeding density of 0.5 x 10^6 per well. On the day of the experiment, the medium was replaced with 1 mL of fresh medium and then 100,000 cpm of the desired BBN-HPMA conjugate (dissolved in 100 µL medium) was added per well. Cells were then incubated at 37 °C/5% CO_2 for 30 min, 1 h, 2 h, 3 h, and 4 h (five wells per compound per time point). At the end of each time point, cells were washed three times with PBS followed by incubating with an acidic buffer (0.2 M glycine-0.15 M NaCl, pH = 2.8) for 5 min to isolate the surface-bound radioactivity and SDS to lyse the cell and obtain the internalized radioactivity. A gamma counter was used to measure the radioactivity signal. Each experiment was done in two biological replicates.

2.2.5.4 Competitive blocking experiments of BBN-HPMA conjugates

Competitive blocking experiments were performed for P-RR-2, P-RR-3, P-D-RR-3, and P-RR-EE-1. BBN-Anta, a known GRPR antagonist (172), was used as a blocking agent. PC-3 cells were seeded on 6-well plates at a seeding density of 0.5 x 10^6 cells/well. The following day, a fresh medium containing 300 µM of BBN-Anta was added, and the desired BBN-HPMA conjugate (five wells per compound) was added. After 1 h incubation at 37 °C/5% CO_2, the cells were washed three times with PBS, incubated with the previously described acidic buffer (pH = 2.8) for 5 min and SDS to obtain surface-bound and internalized activity, respectively, and the radioactivity was measured. Each experiment was performed in two biological replicates.

2.2.5.5 Confocal microscopy of BBN-HPMA conjugates

Confocal microscopy studies were performed for P-RR-3 and P-D-RR-3. PC-3 cells were incubated in a 4-well Lab-Tek II chamber coverglass (Thermo Scientific) at a seeding density of 5 x 10^4 cells per well (two wells per compound). The next day, the cells were washed three times with PBS and then, a fresh 400 µL medium containing an equivalent FITC concentration of 6 µM of the desired BBN-HPMA conjugate was added. The cells were incubated for 4 h at 37 °C/5% CO_2. The cells were then washed three times with PBS and fresh medium containing 150 nM of LysoTracker Red DND-99 was added. After 2 h, the cells were washed three times with PBS and incubated with 1 nM of Hoechst® 33342 dye for 5 min. Finally, the cells were washed with PBS and imaged using an excitation wavelength of 405 nm, 488 nm and 568 nm for blue, green and red excitations, respectively. The intensity of fluorescent signals was quantified using ZEN (blue edition) software.

2.2.6 Biodistribution studies

The biodistribution studies were performed on normal female CF-1 mice weighing ~ 35 g. The mice were randomly divided into five groups (five mice/group). After radiolabeling and purification, 0.37 MBq (10 µCi) of the desired ^{177}Lu-BBN-HPMA conjugate was injected

intravenously via tail. After 4 h, the mice were sacrificed, and their tissues were excised and weighed. The tissue radioactivity was measured using a gamma counter. The percent injected dose (%ID) for each tissue was calculated by dividing the radioactivity of each tissue by the total counts of all excised tissues, the remaining carcass, and the bedding materials. Data are expressed in terms of %ID/g of tissue to normalize differences in tissue masses.

2.2.7 Statistics

Statistical analyses were performed using a two-tailed unpaired Student's t-test (two groups) or one-way ANOVA (more than two groups) with Bonferroni post-tests. A value of $p < 0.05$ was considered statistically significant.

2.3 Results

2.3.1 Design and Synthesis of BBN-HPMA conjugates

Herein, we examine the potential of BBN peptides to enhance the delivery of diagnostic or therapeutic HPMA copolymers to GRPR-positive prostate cancer. To that end, BBN peptides in varying densities and charges were incorporated into the polymeric construct to examine how these factors affected *in vitro* and *in vivo* performance. Through this incorporation, the resulting BBN-incorporated HPMA copolymers (BBN-HPMA) were either positive (modified with BBN-RR), negative (modified with BBN-EE), or zwitterionic (modified with both BBN-RR and BBN-EE), Figure 2.1 and Figure 2.2.

All of the BBN peptides incorporated into the HPMA copolymers contain the BBN(7-14)NH_2 sequence which is capable of yielding low nanomolar GRPR binding (77). BBN-RR includes two positively charged Arg (R) residues, while BBN-EE contains two negatively charged Glu (E) residues. In the case of BBN-EE, a PEG_2 spacer was included that separates the Glu residues from the GRPR-targeting vector. An earlier attempt to synthesize the above BBN-EE without the PEG_2 spacer resulted in a peptide with poor aqueous solubility. All of the peptides

designed for polymeric integration included a D-Phe(4-F) moiety which allowed for easy quantification of polymer-peptide incorporation by ^{19}F-NMR. Lastly, these peptides included a terminal maleimide group to facilitate incorporation into the HPMA copolymer through thio-maleimide click chemistry.

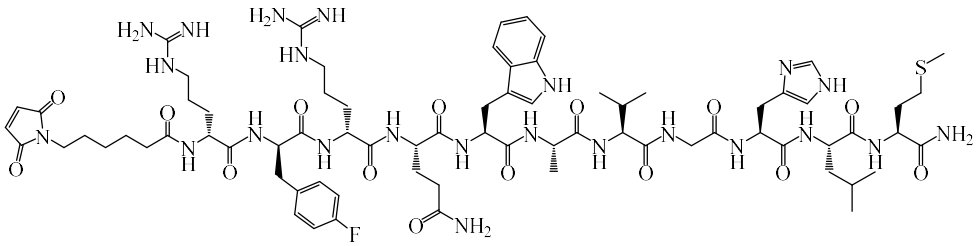

BBN-RR: 6-maleimidohexanoic acid-D-Arg-D-Phe(4-F)-D-Arg-Gln-Trp-Ala-Val-Gly-His-Leu-Met-NH_2

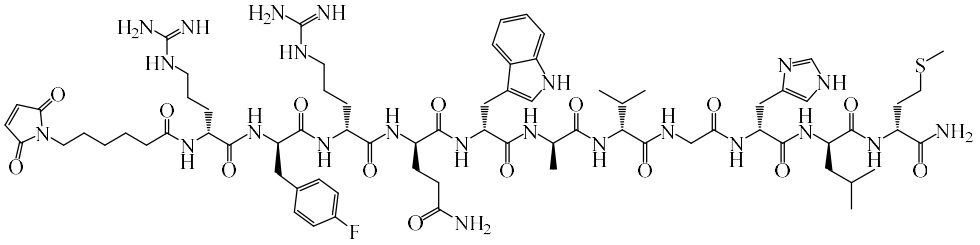

D-BBN-RR: 6-maleimidohexanoic acid-D-Arg-D-Phe(4-F)-D-Arg-D-Gln-D-Trp-D-Ala-D-Val-D-Gly-D-His-D-Leu-D-Met-NH_2

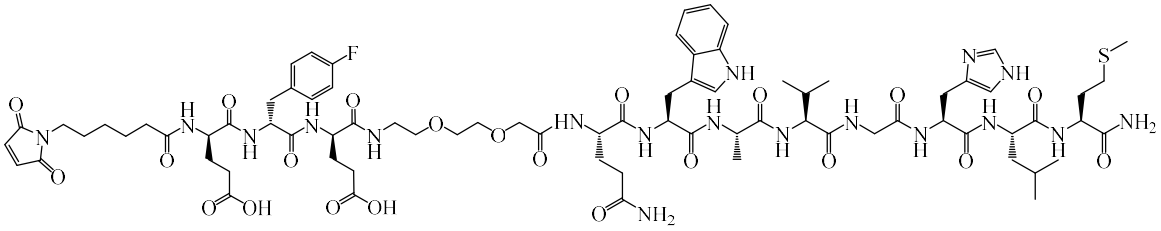

BBN-EE: 6-maleimidohexanoic acid-D-Asp-D-Phe(4-F)-D-Asp-PEG_2-Gln-Trp-Ala-Val-Gly-His-Leu-Met-NH_2

Figure 2.1 Structures of synthesized peptides (BBN-RR, D-BBN-RR, and BBN-EE).

A number of control peptides (D-BBN-RR, BBN-DOTA and BBN-Anta) were also synthesized for the planned studies. For D-BBN-RR, D-configured amino acids were utilized to assemble the BBN(7-14)NH_2 sequence. This provided a matched control with the same physiochemical properties of the BBN-RR without the capability to bind to the GRPR. BBN-DOTA and BBN-Anta (a known GRPR antagonist) were generated as controls and utilized in the investigation of the GRPR binding of the polymeric constructs. All of the peptides described above were successfully synthesized using SPPS. The yields and mass spectrometric identifications of the resulting peptides are provided in Table 2.2**Error! Reference source not found.Error! Reference source not found.**. The corresponding MS spectra for these peptides can be found in Figure 2.3.

The two batches of HPMA copolymers (HPMA-SS-1 and HPMA-SS-2) were successfully synthesized using RAFT polymerization chemistry (Figure 2.2). Deprotection of the disulfides with TCEP yielded the free thiols. The molecular weight of the resulting HPMA copolymers were 43.4 (Đ = 1.1) and 35.1 (Đ = 1.06) kDa for HPMA-SH-1 and -2, respectively. Corresponding free thiol content for the two copolymer batches were 18.5 and 16.4 mol%, respectively. Incorporation of the BBN peptides into the HPMA copolymers were carried out using thiol-maleimide click chemistry. Variation in peptide loading onto the copolymer was accomplished by adjusting the concentration of the BBN peptide (Table 2.1) for the conjugation reaction. The HPMA-SH-1 was utilized to yield P-RR and P-RREE copolymer constructs while HPMA-SH-2 was utilized to generate the P-EE copolymers. Deprotection of the tert-butyl protecting groups from the DOTA chelator was achieved using TFA to give the final polymeric constructs. The composition of the various HPMA copolymers generated are provided in Table 2.3. Representative examples of ^{1}H and ^{19}F-NMR spectra utilized in the characterization of the polymeric constructs are given in Figure 2.4 and Figure 2.5. Depending on the extent of the peptide incorporation, molecular weights of the HPMA copolymers varied from 55.0 – 117.80 kDa with BBN peptide content ranging from 0.12 – 0.39 mmol/g polymer. The radiolabeling of BBN-incorporated HPMA copolymers was accomplished

by incubation with $^{177}LuCl_3$ in DI water at 90°C for 60 min. These radiolabeling conditions gave moderate radiochemical yields of 55 - 75%.

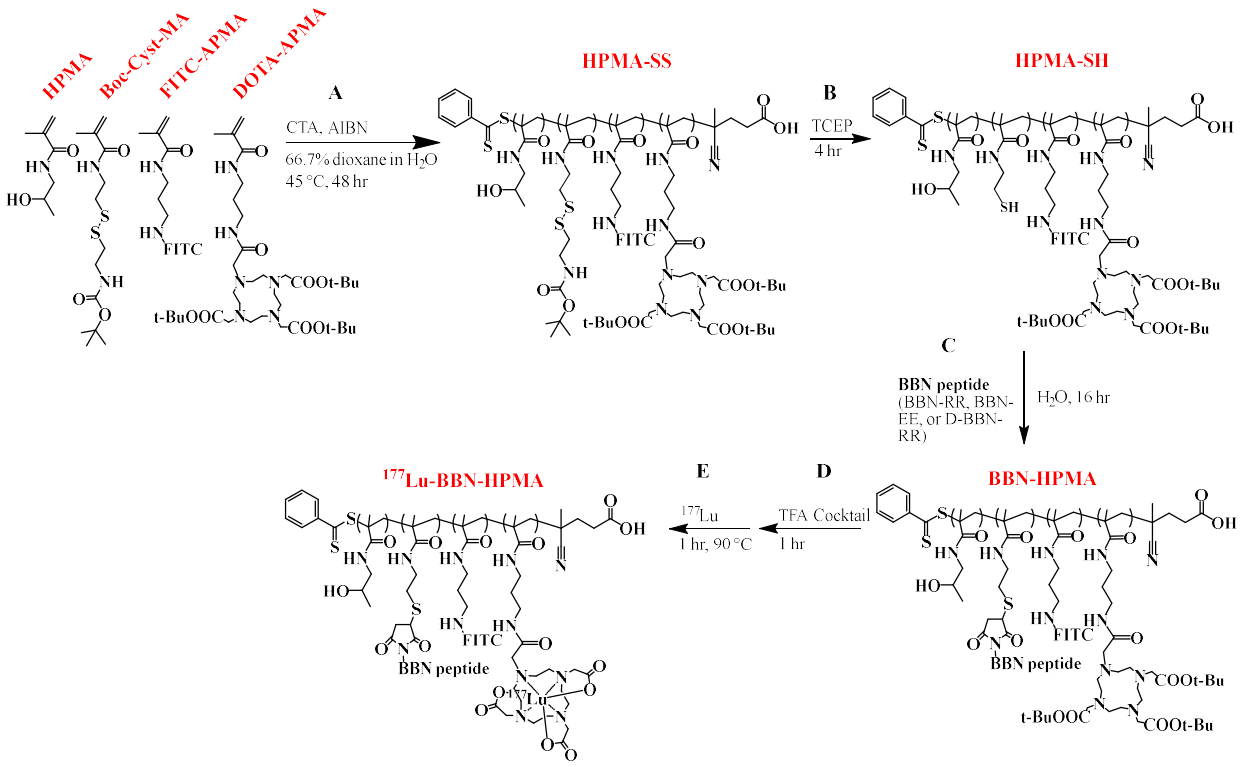

Figure 2.2 Schematic representation of A) RAFT polymerization, B) Thiol deprotection, C) BBN peptide conjugation, D) Deprotection of DOTA-tris(tBu) and E) radiolabeling with ^{177}Lu.

Table 2.2 Mass spectrometric identification and IC_{50} values of the peptides

Peptides	Molecular formula	Mass calculated[a]	Mass found[a]	Yield (%)	IC_{50} (nM)
BBN-RR	$C_{74}H_{108}FN_{23}O_{15}S$	1610.8	1610.6	21.7	18.6 ±1.0
D-BBN-RR	$C_{74}H_{108}FN_{23}O_{15}S$	1610.8	1610.7	19.8	NI[b]
BBN-EE	$C_{78}H_{109}FN_{18}O_{22}S$	1701.8	1701.4	17.1	31.2 ±1.7
BBN-DOTA	$C_{71}H_{115}N_{25}O_{18}S$	1638.8	1638.6	18.3	-
BBN-Anta	$C_{49}H_{69}N_{13}O_9$	984.1	984.3	25.4	-

[a] Mass calculated and found are for $[M+H]^+$

[b] No competitive inhibition was observed at the highest concentration used (3.33 μM)

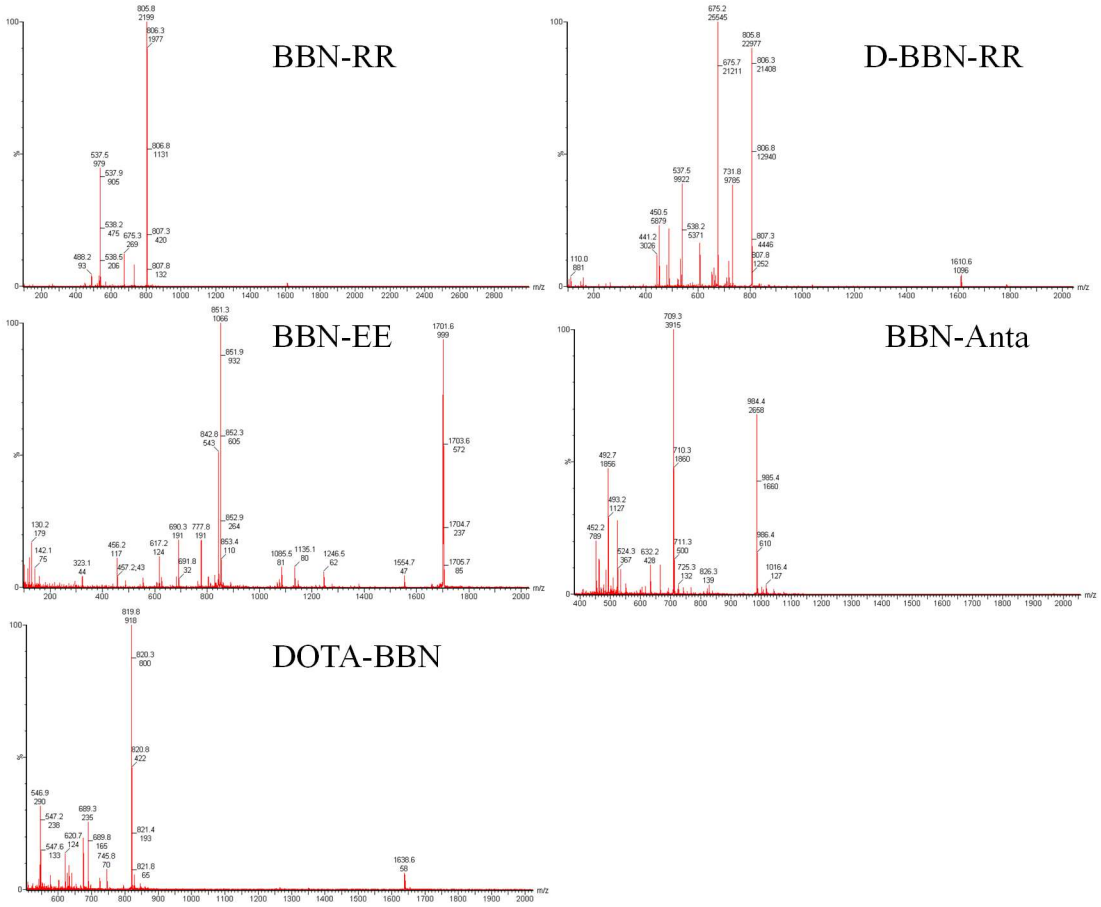

Figure 2.3 MS spectra of the synthesized BBN peptides.

Table 2.3 Characteristics of HPMA copolymers

Copolymers	MW[c] (kDa)	Đ	APMA-Cys-Boc[d] (Mol.%)	FITC[e] (Mol.%)	DOTA[f] (Mol.%)	Total peptide weight (%)	Peptide content by type[j] (mmol/g polymer)		
							BBN-RR	**D-BBN-RR**	**BBN-EE**
HPMA-SS-1	50.6	1.0		0.24	0.54				
HPMA-SH-1[a]	43.5	1.1	18.5						
HPMA-SS-2	40.0	1.07							
HPMA-SH-2[b]	35.1	1.06	16.5	ND	ND				
P-RR-1	55.0	1.11				19.8	0.12		
P-RR-2	67.1	1.06				38.5	0.24		
P-RR-3	93.5[j]					53.5	0.33		
P-RR-4	117.8[j]					63.1	0.39		
P-D-RR-3	99.2	1.10				50.6		0.314	
P-EE-1	42.3	1.06				23.6			0.14
P-EE-2	62.6	1.10				37.9			0.22
P-EE-3	70.2	1.09				54.5			0.32
P-EE-4	78.4	1.06				61.8			0.36
P-RREE-1	88.2	1.09				51.0	0.19		0.11
P-RREE-2	101.2[j]					57.0	0.17		0.18

[a] Intermediate polymer for the synthesis of P-RR-1, P-RR-2, P-RR-3, P-RR-4, P-D-RR-3, P-RREE-1, and P-RREE-2

[b] Intermediate polymer for the synthesis of P-EE-1, P-EE-2, P-EE-3, and P-EE-4

[c] Estimated by gel permeation chromatography

[d] Determined by Ellman's essay

[e] Determined by UV/Visible spectrophotometry

[f] Determined by ^{1}H-NMR spectroscopy

[j] Determined by ^{19}F-NMR spectroscopy

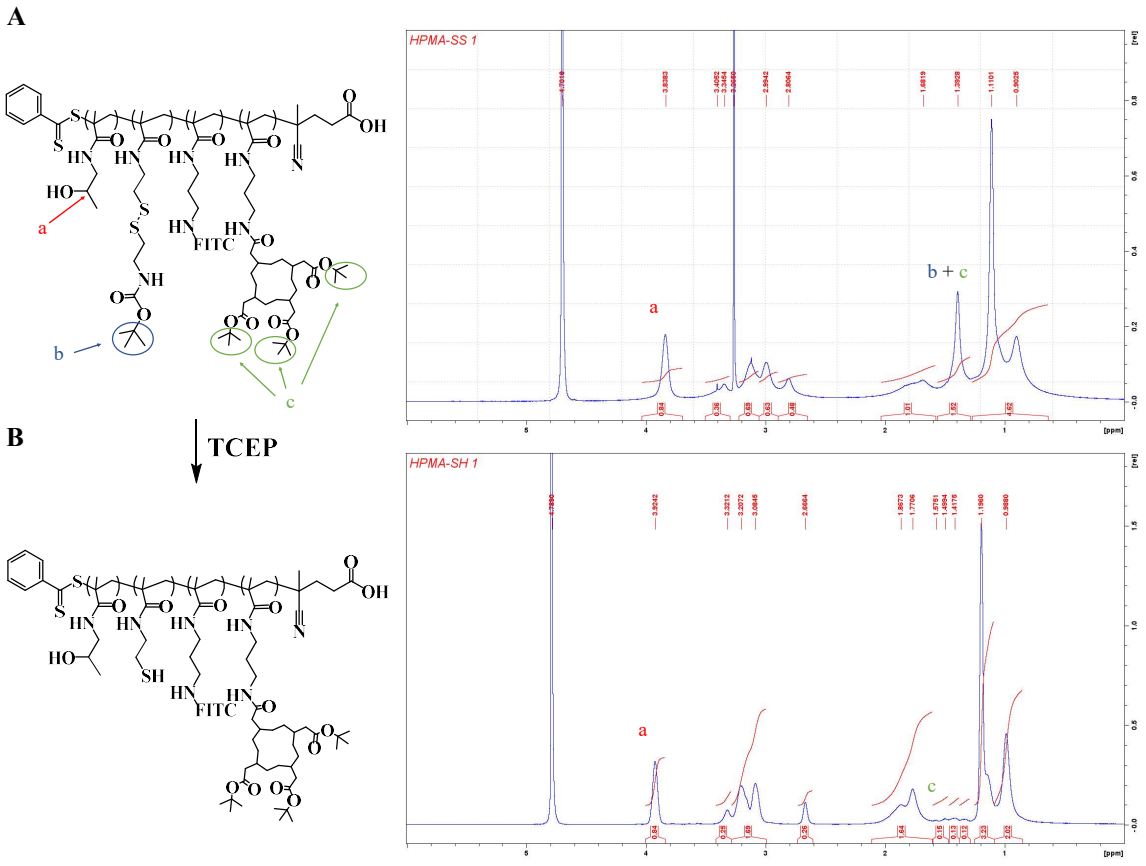

Figure 2.4 ^{1}H-NMR spectra of HPMA-SS (top) and HPMA-SH 1 (bottom) using D2O.

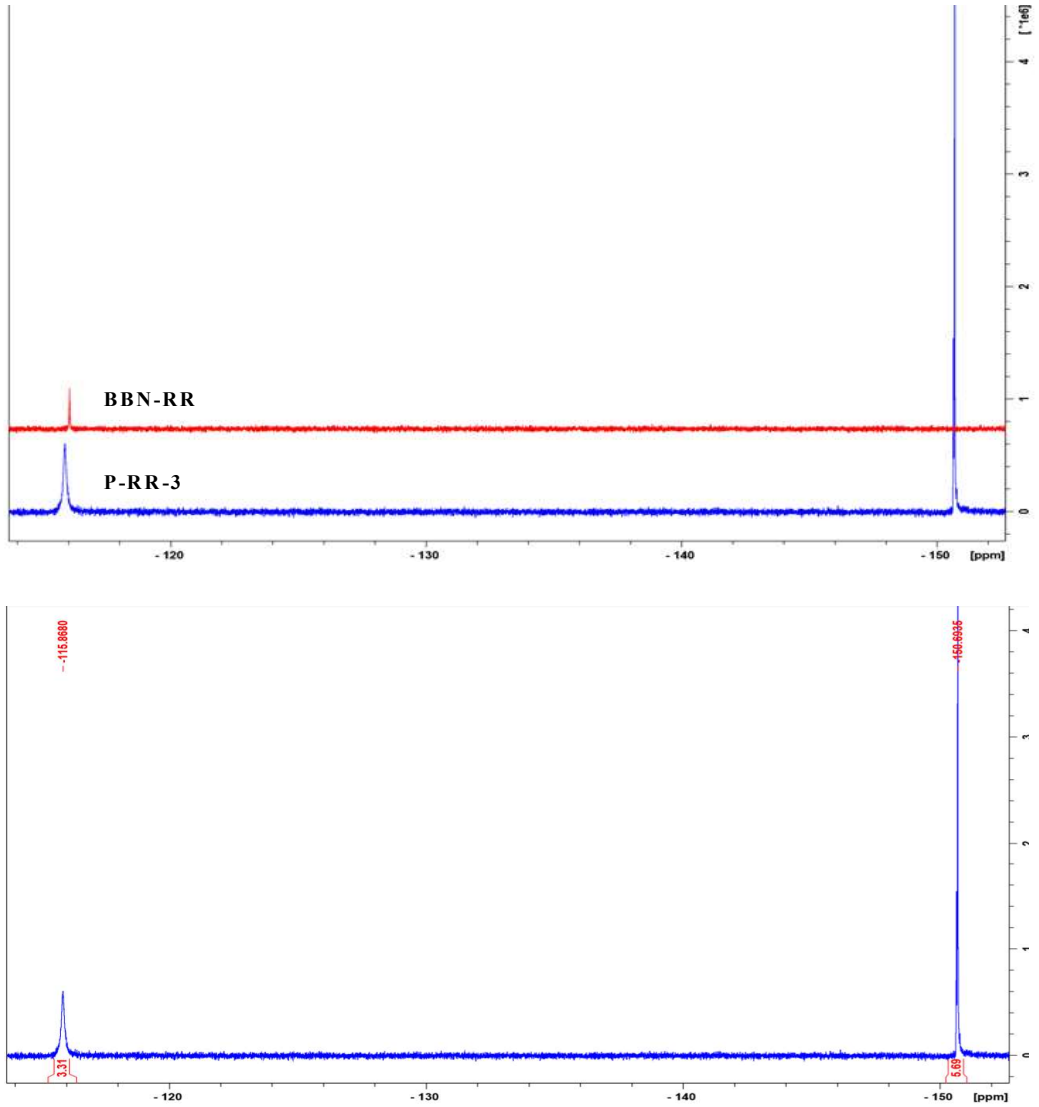

Figure 2.5 ^{19}F-NMR spectra of both BBN-RR and P-RR-3. The bottom spectrum shows P-RR-3 (9.8 mg) is integrated to 3.31 µmol in presence of 5.69 µmol of NaBF4 (control).

2.3.2 *In vitro* studies

In vitro studies were conducted in the GRPR-positive, PC-3 human prostate cancer cell line (173). Competitive binding studies (Table 2.2) were conducted for BBN-RR, BBN-EE and D-BBN-RR vs BBN-DOTA (positive control radioligand) to establish the GRPR affinity of the three experimental peptides prior to polymeric incorporation. The GRPR-affinities (IC_{50} values) of BBN-RR and BBN-EE were 18.6 ± 1.0 and 31.2 ± 1.7 nM ($p < .001$), respectively. As expected, no GRPR-affinity for the D-BBN-RR was observed at the tested concentrations (Table 2.2).

Once the GRPR-affinities of the BBN peptides were established, the cellular uptake of the BBN-HPMA conjugates were investigated over 4 h using the PC-3 cell line (Figure 2.6). For the positive BBN-HPMA copolymers, uptake of P-RR-1 was negligible over the time frame, see Fig. 3A. However, as BBN-RR incorporation increased in the polymer construct, marked increases in cellular uptake rates were seen. By the end of the 4 h period, the trend of P-RR-4, P-RR-3, P-RR-2 and P-RR-1 was observed to have 20, 17, 7 and 0.7 of the added radiolabeled construct internalized, respectfully. Interestingly, the negative control P-D-RR-3, which has a similar peptide content compared to P-RR-3 but has no GRPR binding capabilities, had approximately half (9%) of the cellular uptake of P-RR-3. This suggests that GRPR-mediated uptake is not the only mechanism by which these constructs enter cells. The negatively charged BBN-HPMA constructs (P-EE-1, P-EE-2, P-EE-3, and P-EE-4) had distinctly different internalization profiles, see Figure 2.6B. With exception to P-EE-4, all of the negatively charged polymeric constructs exhibited less than 0.2% of internalization over the 4 h time frame. P-EE-4, which contained the largest BBN-EE peptide content, had just less than 0.6% of cellular internalization during that time.

Based on the above results, we decided to examine what impact combining positive (BBN-RR) and negative (BBN-EE) peptides in a single HPMA copolymer had on cellular internalization. Two constructs, P-RREE-1 and P-RREE-2, with similar peptide contents, 0.30 and 0.35 mmol/g polymer, correspondingly, but different positive to negative peptide ratios of approximately 1.7:1 and 1:1 were synthesized. The cellular internalization of these constructs along with P-RR-2 (positive control) were investigated using PC-3 cells, see Figure 2.6C. The cellular uptake profiles for both of these constructs were significantly below that of the control. P-RREE-1 resulted in 1.5% internalization of the radiolabeled polymer over 4 h, while P-RREE-2 exhibited only a 0.2% uptake over the same time frame. This indicates that the inclusion of the negative charged BBN-EE deleteriously impacted cellular uptake with the degree of impact increasing with the amount of BBN-EE incorporated.

Using a GRPR blocking agent, BBN-Anta (300 μM), the impact of GRPR blocking on the cellular internalization of the P-RR-2, P-RR-3, P-RREE-1 and P-D-RR-3 constructs was examined at the 1 h time point, see Figure 2.6D. In the presence of the GRPR-blocking agent, a 60 and 33 % reduction in cellular internalization for P-RR-2 and P-RR-3, correspondingly, was observed. However, no change in cellular uptake was observed for P-RREE-1 and P-D-RR-3 when blocking the GRPR. Based on these results, GRPR-mediated internalization of the BBN-HPMA constructs is only relevant, at least in the context of this study, for the positively charged P-RR constructs. Overall, these results indicate that the percent incorporation and charge of the BBN peptide play an important role in the cellular uptakes of the BBN-HPMA conjugates.

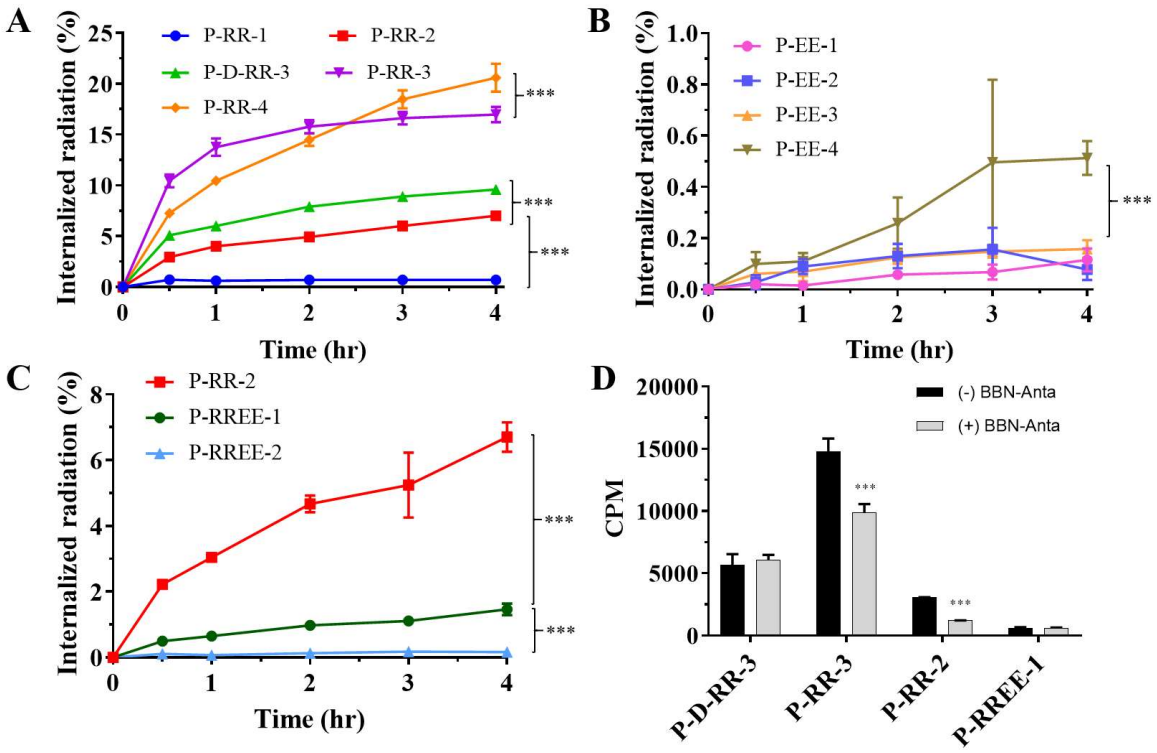

Figure 2.6 Cellular internalization of positive BBN-HPMA conjugates (A), negative BBN-HPMA conjugates (B), zwitterionic BBN-HPMA conjugates (C), and GRPR blocking experiments after 1 h (with or without BBN-Anta) (D). Data expressed as Mean ± SD. *** Indicates significance at $p < 0.001$.

Confocal microscopy studies were performed to examine the uptake pattern of BBN-HPMA constructs that do and do not undergo GRPR-mediated internalization. Specifically, the cellular uptake of P-RR-3 and P-D-RR-3 were examined in PC-3 cells at 4 h post-incubation, see Figure 2.7. Consistent with previous cellular uptake studies, the FITC-labeled (green) P-RR-3, capable of GRPR-mediated uptake, exhibited a two-fold higher uptake in PC-3 cells relative to the P-D-RR-3 which is incapable of GRPR-mediated internalization. Focal points of subcellular accumulation were observed for both polymeric constructs. These accumulation sites overlapped well with the endolysosomal marker (LysoTracker Red). These findings suggest that whether GRPR-mediated or not, the cellular uptake of BBN-HPMA polymeric constructs are internalized through the endocytic pathways.

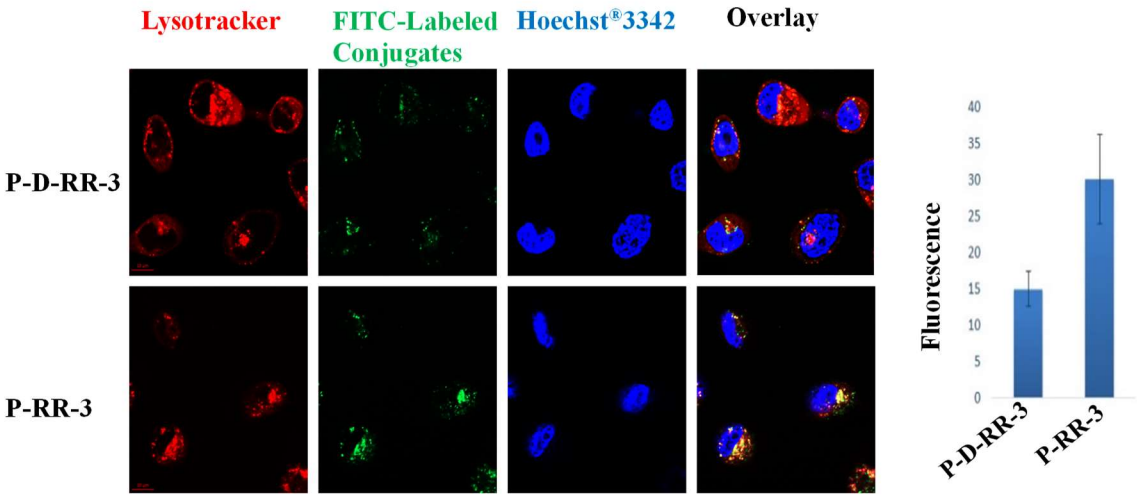

Figure 2.7 Confocal microscopy images of P-D-RR-3 (top) and P-RR-3 after incubation for 4 h. Lysotracker (red), FITC (green) and Hoechst® 33342 dye (blue) visualize endosomal compartments, peptide-polymer conjugates and nucleus, respectively. The corresponding fluorescence signals are shown to the right (mean ± SEM).

2.3.3 Biodistribution studies

Based on our *in vitro* work, only the P-RR constructs demonstrated significant levels of GRPR-mediated internalization. Therefore, we decided to restrict the biodistribution studies to P-RR-1, P-RR-2, P-RR-3, P-RR-4 and P-D-RR-3 (control) using a normal CF-1 mouse model. The results of these biodistribution studies are illustrated in Figure 2.8 and Table 2.4. Blood retention for all conjugates was less than 0.5 %ID/g at 4 h with exception to P-RR-1, which had a markedly higher value of 14.0 ± 0.6 %ID/g ($p < .001$). Liver and spleen uptakes for P-RR-1 (12 ± 3 and 2.8 ± 0.4, respectively) were also substantially lower than the other constructs with values ranging from 39 ± 4 – 57 ± 8 %ID/g for the liver and 16 ± 3 – 121 ± 41 %ID/g for the spleen. The rapid blood clearance and accumulation of the P-RR constructs in the liver and spleen suggest these positively charged polymeric systems are removed from the blood by phagocytic cells of the mononuclear phagocyte system (MPS) (55, 110). Interestingly, doubling of the BBN-RR content from 0.12 mmol/g to 0.24 mmol/g for P-RR-1 and P-RR-2, respectively, led to a marked increase in blood clearance and uptake in MPS-associated organs. In particular, increased spleen uptake of the P-RR constructs correlated well with increasing BBN-RR polymeric content. Overall, these studies demonstrate that the clearance profile of these agents are directly related to BBN-RR content and this observation is mostly likely tied to the charge and size of the constructs.

The mouse pancreas is known to highly express the GRPR and has been utilized as an *in vivo* control for low-molecular-weight GRPR-targeted agents (81, 174). The pancreas uptake of P-RR-1 (1.4 ± 0.3 %ID/g) was significantly ($p < .001$) higher than the other polymeric constructs (< 0.64 ± 0.17 %ID/g). Prior *in vitro* studies demonstrated that P-RR-1 demonstrated poor GRPR-targeting. Therefore, the increased pancreatic uptake of P-RR-1 relative to the other constructs is likely due to the higher blood retention/longer circulation time of the construct.

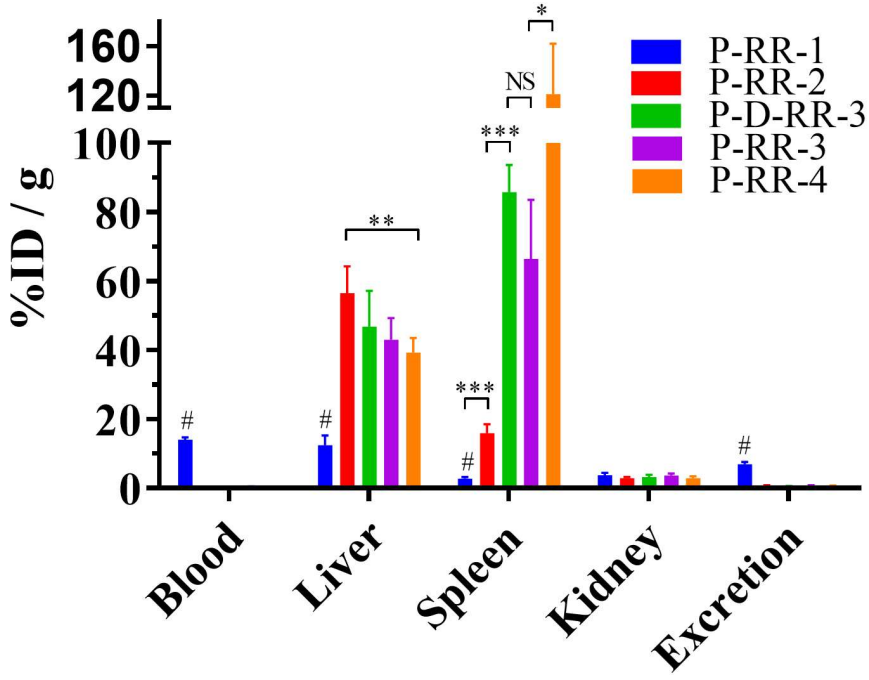

Figure 2.8 Biodistribution profiles (in selected organs) of P-RR-1, P-RR-2, P-D-RR-3, P-RR-3, and P-RR-4 after 4 h in normal mice. # indicates significance ($p < 0.001$) for P-RR-1 in comparison with any other group. NS no significance, * $p < 0.05$, ** $p < 0.01$, *** $p < 0.001$. Data expressed as mean ± SD.

Table 2.4 Biodistribution of BBN-HPMA conjugates in CF-1 female mice after 4 h

Organ/Conjugate	P-RR-1	P-RR-2	P-RR-3	P-D-RR-3	P-RR-4
Blood	14 ± 1	0.20 ± 0.02	0.40 ± 0.14	0.29 ± 0.09	0.28 ± 0.10
Heart	4.1 ± 0.4	1.3 ± 0.3	11 ± 2	3.9 ± 0.8	8.5 ± 2.7
Lung	5.6 ± 1.7	7.1 ± 2.0	22 ± 5	38 ± 4	8.4 ± 3.0
Liver	12 ± 3	56 ± 8	43 ± 6	47 ± 10	39 ± 4
Pancreases	1.4 ± 0.3	0.18 ± 0.03	0.64 ± 0.17	0.43 ± 0.23	0.45 ± 0.18
Stomach	0.82 ± 0.20	0.41 ± 0.15	0.76 ± 0.21	0.58 ± 0.25	0.85 ± 0.44
Spleen	2.8 ± 0.4	16 ± 3	66 ± 17	86 ± 8	121 ± 41
Small intestine	1.6 ± 0.5	0.20 ± 0.03	0.26 ± 0.05	0.24 ± 0.07	0.28 ± 0.12
Large intestine	2.5 ± 1.6	0.43 ± 0.16	0.35 ± 0.16	0.25 ± 0.17	0.29 ± 0.17
Kidney	3.8 ± 0.7	2.8 ± 0.4	3.7 ± 0.5	3.1 ± 0.7	2.8 ± 0.6
Bladder	1.6 ± 0.3	0.34 ± 0.08	0.31± 0.22	0.93 ± 0.81	0.94 ± 0.73
Muscle	0.69 ± 0.05	0.11 ± 0.02	0.33 ± 0.14	0.38 ± 0.43	0.17 ± 0.15
Bone	1.2 ± 0.2	0.75 ± 0.27	0.70 ± 0.39	0.73 ± 0.29	0.73 ± 0.23
Brain	0.51 ± 0.05	0.02 ± 0.01	0.05 ± 0.03	0.05 ± 0.02	0.04 ± 0.03
Tail	3.3 ± 2.8	1.00 ± 0.27	1.24 ± 0.55	1.32 ± 0.56	1.4 ± 0.6
Excretion (% ID)	6.9 ± 0.7	0.67 ± 0.11	0.56 ± 0.32	0.34 ± 0.29	0.53 ± 0.14

Data represented as %ID / g tissue. Values are mean ± SD (n = 5 for all conjugates except P-D-RR-3, n = 4)

2.4 Discussion

Nanomedicines, including drug-polymer conjugates, are able to target tumors through the use of passive and active targeting mechanisms (157, 158). Passive tumor uptake through the enhanced permeability and retention (EPR) effect relies on imperfections (i.e., fenestrations) in the tumor vasculature to allow for the selective delivery of high molecular weight nanocarriers to tumors. For active targeting, incorporation of targeting vectors (e.g., peptides or antibodies) onto the surface or into the structure of nanocarriers allows for the possibility of increased tumor accumulation through active targeting of antigens expressed on the surface of tumor cells and/or in the tumor microenvironment. While active targeting offers the possibility of efficient intracellular delivery through receptor-mediated endocytosis, the ability of targeting ligands to actually increase overall tumor delivery has been generally restricted to constructs with lower molecular size (< 50 nm) (163). HPMA copolymers are one such delivery vehicle (< 20 nm) and have been demonstrated to be able to enhance tumor uptake through the incorporation of small molecules and peptide targeting vectors (175, 176).

The GRPR has been shown to be a clinically validated target for prostate, breast and other cancers (76). Trials have been performed and are currently underway to examine the clinical potential of low-molecular weight GRPR-targeting vectors based on the bombesin peptide (177). Our aim in this study is to exploit BBN(7-14)NH_2, a truncated form of bombesin that is a known GRPR-targeting vector, to examine if its incorporation into HPMA copolymer constructs can enhanced tumor uptake in GRPR-positive cancers. Based on previous reports (105, 178, 179), targeting vector charge and incorporation densities can have significant impact on *in vitro* and *in vivo* performance. To examine these factors, we synthesized HPMA copolymers incorporated with positive (P-RR), negative (P-EE) or a combination of both (P-RREE) charged BBN(7-14)NH_2 constructs. The *in vitro* GRPR-targeting of these polymeric constructs were

investigated in the human PC-3 prostate cancer cell line and the preliminary *in vivo* biodistribution of the constructs were investigated in a normal mouse model.

The GRPR-targeting vectors, BBN-RR and BBN-EE, both demonstrated nanomolar binding affinities to the GRPR. The higher affinity of BBN-RR is likely attributable to the positive charges on the N-terminal side of the pharmacophore which has been observed previously with similar constructs (180). Once incorporated into the HPMA constructs, the GRPR targeting vectors have distinctly different uptake patterns in the PC-3 cell line. The P-RR constructs demonstrated substantially higher uptake relative to P-EE or P-RREE constructs. Incorporation of higher BBN-RR densities promoted cellular uptake while the inclusion of BBN-EE in negative and zwitterionic constructs seemed to inhibit cellular uptake. It is known that the charge of HPMA constructs can have a profound effect on cellular uptake (105). Positively charged constructs are believed to promote surface cell binding/internalization due to favorable electrostatic interactions with the negatively charged plasma membrane.

To determine if the cellular uptake of P-RR constructs were due to charge alone, we completed follow-up studies that examined P-RR-3 to a matched control (P-D-RR-3) that has similar peptide density and charge but is unable to undergo GRPR-mediated internalization. P-D-RR-3 demonstrated roughly one-third the uptake as P-RR-3. Additionally, blocking of the GRPR with a known GRPR antagonist reduced P-RR-3 internalization but, as expected, had no effect on P-D-RR-3. Further analysis by confocal microscopy confirmed these findings and demonstrated that cellular uptake resulted in trafficking to the endolysosomal compartments of the cell. The findings are in accordance with GRPR-mediated internalization (78, 181) and other endocytic routes for HPMA copolymers and other nanomedicine constructs (105, 182). Overall, these studies demonstrate that the internalization of the P-RR-3 constructs are due to both GRPR-mediated uptake and non-specific charge-associated uptake mechanisms. The inability of P-EE and P-RREE constructs to internalize as efficiently as the positively charged analogs suggests that

the negative charge or decreased positive charge of the copolymer constructs inhibit plasma membrane association and, as a consequence, inhibit the ability to bind to and be internalized by the GRPR.

Preliminary biodistribution studies of the P-RR constructs were examined in a normal CF-1 mouse model at the 4 h time point. With exception to P-RR-1, all of the constructs denoted rapid clearance from the blood and substantial uptake in MPS-associated tissues, particularly the liver and spleen. P-RR-1 was the only construct with significant blood pool retention at 4 h suggesting that the lower peptide density reduces recognition and clearance by the MPS. This observation is consistent with other peptide-incorporated nanomedicine constructs (179, 183). It suggests the higher peptide content of the copolymers increases opsonization and recognition by the phagocytic cells of the MPS (184).

The pancreas is known to contain a high density of the GRPR and has been utilized as a control tissue to examine *in vivo* GRPR-targeting (81, 174). P-RR-1 did demonstrate higher levels (1.4 ± 0.3 %ID/g) of pancreatic uptake compared to the other constructs. However, this level of uptake is far below what is normally seen with other low and high molecular weight GRPR-targeted agents (80, 81, 160, 185). Additionally, the blood to pancreas ratio for P-RR-1 (10:1) is similar to analogous HPMA copolymers (~ 6:1 to 10:1) we have previously reported that are not active targeting (117, 186). Given this and the relatively poor *in vitro* GRPR-targeting capabilities of P-RR-1 lead us to conclude that the higher pancreatic signal for P-RR-1 corresponds to a substantially higher blood pool activity and not GRPR-mediated uptake. Overall, the poor *in vitro* GRPR-targeting profile of P-RR-1 and the rapid MPS clearance of the remaining P-RR constructs prevented us from pursuing follow up studies in the GRPR-positive, PC-3 mouse model.

2.4.1 Conclusion

In this study, BBN-modified HPMA copolymer conjugates were synthesized and investigated to examine their GRPR-targeting capabilities. The BBN(7-14)NH_2 pharmacophore

was modified with either positively-or negatively-charged linkers before conjugation to HPMA copolymers. Our *in vitro* studies showed that both the amount of BBN and the charge of the conjugate has a significant effect on GRPR-mediated internalization in PC-3 cells. Positive HPMA copolymer conjugates demonstrated increasing cellular internalization with increase BBN peptide content and charge. In contrast, the incorporation of negatively charged BBN peptides had a deleterious effect on GRPR-mediated internalization. However, the *in vivo* biodistribution profiles of the positive conjugates in normal mice demonstrated rapid recognition and clearance by the MPS. Overall, these results indicate that the modification of HPMA copolymers with BBN peptides could be a promising approach to exploit the GRPR-overexpression in cancers but the effects of peptide content and charge on MPS recognition and clearance should be carefully considered.

3 Chapter 3. Bioorthogonal pretargeting of multi-block cathepsin S-cleavable HPMA copolymers: *In vitro* and *in vivo* evaluations for improved ovarian cancer treatment

3.1 Introduction

Nanosized delivery systems (e.g., polymeric conjugates, micelles, and liposomes) has been a promising approach in the development of more effective therapies for cancer (50). These platforms are capable of multifunctional applications and are designed to incorporate substantial quantities of diagnostic and/or therapeutic agents by physical entrapment or chemical conjugation. These nanomedicine constructs are able to selectively deliver their payload to tumors by means of the enhanced permeability and retention (EPR) effect (158), which is associated with the abnormalities of the tumor vasculature and lymphatic vessels. To date, numerous nanomedicines have already been clinically approved for treating different types of cancers, with many others under clinical evaluations (187). However, the development of drug delivery platforms for nuclear imaging or targeted radionuclide therapeutic applications has been a more dormant area of research. While exceptional work by numerous laboratories has demonstrated the potential of radionuclide-incorporated nanomedicine platforms (173, 188-191), the clinical translation of these systems has been hampered by their slow pharmacokinetics and sites of non-target accumulation (e.g., normal liver and spleen) (50). This is particularly the case for radiotherapeutic drug delivery platforms which often have significant dose-limiting toxicities that prevent the administration of radiative doses capable of achieving the desired therapeutic outcomes.

To address dose-limiting radiotoxicity issues and the poor overall tumor-non-target (T/NT) ratios exhibited by nanomedicine and other high-molecular weight radiotherapeutics, pretargeting has become a strategy of interest (90, 94, 192, 193). This two-step process relies on highly efficient

in vivo bioorthogonal conjugation chemistry to lower non-target radiotoxicity while still yielding selective tumor targeting. An example of this bioorthogonal chemistry is the inverse electron-demand Diels–Alder (IEDDA) reaction between trans-cyclooctene (TCO) and 1,2,4,5-tetrazine (TZ), which can exhibit outstanding reaction kinetics (second-order rate constants (K_2) of up to 10^6 M^{-1} S^{-1}) (73). In practice, these very large rate constants mean that this conjugation reaction is very efficient even at tracer level quantities of radiopharmaceuticals. The first step in this process involves administration of a non-radiolabeled, tumor targeted construct (e.g., antibody or drug delivery system) functionalized with the necessary component for bioorthogonal conjugation (e.g., TCO). In the second step, after allowing the necessary time (e.g., 2 – 3 days) for the high molecular weight construct to achieve sufficient T/NT ratios (192), a low-molecular weight radiotherapeutic is administered that contains the complementary functionality (e.g., TZ) needed for bioconjugation. Upon encountering the high-molecular weight construct, the small molecule radiotherapeutic will be sequestered by irreversible covalent bond formation between the bioorthogonal functional groups (e.g., TCO/TZ) contained in each component. The uncaptured pretargeted small molecule radiotherapeutic will be quickly cleared from the body, typically with plasma half-life lives on the minutes timescale (88, 194). In this manner, substantial decreases in blood circulation times and increases in T/NT ratios can be achieved relative to direct-labeled high-molecular weight constructs. Recent examples of this approach applied to nanomedicine platforms have shown promise and yielded substantial gains in T/NT ratios due predominately to a lower blood retention profile (90, 195, 196). Even with these exciting gains due to pretargeting, significant amounts of mononuclear phagocyte system (MPS)-associated tissue retention (e.g., liver and spleen) have been observed and this sequesterization impedes the translative potential of these systems as radiotherapeutics.

The design and synthesis of biodegradable polymers as a way of controlled drug release and decreasing long-term retention and associated toxicities has been an active area of research (197, 198). Our laboratory (117, 120) and others (118, 199, 200) have explored biodegradable

polymer conjugates based on N-(2-hydroxypropyl)methacrylamide (HPMA) copolymers. Recently, we reported the development of an HPMA copolymer that was selective for degradation by cathepsin S (Cat S), a cysteine protease that is highly expressed in certain immune cells (e.g., macrophages and monocytes) responsible for the MPS-associated uptake of HPMA copolymers and other drug delivery platforms (117, 120). Using this Cat S-degradable HPMA copolymer, a significant reduction in the MPS-associated retention (e.g., blood, liver, and spleen) was observed without substantially impacting tumor uptake or retention in a pancreatic cancer model. This enhanced clearance in non-target tissues led to significant (2- to 3-fold) gains in T/NT ratios and represented an interesting pathway to improve the clinical potential of nanomedicine-based radiopharmaceuticals.

Herein, we explore the potential of this Cat S-degradable HPMA copolymer design in the context of pretargeting using the IEDDA biorthogonal reaction. Specifically, we designed Cat S-biodegradable, TCO-incorporated HPMA copolymers and small molecule TZ-based radiotherapeutic. Our hypothesis was that the Cat S-degradable HPMA copolymer design could reduce non-target uptake of the TCO-incorporated platform and lower the non-target tissue sequestration of the administered TZ-based radiotherapeutic. If successful, the reduced non-target uptake, along with other advantages (e.g., large TCO payload), could make polymer conjugates and other nanomedicine-based constructs more attractive for the development of radiotherapeutics for oncology. In this manuscript, the synthesis and characterization of the two-component pretargeting system, TCO-incorporated HPMA copolymer and the TZ-based radiotherapeutic "chaser agent", is described. Additionally, the influence of the molecular weight of the copolymer and the type of TZ (tetrazine versus methyltetrzaine) on the kinetics of the IEDDA reaction is explored. Lastly, the *in vivo* performance of the CatS-biodegradable, TCO-incorporated HPMA copolymers is evaluated in comparison to a non-biodegradable control using an OVCAR-3 subcutaneous ovarian cancer model.

3.2 Materials and methods

3.2.1 Chemicals

If not otherwise indicated, all solvents used for polymer reactions and silica gel purification were ACS grade and obtained from Fisher Scientific (U.S.). Water was deionized using a Milli-Q® Integral Water Purification System (Millipore Corp., U.S.). Acetonitrile (ACN) and formic acid were HPLC grade and purchased from Fisher Scientific (U.S). Dichloromethane (DCM), N,N-dimethylformamide (DMF), trifluoroacetic acid (TFA) were peptide synthesis grade and purchased from Fisher Scientific (U.S). Fluorescein isothiocyanate (FITC), 1-ethyl-3-(3-dimethylaminopropyl)carbodiimide (EDC), N-hydroxysuccinimide (NHS), triisopropylsilane (TIS), 4-cyano-4-(phenylcarbono-thioylthio)pentanoic acid (CTA 1), 2,2′-Azobis(2-methylpropionitrile) (AIBN), tris(2-carboxyethyl)phosphine (TCEP), ethylenediaminetetraacetic acid (EDTA), N-Boc-ethylenediamine, N,N′-Diisopropylcarbodiimide (DIC), and 2,3,5,6-Tetrafluorophenol (TFP) were purchased from Sigma-Aldrich (U.S). Cis-cyclooct-4-enol (CCO) was purchased from Click Chemistry Tools (U.S.). (1-Cyano-2-ethoxy-2-oxoethylidenaminooxy)dimethylamino-morpholino-carbenium hexafluorophosphate (COMU) was purchased from Chem-Impex International (U.S.). N-(2-Hydroxypropyl)methacrylamide (HPMA) and N-(3-Aminopropyl)methacrylamide (APMA) were obtained from Polysciences (U.S.). Fmoc-Gly-OH and Fmoc-D-Gln(trt)-OH were purchased from NovaBiochem (U.S.) and eMolecules (U.S.), respectively. N,N-Diisopropylethylamine (DIEA) was obtained from ChemPep (U.S.). Fmoc-$(PEG)_2$-COOH and Fmoc-$(PEG)_4$-COOH were purchased from NovaBiochem (U.S.). Fmoc-D-Asp(OtBu)-OH, 2,2,2-Trifluoroethylamine hydrochloride, and glycolic acid were purchased from TCI America (U.S.). 1,4,7,10-Tetraazacyclododecane-1,4,7,10-tetraacetic acid mono-N-hydroxysuccinimide ester (DOTA-NHS-ester) was purchased from Macrocyclics (U.S.). Tetrazine-NHS ester, methyltetrazine-NHS ester, and TCO-PEG4-NHS ester (TCO-A-NHS) were purchased from BroadPharm (U.S.). A 2000-kDa amino dextran (AD2000 x 750) was purchased

from FinaBio (U.S.). Piperidine, pyridine, phenol, Fmoc-Gly-Wang resin, sodium dodecyl sulfate (SDS), and dithiothreitol (DTT) were purchased from Sigma-Aldrich (U.S). Phosphate buffered saline (PBS) and 1-piperazineethanesulfonic acid (HEPES) were purchased from Fisher Scientific (U.S.). RPMI-1640 Medium and fetal bovine serum (FBS) were obtained from Gibco (U.S.). Bovine insulin was obtained from Cell Applications Inc. (U.S.). Human cathepsin S recombinant protein was purchased from R&D Systems (U.S.).

3.2.2 Instrumentation

A Liberty microwave peptide synthesizer (CEM, U.S.) was used to synthesize peptides via solid phase peptide synthesis (SPPS). Equipped with a Waters 2489 absorption detector and a Waters Qtof Micro electrospray ionization mass spectrometer, a Waters (U.S.) e2695 system was used to perform reversed phase-high performance liquid chromatography/mass spectrometry (RP-HPLC/MS) analyses. A Phenomenex (U.S.) Jupiter C12 Proteo 250 x 10.0 mm semiprep column was used to purify the desired molecules. Evaluation and purification of radiolabeled conjugates were performed on a Waters 1515 binary pump equipped with a Waters 2489 absorption detector and a Bioscan (U.S.) Flow Count radiometric detector system. A Bruker Avance-III HD 500 MHz instrument (U.S.) was used to record ^{1}H-NMR, ^{13}C-NMR, and ^{19}F-NMR spectra using either deuterated dimethyl sulfoxide, deuterated chloroform, or deuterium oxide as a solvent. Weight and size measurements of polymers were performed using a Viscotek TDA max system (Malvern Instruments Inc., U.S.) equipped with Shodex Asahipak GF-510 HQ GPC column (TDA-SEC). Biochrom WPA Biowave II UV/Visible Spectrophotometer was obtained from Biochrom (U.S.). A Multi-Wiper nuclear medicine gamma counter (LTI, U.S.) was used for counting the activity when conducting kinetic experiments utilizing HPMA copolymers. Gamma decay detection of injected radiolabeled constructs was performed using NaI (Tl) well detector constructed by AlphaSpectra Inc. (U.S.).

3.2.3 synthesis and characterization

3.2.3.1 Synthesis of TZ intermediates and TZ final compounds

3.2.3.1.1 Synthesis of Fmoc-PEG_2-Boc

Fmoc-PEG_2-COOH (300 mg, 0.778 mmol) was dissolved in 10 mL DCM. To this was added a solution of EDC (149 mg, 0.778 mmol) and NHS (99.0 mg, 0.86 mmol) in 10 mL DCM followed by stirring for 2 h. To this mixture was added a solution of N-Boc-ethylenediamine (124.64 mg, 0.778 mmol) in 10 mL DCM and followed by the addition of DIEA (273 µL, 1.56 mmol). The reaction mixture was stirred at room temperature. After 18 h, the mixture was partitioned between DCM (100 mL) and diluted aqueous HCL (100 mL). The organic layer was washed three times with water and dried over $MgSO_4$. The organic solvent was evaporated under vacuum and the product was purified by silica gel chromatography (1:4 ethyl acetate/hexane) to afford Fmoc-PEG_2-Boc as a white solid (291.2 mg, 0.552 mmol, 71.0% yield).

3.2.3.1.2 Synthesis of NH_2-PEG_2-Boc

Fmoc deprotection of Fmoc-PEG_2-Boc (100 mg, 0.19 mmol) was carried out in 3 mL of 20% piperidine in DCM. After 20 min, the product was precipitated in cold ethyl ether, filtered, and washed three times with ethyl ether to yield a white solid (48.82 mg, 0.16 mmol, 84.2%).

3.2.3.1.3 Synthesis of DOTA-PEG_2-Boc

DOTA-NHS-ester (60.16 mg, 0.079 mmol) was dissolved in 300 µl anhydrous DMF. To this solution was added drop-wise a solution of NH_2-PEG_2-Boc (20 mg, 0.066 mmol) in 300 µL anhydrous DMF followed by the addition of DIEA (28.88 µL, 0.165 mmol). The reaction mixture was stirred at room temperature for 18 h. The product was precipitated in cold ethyl ether and purified by RP-HPLC/MS using an 88% to 80% gradient separation with solvents consisting of solvent A (0.1% formic acid in DI water) and solvent B (0.1% formic acid in ACN) to afford a white solid (34.56 mg, 0.05 mmol, 75.8%).

3.2.3.1.4 Synthesis of DOTA-PEG2-NH2

DOTA-PEG_2-NH_2 was obtained by the removal of the Boc group from DOTA-PEG_2-Boc (30 mg, 0.043 mmol) using 95% TFA in DCM solution. The mixture was stirred at room temperature for 1 h. The product was precipitated in cold ethyl ether, filtered, washed three times with ethyl ether to afford 21.9 mg (0.037 mmol, 86.1%) of the product.

3.2.3.1.5 Synthesis of DOTA-TZ probes

DOTA-PEG_2-NH_2 (10 mg, 0.017 mmol) was dissolved in 300 µL anhydrous DMF and a solution of methyltetrazine-NHS ester (8.5 mg, 0.026 mmol) in 200 µL anhydrous DMF was added followed by the addition of DIEA (7.4 µL, 0.042 mmol). The reaction mixture was stirred at room temperature for 6 h. The crude product was precipitated in cold ethyl ether. The product was purified by RP-HPLC/MS using 90% to 80% gradient separation (over 15 min time period) with solvents consisting of solvent A (0.1% formic acid in DI water) and solvent B (0.1% formic acid in ACN) to afford DOTA-TZ-1 as a pink solid (10.1 mg, 0.0126 mmol, 73.6%). DOTA-TZ-2 was similarly synthesized using tetrazine-NHS ester (8.1 mg, 0.026 mmol) and purified by RP-HPLC/MS using 92% to 82% gradient separation to afford a pink solid (9.3 mg, 0.0118 mmol, 69.4%).

3.2.3.2 Synthesis of TCO intermediates and TCO final compounds

3.2.3.2.1 Synthesis of Fmoc-D-Asp(OtBu)-NH-F_3 and Fmoc-D-Asp(OH)-NH-F_3

Fmoc-D-Asp(OtBu)-OH (500 mg, 1.215 mmol) was dissolved in 10 mL DCM and solutions of EDC (233 mg, 1.215 mmol) in 5 mL DCM and NHS (154 mg, 1.34 mmol) in 5 mL DCM was added, and the mixture was stirred for 2 h. A solution of 2,2,2-Trifluoroethylamine hydrochloride (164.66 mg, 1.215 mmol) in 10 mL DCM was added followed by the addition of DIEA (424 µL, 2.43 mmol). The reaction mixture was stirred at room temperature for 18 h then partitioned between dilute aqueous HCL (100 mL) and DCM (100 mL). The organic layer was washed three times with water (50 mL), dried over $MgSO_4$, and evaporated under vacuum. The

product was purified by silica gel chromatography (1:9 ethyl acetate/hexane) to afford Fmoc-D-Asp(OtBu)-NH-F_3 as a white solid (411 mg, 0.94 mmol, 71% yield).

The intermediate Fmoc-D-Asp(OtBu)-NH-F_3 (350 mg, 0.82 mmol) was then added to a solution consisting of 95:5 TFA/DCM (3 mL). After stirring for 2 h, the mixture was concentrated under vacuum, diluted in DCM and loaded on a silica gel column using (1:1 ethyl acetate/hexane) to afford Fmoc-D-Asp(OH)-NH-F_3 as a white solid (310 mg, 0.71 mmol, 86.1%).

3.2.3.2.2 Synthesis of peptides

The synthesis of peptides (linker-B and linker-C) was performed using an automated solid-phase peptide synthesizer on a Fmoc-Gly-Wang resin. Briefly, 164 mg (0.1 mmol) of the resin was deprotected using 20% piperidine in DMF. Fmoc protected compounds (0.5 mmol) were coupled to the growing peptide of the resin using COMU (0.5 mmol) and DIEA (1 mmol). The synthesized peptide was cleaved from the resin using a cleavage cocktail (TFA/phenol/water/TIS (88/5/5/2)). The cleaved product was precipitated in cold ethyl ether, filtered, and washed three times. The crude peptide was dried, and the desired peptide was purified by RP-HPLC/MS. The synthesis and characterization of Cat S-cleavable peptidic linker (Maleimide-PMGLPG)$_2$K) (CL) was performed according to our previously published report (117).

3.2.3.2.3 Synthesis of TCO

Photochemical synthesis of TCO was carried out according to a previously published method with modifications (86). CCO (500 mg) and methyl benzoate (500 mg) was added to 250 mL solvent (Ether:Hexane = 9:1) in a 500 mL quartz reaction vessel. No attempt to degas the solution was made. The vessel was irradiated with 254 nm light in a UV reactor (CL-1000 Ultraviolet Crosslinker, UVP) under constant stirring. At 30 min intervals, the irradiation was stopped, and the entire solution was passed through a column packed with silver nitrate (10%) impregnated silica. The solution that passes through was then transferred back into the quartz flask and irradiation was continued. After ten rounds, the irradiation was stopped, and the silica was

added to a solution of ammonium hydroxide and stirred for 5 min after which DCM was added and stirring continued for another 5 min. The mixture was filtrated and the organic phase was separated out, washed with brine and purified with chromatography (hexane/ethylacetate = 30:1/10:1) to give 250 mg TCO (50%) as a mixture of isomers, major and minor. No attempt was made to separate the isomers at this step.

3.2.3.2.4 Synthesis of TCO-NO_2

Synthesis of the title compounds was adapted from a previously reported synthesis (201). Briefly, to a stirring solution of TCO (major and minor) (200 mg, 1.59 mmol) in DCM (50 mL) was added pyridine (309 µL, 3.17 mmol). To this mixture, 4-nitrophenylchloroformate (480.8 mg, 2.38 mmol) dissolved in 10 mL DCM was added and was allowed to stir at room temperature for 1 h. The reaction was quenched by the addition of aqueous NH_4Cl and the organic layer was separated. The remaining aqueous layer was extracted twice with DCM and the combined organic layers were dried over $MgSO_4$ and concentrated under vacuum. Purification was performed by using silica gel chromatography (1:200 ethyl acetate/hexane) to afford 301.1 mg of the combined two compounds (1.034 mmol, 65%); TCO-NO_2 major and TCO-NO_2 minor were found to be in 66.2% and 33.8% yield of the total product, respectively.

3.2.3.2.5 Synthesis of TCO-B and TCO-C

Linker-B (16 mg, 0.028 mmol) was dissolved in 300 µL anhydrous DMSO, purged with N_2, and stirred. To this mixture a solution of TCO-NO_2 major (12.24 mg, 0.042 mmol) in 200 µL anhydrous DMSO under N_2 was added dropwise. The reaction tube was capped, and the mixture was stirred for 4 h. To the reaction mixture DI water (3 mL) was added and the resultant suspension was spun down to remove the precipitate. The filtrate was lyophilized to provide the crude product. The product (TCO-B) was purified by RP-HPLC/MS using a 65% to 58% gradient separation to afford 11.4 mg (0.016 mmol, 56%) as a white solid. The solvent system consisted of 0.01% TFA in DI water (solvent A) and 0.01% TFA in ACN (solvent B).

Synthesis of TCO-C was similarly performed using linker-C (16 mg, 0.017 mmol) and TCO-NO_2 major (7.28 mg, 0.025 mmol). The product was purified by RP-HPLC/MS using a 75% to 70% gradient separation, employing the same solvent system as previously described, to afford 10.1 mg (0.009 mmol, 52.9%) of the product as a white solid.

3.2.3.2.6 Synthesis of TCO-B-TFP and TCO-C-TFP

The synthesis of TCO-B-TFP and TCO-C-TFP was accomplished according to previously reported literature procedures with minor modifications (202). Briefly, 7.2 μmol of TCO-B or TCO-C was dissolved in anhydrous DMF (200 μL) and a solution of TFP (3.6 mg, 21.6 μmol) in anhydrous DMF (100 μL) and DIC (3.6 μL, 21.6 μmol) was added and the reaction mixture was allowed to stir for 6 h. The products were precipitated in cold ethyl ether, filtered, washed three times with cold ethyl ether, and dried under vacuum to afford 5.1 mg (5.8 μmol, 80.6%) of TCO-B-TFP and 7.5 mg (5.9 μmol, 82.0%) of TCO-C-TFP as white solids.

3.2.3.3 Synthesis of HPMA copolymers

3.2.3.3.1 Reversible addition-fragmentation chain transfer (RAFT) polymerization reactions

The synthesis of HPMA copolymers employing reversible addition-fragmentation chain transfer (RAFT) polymerization was performed and modified following a previously published paper (203). Three copolymers were synthesized and used as precursors, which included the non-cleavable (NP-18, NP-82) and telechelic-block (BP-20) HPMA copolymers. The general procedure for the synthesis of each copolymer includes dissolving HPMA, APMA, FITC-APMA, and DOTA-t(Bu)-APMA monomers at a molar ratio of 88.5:10.0:0.5:1.0, respectively, in a dioxane/DI water (2:1) solution. The total monomer amount was 0.5 mmol. To this mixture was added AIBN initiator (7.7 μmol for NP-18 and BP-20, and 1.6 μmol for NP-82). A solution consisting of either 8.9 μmol CTA-1 (for NP-18), 8.9 μmol CTA-2 (for BP-20), or 1.4 μmol CTA-1 (for NP-82) was also added to keep the final volume 500 μL. The mixture was transferred into a glass ampule, purged with N_2 for 30 min, flame sealed, and stirred for 48 h at 50 °C. The mixture was cooled to room temperature

and purified by a LH-20 column using methanol as an eluent to afford the desired copolymer as a yellow solid. Measurement of molecular weights were performed by size exclusion chromatography (SEC) using TDA-SEC.

3.2.3.3.2 Synthesis of deprotected block copolymer (d-BP-20)

The synthesis of d-BP-20 was performed over three steps, according to a published report (117). First, to a solution of BP-20 (50 mg) in 1 mL methanol was added 100 µL of hexylamine and the reaction was allowed to stir for 2 h at room temperature. The copolymer was then precipitated in cold ethyl ether to afford a yellow solid. Next, the copolymer was dissolved in 1 mL DI water followed by the addition of excess TCEP (100 times the molar equivalent to the initial amount of BP). The mixture was stirred for 4 h at room temperature. The copolymer was purified by a LH-20 column using methanol as an eluent to afford a yellow solid. Lastly, the copolymer was dissolved in 2 mL of a 95:5 TFA/DCM solution and stirred at room temperature. After 1 h, the solvent was evaporated by a N_2 flow. The copolymer was redissolved in methanol and purified using a LH-20 column to afford d-BP-20 as a yellow solid (41.2 mg, 82.4%).

3.2.3.3.3 Synthesis of multi-block HPMA copolymer (MP-90)

The Cat S-cleavable peptidic linker (CL) (5.1 mg, 3 µmol) was dissolved in methanol (100 µL) and added to a solution of d-BP-20 copolymer (36 mg) in 200 µL PBS (pH = 6.8). The mixture was purged with N_2 for 30 min and stirred for 48 h at 40 °C. The reaction mixture was filtered using a 0.22 mm filter and fractionated using a HPLC equipped with an Asahipak GF-510 HQ column (eluent = 40% ACN in PBS). The desired fraction was desalted (Amicon Ultra-4 centrifugal filter, 30 kDa) using DI water and evaporated under vacuum to afford MP-90 as a yellow solid (5.7 mg, 15.9 %).

3.2.3.4 TCO-polymer conjugations

The polymer-analogous reactions were performed according to the following general procedure. The desired amount (4 mg) of the copolymer was dissolved in anhydrous DMSO

followed by the addition of an anhydrous DMSO solution containing 4 μmol of either TCO-A-NHS, TCO-B-TFP, or TCO-C-TFP to keep the final volume at 300 μL. The reaction mixture was stirred at room temperature for 4 h. The reaction mixture was concentrated under N_2 and then diluted with methanol. The product was purified using a LH-20 column and dried under vacuum to afford a yellow solid.

The unreacted primary amines of APMA within NP-18-TCO-3, NP-18-TCO-3, and MP-90-TCO-3 were capped with excess glycolic acid. Briefly, glycolic acid (1.5 mg, 19.8 μmol), EDC (3.75 mg, 19.8 μmol), and NHS (2.52 mg, 21.8 μmol) were dissolved in DMSO (50 μL). The reaction mixture was stirred at room temperature for 4 h. To this mixture was added a solution containing DIEA (25 μmol) and the desired TCO-HPMA copolymer (3 mg, a portion of each TCO-copolymer was kept uncapped) in 100 μL DMSO. After 4 h, the reaction mixture was diluted with DI water, and the TCO-HPMA copolymer was purified using an Amicon Ultra-4 centrifugal filter (3 kDa). Quantification of the primary amine content after capping was evaluated using a Ninhydrin assay according to our previously reported literature procedure (204). Unless otherwise indicated, the uncapped portion of each of the TCO-HPMA copolymers was used for characterization (^{19}F-NMR, ^{1}H-NMR, and molecular weight estimations) and kinetic studies. The capped portion was used for *in vitro* Cat S cleavage and *in vivo* studies.

3.2.3.5 Synthesis of dextran polymer-tetrazine (DP-TZ)

The synthesis of dextran polymer-TZ (DP-TZ) was performed following a modified literature procedure (89). Briefly, 8 mg (4 nmol) of dextran polymer-NH_2 (DP) was dissolved in 800 μL PBS (pH = 7.4) followed by the addition of 40 μL Na_2CO_3 (0.1 M). To this mixture a DMF solution (20 μL) containing tetrazine-NHS (5.3 mg, 16.8 μmol) was slowly added. The reaction mixture was incubated at room temperature with agitation (700 rpm) for 2 h. DI water (3 mL) was added and the reaction mixture was spun down by centrifugation (15 s at 1000 g) to remove the precipitates. The product (supernatant) was purified using an Amicon Ultra-4 centrifugal filter (100

kDa) and afforded a pink solid. The content of TZ was characterized using UV/Vis spectroscopy, based on a standard curve prepared for the absorbance of the tetrazine-NHS-ester (27 – 217 μM) (solvent = 50% methanol in DI water) at 269 nm.

3.2.4 Radiolabeling of DOTA-TZ probes and TCO-HPMA copolymers

The DOTA-TZ probes were radiolabeled by dissolving 25 μg of the desired probe in an ammonium acetate buffer (0.5 M, 100 μL, pH = 5.5) and adding 3.7 MBq (100 μCi) of $^{177}LuCl_3$ to the solution. The mixture was heated for 65 °C. After 30 mins, 4-6 mg of $CoCl_2$ was added, and the mixture continued stirring at 65 °C for an additional 5 min. The radiolabeled DOTA-TZ probe was purified using a radio-HPLC with solvent gradient methods similar to the procedure used in the synthesis of the DOTA-TZ probes. The radiolabeled DOTA-TZ probes were concentrated using N_2 flow before any further studies. The ^{nat}Lu-DOTA-TZ probes were similarly prepared using $^{nat}LuCl_3$ and purified by RP-HPLC/LC.

Radiolabeling of TCO-HPMA copolymers were performed by dissolving 100 μg of the desired compound in 100 μL DI water and followed by the addition of 3.7 MBq (100 μCi) of $^{177}LuCl_3$ or $^{111}InCl_3$. The mixture was heated at 65 °C for 30 min. A radio-SEC-HPLC, equipped with an Asahipak GF-510 HQ column, Bioscan flow count radiometric detector, and a Waters 2489 UV detector (λ = 494 nm), was used to identify and purify the radiolabeled copolymers. The purified radiolabeled copolymers were buffer exchanged in PBS and concentrated using an Amicon Ultra-4 centrifugal filter (3 kDa) before continuing on to any further studies.

3.2.5 Kinetic studies

Kinetic studies were performed between the DOTA-TZ-probes and either the TCO-linkers (TCO-B and TCO-C) or the desired TCO-HPMA copolymers in pseudo-first order conditions (92). The reaction between a DOTA-TZ probe (DOTA-TZ-1 or DOTA-TZ-2) and a TCO-linker was monitored using radio-HPLC. Briefly, a ^{177}Lu-DOTA-TZ probe in PBS was

mixed with a known amount of ^{nat}Lu-DOTA-TZ probe (to make 0.5 μM) in PBS and incubated at 37 °C. To this mixture was added a solution of a TCO-molecule (2 or 4 μM) in PBS to keep a final volume of 800 μL and a radioactivity concentration of 0.74 MBq (20 μCi) per 50 μL. At the desired time point, 50 μL of the reaction mixture was pipetted out and quenched immediately with the corresponding DOTA-TZ-NHS ester (100 folds greater than the DOTA-TZ probe concentration) dissolved in 50 μL ACN. At the end of the last time point, each fraction was injected into the radio-HPLC (85% to 65% gradient separation over 15-min run using 0.1% formic acid in DI water and 0.1% formic acid in ACN for solvents A and B, respectively) to obtain the corresponding radio-chromatogram. The integrations of formed radioactive peaks (products) were divided by the total value for the integrations of starting and formed radioactive peaks to obtain the reaction yield (%).

Additional kinetic studies with the DOTA-TZ probes (DOTA-TZ 1 or DOTA-TZ 2) reacted with the desired TCO-HPMA copolymers were performed. Briefly, the ^{177}Lu-DOTA-TZ probe in PBS was mixed with a known amount of ^{nat}Lu-DOTA-TZ probe in PBS (to make 0.5 μM) and incubated at 37 °C. To this mixture was added a solution of the desired TCO-HPMA copolymer in PBS to achieve a final volume of 800 μL with a radioactivity concentration of 100,000 cpm/50 μL. At each time point, a 50 μL aliquot of the reaction mixture was removed and immediately quenched with an excess (100 X) amount of the corresponding DOTA-TZ-NHS ester dissolved in 50 μL ACN. The copolymer was then purified using an Amicon Ultra-4 centrifugal filter (3 kDa). The radioactivity bound to the copolymer was measured using a gamma counter. All kinetic studies were performed in duplicates.

The pseudo first-order rate constant (k_{obs}) was estimated for each IEDDA reaction between the DOTA-TZ probe and TCO by fitting the reaction yields with time to the one-phase association model using Graphpad PRISM 7 (U.S.). The second order rate constant (K_2) was calculated by dividing the K_{obs} over the TCO concentration (87).

3.2.6 *In vitro* cleavage of multi-block HPMA copolymer

The *in vitro* cleavage studies using the Cat S enzyme was conducted for the desired HPMA copolymer according to our previously published paper (120). Briefly, the desired copolymer was added to 250 µL of the cleavage buffer containing sodium acetate (50 mM), DTT (10 mM), and EDTA (1 mM) to keep a concentration of 1 mg/mL. To this solution was added human cath S enzyme (2.50 µg/mL) and incubated at 37 °C. At the desired time point, a 50 µL aliquot of the mixture was pipetted out and mixed with 50 µL of SEC eluent (40% ACN in PBS). The 100 µL of sample was injected into a SEC-HPLC (equipped with an Asahipak GF-510 HQ column and Waters 2489 UV detector (λ = 494 nm)) to identify the intact and cleaved copolymers.

3.2.7 Cell culture

Ovarian cancer (OVCAR-3) cells were obtained from American Type Culture Collection (ATCC). The cells were cultured in our laboratory, as per ATCC protocol, in RPMI-1640 medium containing 20% FBS, 2 mM L-glutamine, 10 mM HEPES, 1 mM sodium pyruvate, and 0.01 mg/ml bovine insulin. Cells were incubated at 37 ˚C at 5% CO_2.

3.2.8 Biodistribution and *in vivo* DOTA-TZ-TCO reactivity (single- and dual-radioisotope experiments)

3.2.8.1 Biodistribution in a CF-1 mouse model (single-radioisotope experiment)

The biodistribution of the desired copolymer was investigated in CF-1 mice (Charles River, U.S.) weighing ~ 27 g. The mice (5 mice per group) were injected with the desired ^{177}Lu-TCO-HPMA copolymer (10 µCi, 0.37 MBq) in 100 µL PBS. The mice were sacrificed after 72 h. Their tissues were excised and weighed.

3.2.8.2 Biodistribution and *in vivo* DOTA-TZ-TCO reactivity in ovarian-cancer models (dual-radioisotope experiments)

Four-week old female NOD-SCID mice (Jackson Laboratory, U.S.) were injected subcutaneously with 100 µL OVCAR-3 cells (5×10^6) suspended in Matrigel® into the flanks. Tumor growth was regularly monitored until it reached ~ 50 mm^3. The mice (weighing ~ 18 g) were then randomly allocated into three groups (5 mice per group). The groups were intravenously injected with 100 µL PBS containing the desired non-radiolabeled TCO-HPMA copolymers (TCO content ~ 23 nmol) premixed with the corresponding ^{111}In-radiolabeled copolymer (0.37 MBq, 10 µCi). After three days, all the mice were injected with 100 µL PBS containing 0.37 MBq (10 µCi) of ^{177}Lu-DOTA-TZ-2. After 4 h, the mice were sacrificed, and their tissues were excised and weighed. A similar study was also conducted in ovarian tumor bearing-NOD-SCID mice to evaluate the biodistribution of ^{177}Lu-DOTA-TZ-2 (after 4 h of injection) in one group using a single-radioisotope experiment. Additionally, the biodistribution and *in vivo* TCO/TZ reactivity of uncapped NP-82-TCO-C was performed in another group using a dual-radioisotope experiment.

Another ovarian cancer model was similarly developed in female SCID mice (Charles River, U.S.). The mice were (weighing ~ 18 g) then separated into three groups (5 mice per group) and injected with the desired amount of non-radiolabeled TCO-HPMA copolymer (TCO content = 23 nmol) premixed with the corresponding ^{111}In-radiolabeled copolymer (0.37 MBq, 10 µCi). After three days, the mice from one group were injected with 100 µL PBS containing DP-TZ (TZ content = 60 nmol). The other two groups were injected with 100 µL PBS (no DP-TZ). After 30 mins, all mice were injected intravenously with 100 µL PBS containing 0.37 MBq (10 µCi) of ^{177}Lu-DOTA-TZ-2. The mice were sacrificed after 4 h later, and their tissues were excised and weighed.

All the injections performed with mice were via tail veins. The tissue radioactivity in all the included mice was measured using a gamma counter. The signal of each radioisotope was

identified based on the corresponding energy level. Data are expressed in terms of %ID/g of tissue per each radioisotope.

3.2.9 Statistics

Statistical analyses were performed using a two-tailed unpaired Student's t-test (two groups) or one-way ANOVA (more than two groups) with Bonferroni post-tests. A value of $p < 0.05$ was considered statistically significant.

3.3 Results and discussion

The off-target retention of radiolabeled nanomedicines (e.g., HPMA copolymers) developed for cancer imaging and therapy is a major obstacle. Our previous reports showed that the large (≥ 80 kDa) multi-block radiolabeled HPMA copolymers synthesized by linking multiple polymeric chains using a Cat S-cleavable linker (CL) are cleared from the off-target tissues (e.g., liver, spleen, blood) at a faster rate relative to HPMA copolymers of the same size with no CL. We aimed to combine this approach with the pretargeted approach (TCO/TZ bioorthogonal chemistry) to improve radiolabeled HPMA copolymer's toxicity profiles further. We first optimized the TCO/TZ reaction by modulating the TCO-linker (used for linking TCO with the HPMA copolymer) and the TZ type (tetrazine versus methyltetrzaine) by conducting kinetic studies. The optimized TCO-linker was used to synthesize a cathepsin S cleavable TCO-HPMA copolymer (> 100 kDa). We investigated its biodistribution and *in vivo* TCO/TZ chemistry profiles in a normal and two ovarian-cancer mice models.

3.3.1 Synthesis and characterization of TCO-linkers

As will be discussed later, TCO was incorporated into the copolymer post-polymerization. Three TCO-linkers (TCO-A, TCO-B and TCO-C) of varying length were synthesized to examine the impact linker length had in the IEDDA reaction kinetics (Figure 3.1). TCO-A (TCO-PEG_4-NHS) was purchased from commercial source while the amine-reactive TCO-B (TCO-PEG_4-

(D)Asp(NH-F_3)-Gly-Gly-TFP) and the amine-reactive TCO-C (TCO-PEG_4-(D)Gln-(D)Gln-(D)Gln-(D)Asp(NH-F_3)-Gly-Gly-TFP) were synthesized in our laboratory. The synthesis of the TCO-B and TCO-C is described below.

TCO was synthesized by photoisomerization of the cis-cyclooctene (CCO) to yield two stereoisomers designated as the major (equatorial hydroxy) and minor (axial hydroxy) TCO product (Figure 3.1). The isomeric mixture was reacted with 4-nitrophenylchloroformate to give the carbonate intermediates named TCO-NO_2 major and TCO-NO_2 minor which were subsequently separated and purified by silica gel chromatography. In this proof of concept study, only the TCO major was used due to the significantly larger yield relative to TCO minor. Future studies may be needed to determine the reaction kineteics using TCO major versus TCO minor. Linkers B (PEG_4-(D)Asp(NH-F_3)-Gly-Gly) and C (PEG_4-(D)Gln-(D)Gln-(D)Gln-(D)Asp(NH-F_3)-Gly-Gly) were synthesized by SPPS and purified by RP-HPLC. The amino acid derivative (D)Asp(NH-F_3) was prepared by reaction of Fmoc-(D)Asp-(OtBu) with 2,2,2-trifluoroethylamine hydrochloride followed by deprotection and purification. The (D)Asp(NH-F_3) was incorporated into the TCO-linkers to allow for quantification of the TCO-linker incorporation into the polymeric constructs using ^{19}F-NMR. The deprotected peptides were subsequently reacted with the major TCO-NO_2 isomer to achieve the desired peptides, TCO-B and TCO-C. The TFP functionalized active esters of these peptides, TCO-B-FTP and TCO-C-FTP, were prepared using the DIC coupling agent. The ^{1}H-NMR, ^{13}C-NMR and mass spectrums for the intermediates and final products for TCO-B-TFP and TCO-C-TFP are shown in Figure 3.2-3.5.

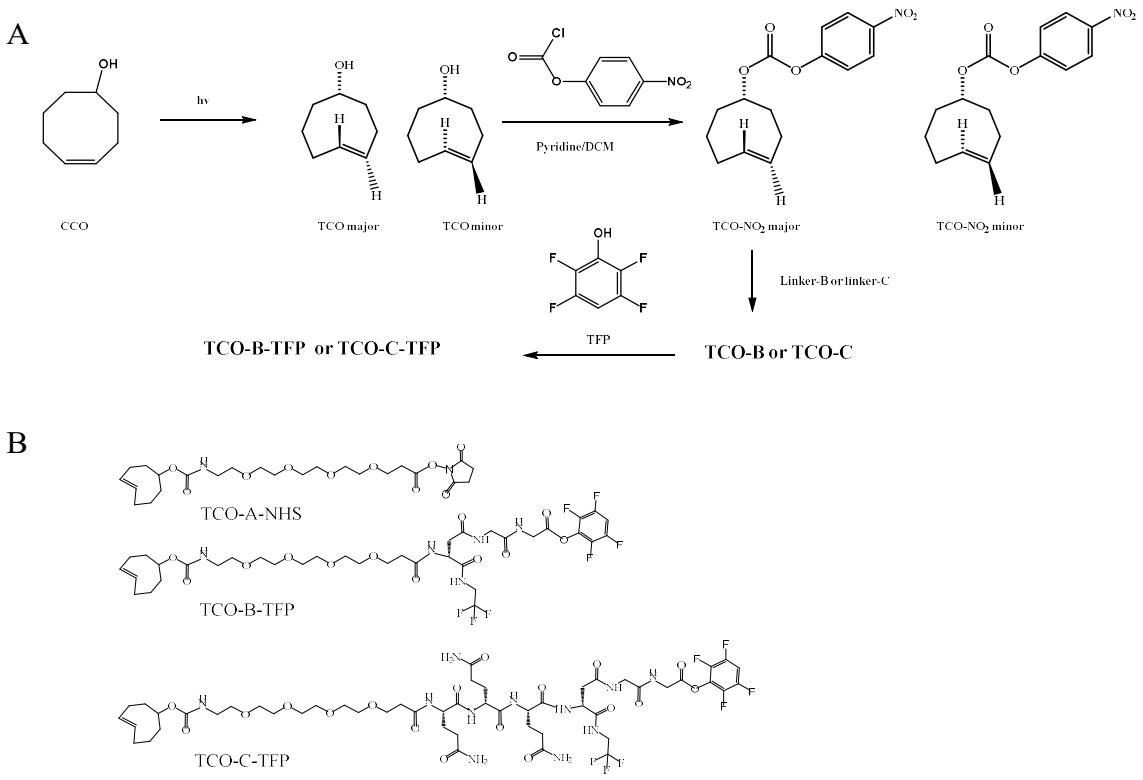

Figure 3.1 Synthesis and structures of TCO-linkers. Synthesis of TCO-B-TFP and TCO-C-TFP is shown in (A). The structures of the commercially purchased (TCO-A-NHS) and the synthesized TCO-B-TFP and TCO-C-TFPA is shown in (B).

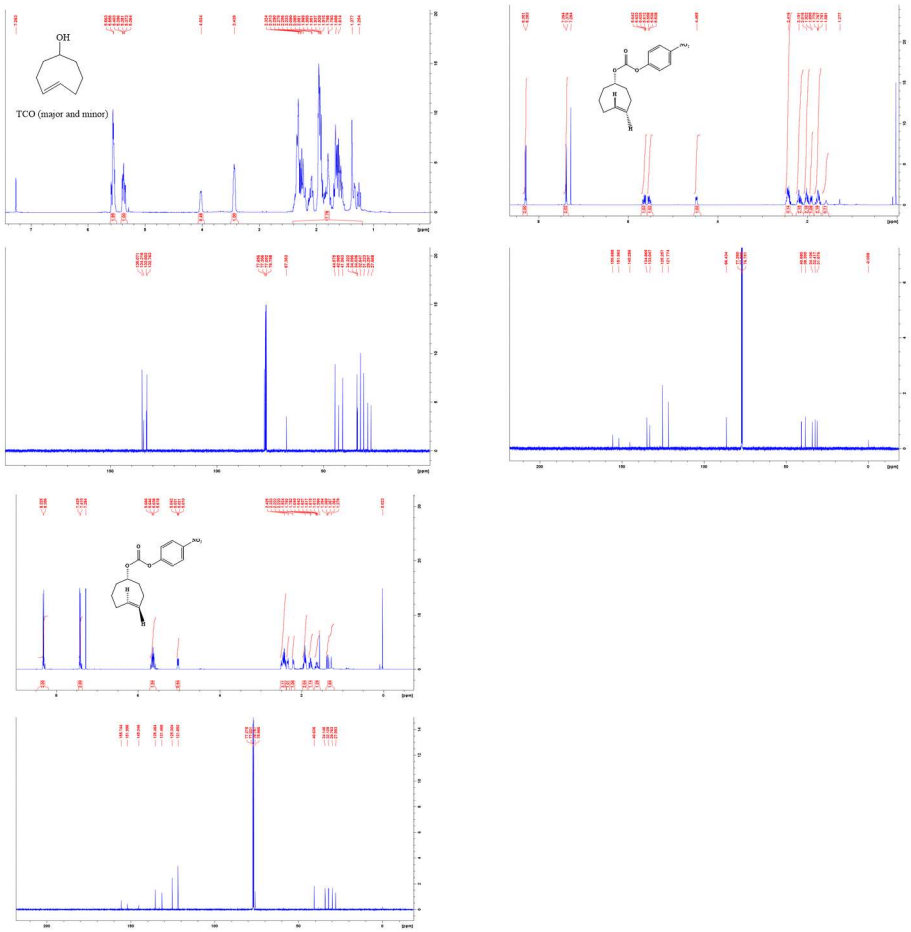

Figure 3.2 ^{1}H-NMR and ^{13}C-NMR spectra of CCO (A), TCO major (B), and TCO minor (C).

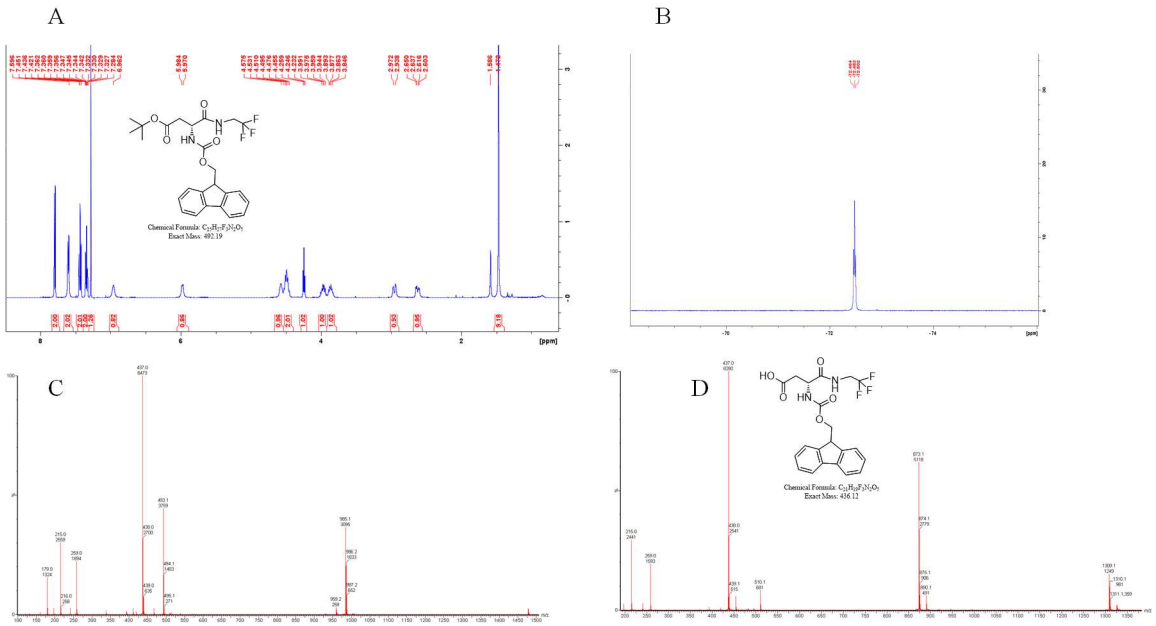

Figure 3.3 ^{1}H-NMR (A), ^{19}F-NMR (B), and MS (C) spectra of Fmoc-D-Asp(OtBu)-NH-F_3 and MS spectrum of Fmoc-D-Asp(OH)-NH-F_3 (D).

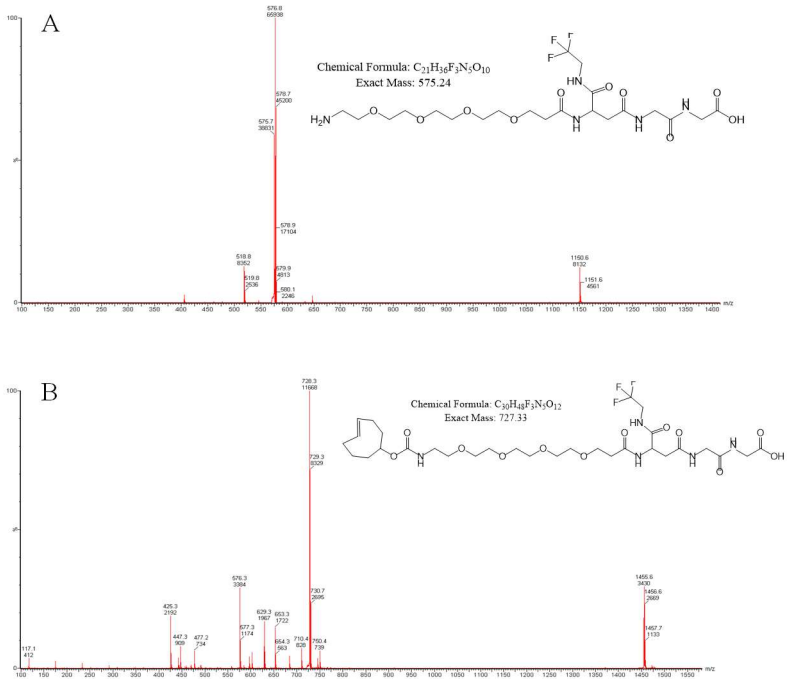

Figure 3.4 MS spectra of linker-B (A) and TCO-B (B).

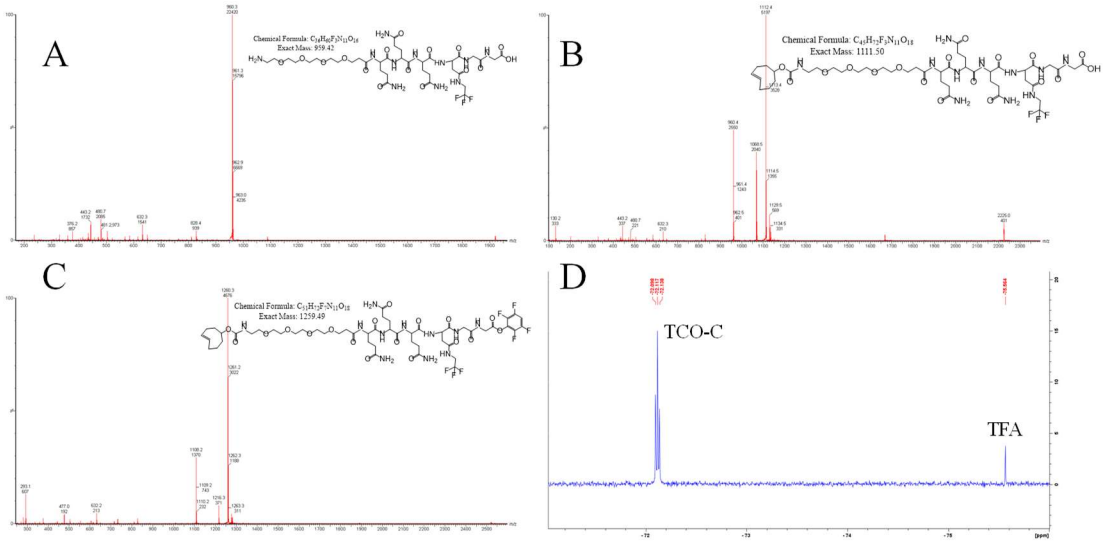

Figure 3.5 MS spectra of linker-C (A), TCO-C (B), and TCO-C-TFP (C) and ^{19}F-NMR spectrum of TCO-C (D).

3.3.2 Synthesis and characterization of the DOTA-TZ "chaser" agents

The synthesis of the DOTA-TZ probes were carried out in a five-step synthetic process outlined in Figure 3.6. Starting from Fmoc-PEG_2-COOH, N-Boc-ethylenediamine (EDA) was coupled to the C-terminus using DIC/NHS/DIEA. The Fmoc-PEG_2-EDA-N-Boc was treated with piperidine to yield the Fmoc-deprotected primary amine which was subsequently reacted with DOTA-NHS to yield DOTA-PEG_2-EDA-N-Boc. The N-Boc was removed by treatments with TFA followed by reaction of the resulting primary amine with the methyltetrazine-NHS ester or tetrazine-NHS ester to give DOTA-TZ 1 or DOTA-TZ 2, respectively. Tetrazine has been reported to have faster reaction kinetics relative to methyltetrazine, but methyltetrazine has a higher stability under physiologic conditions (194, 205, 206). These two tetrazine analogs where chosen to compare and contrast how these factors affect *in vitro* and *in vivo* performance. The ^{1}H-NMR, ^{13}C-NMR and mass spectrums for the intermediates and DOTA-TZ 1 or DOTA-TZ 2 are shown in Figure 3.7-3.9.

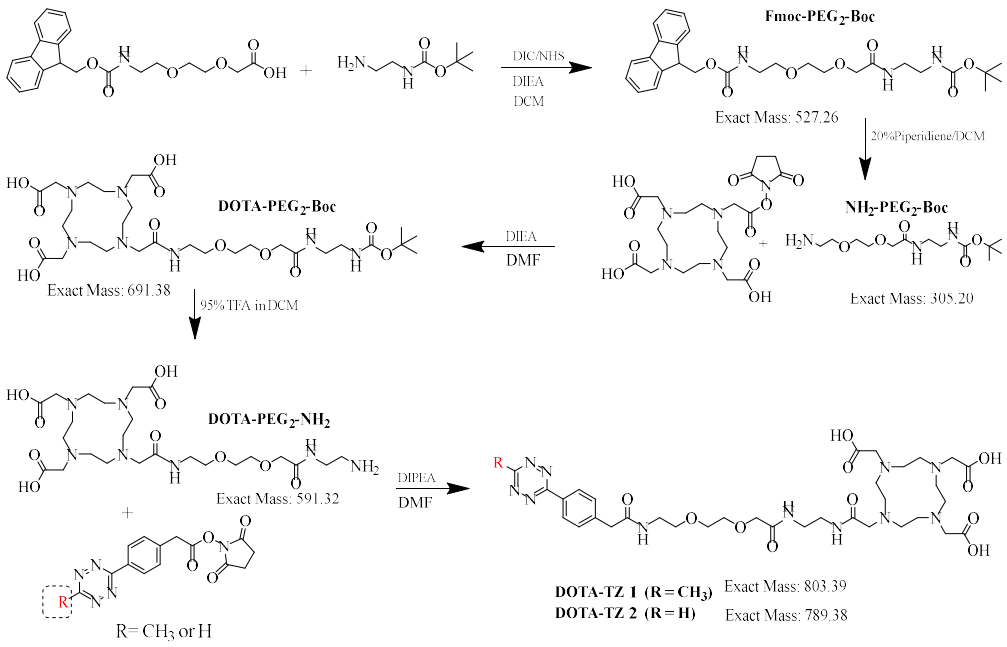

Figure 3.6 Synthesis of DTOA-TZ probes

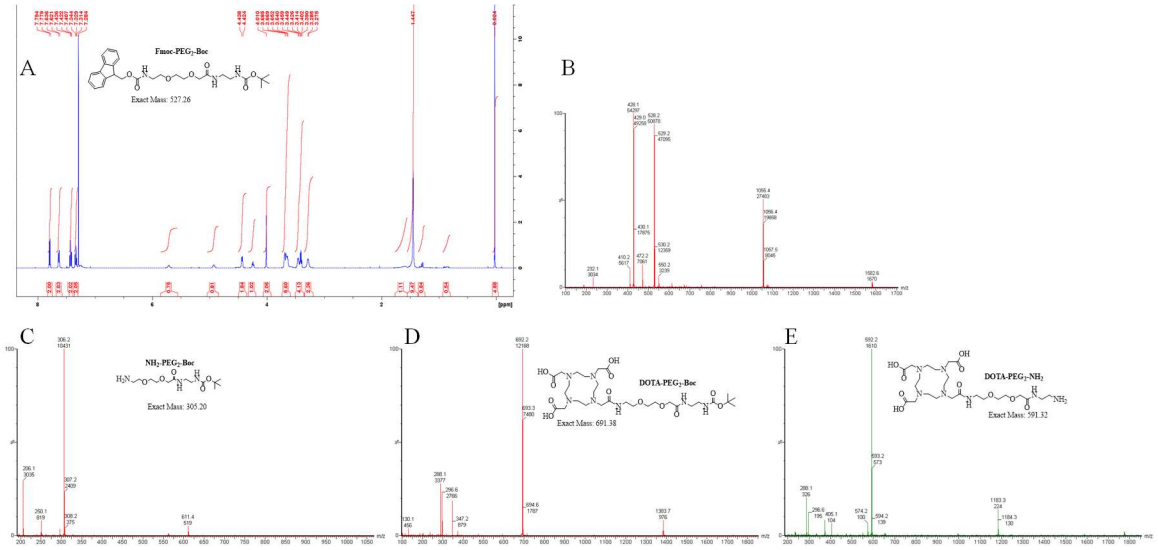

Figure 3.7 Profiles of intermediates for the synthesis of DOTA-TZ probes.

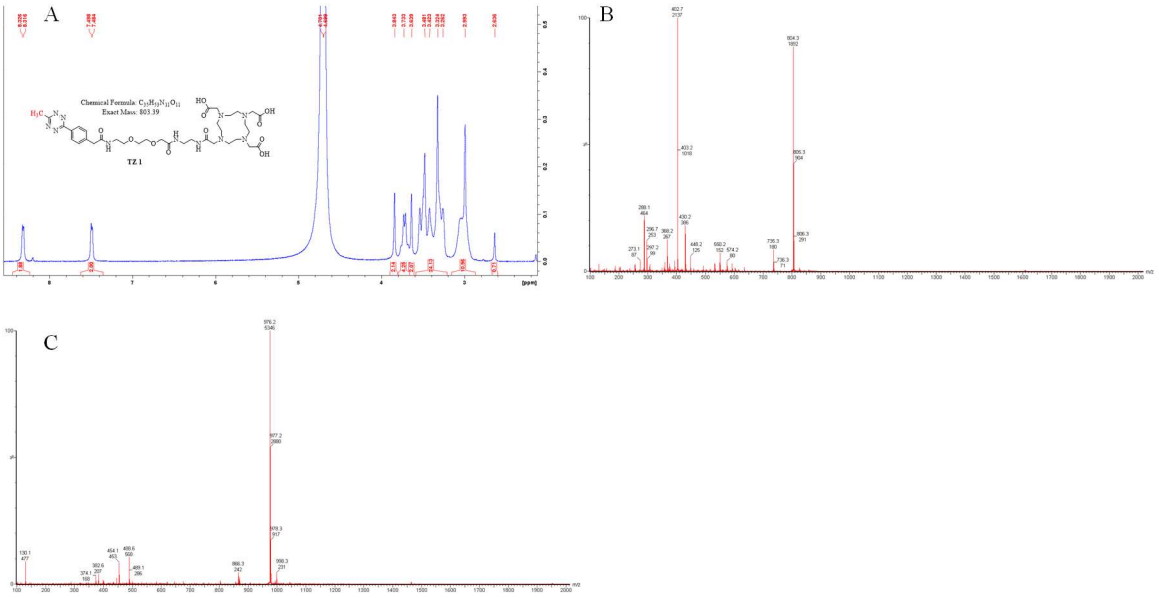

Figure 3.8 ^{1}H-NMR (A) and MS (B) spectra of DOTA-TZ 1 and MS spectrum of ^{nat}Lu-TZ 1.

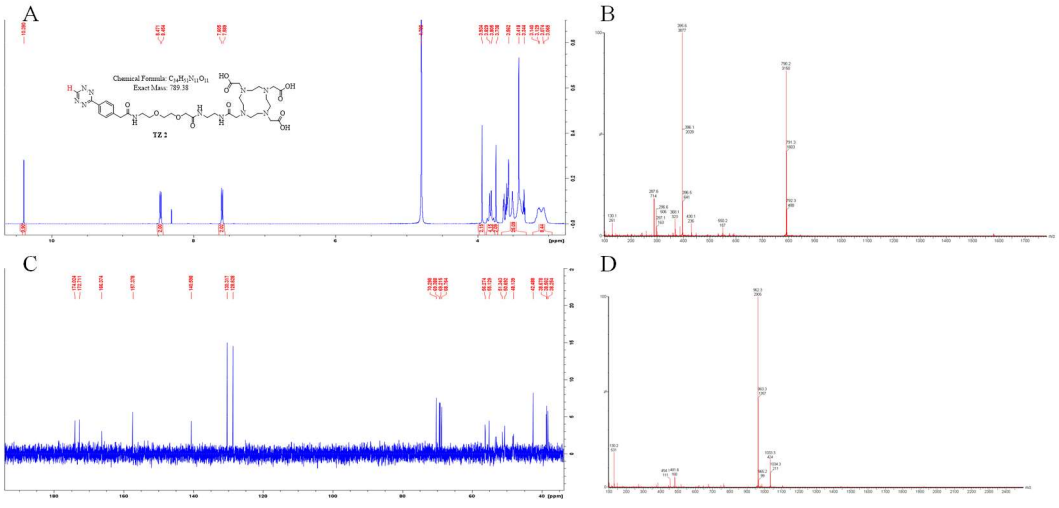

Figure 3.9 ^{1}H-NMR (A), MS (B), ^{13}C-NMR (C) spectra of DOTA-TZ 2 and MS spectrum of ^{nat}Lu-DOTA-TZ 2.

3.3.3 Synthesis and characterization of non-cleavable of TCO-incorporated HPMA copolymers

To examine the impact polymer molecular weight has on IEDDA conjugation efficacy, a small (NP-18) and large (NP-82) non-cleavable HPMA copolymer were prepared by RAFT polymerization (Figure 3.10). Each polymerization included HPMA, APMA, DOTA-t(Bu)$_3$-APMA, and FITC-APMA monomers at a 88.5:10:1:0.5 molar ratio. The APMA is included in the copolymer for eventual post-polymerization TCO incorporation. DOTA-t(Bu)$_3$-APMA and FITC-APMA monomers are added to the copolymer for radiolabeling and to assist in visualization/detection of the HPMA copolymer during purification and characterization, respectively. The polymerization reaction was initiated using AIBN and carried out in the presence of the commercially available chain transfer agent CTA-1. The ratio of AIBN and CTA-1 relative to total monomer concentrations were adjusted to synthesize the desired small and large HPMA copolymers. The resulting copolymers were deprotected with TFA, purified and characterized to yield molecular weights of 18.3 and 82.1 kDa, correspondingly, for NP-18 and NP-82. The characteristics of the copolymers including molecular weight, dispersity, yield and monomeric content is outlined in Table 3.1.

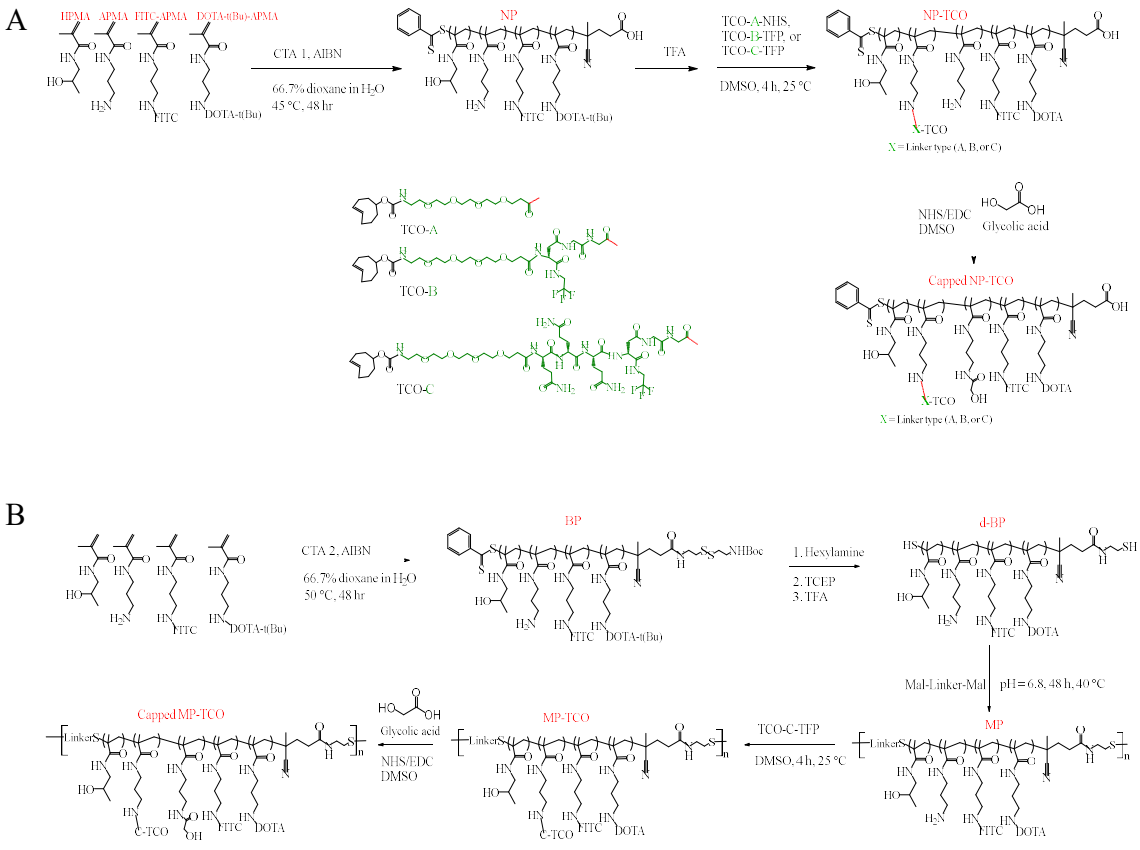

Figure 3.10 Schematic representations for the synthesis of non-cleavable (A) and cleavable (B) TCO-HPMA copolymers. Capping was only performed for selected TCO-HPMA copolymers (NP-18-TCO-C, NP-82-TCO-C, and MP-90-TCO-C).

Table 3.1 Characteristics of TCO-HPMA copolymers and their polymeric precursors

copolymers	MW[d] (kDa)	Đ[d]	APMA[e] (mol.%)	DOTA[e] (mol.%)	FITC[f] (mol.%)	RAFT polymerization yield (%)	TCO content (μmol / mg)[h] / average number of TCO per copolymer chain
NP-18[a]	18.3	1.07	9.2	0.53	0.32	76.8	0
NP-82[b]	82.1	1.08	9.1	0.48	0.20	82.1	0
BP-20[c]	20.2	1.10	8.5	0.62	0.29	79.0	0
MP-90	89.8	1.17					0
NP-18-TCO-C	22.7	1.10					0.262 / 6.4
NP-82-TCO-A	93.7	1.12					0.382[e] / 35.8
NP-82-TCO-B	100.5	1.10					0.257 / 25.8
NP-82-TCO-C	101.3	1.11					0.231 / 24.6
MP-90-TCO-C	108.7	1.20					0.208 / 23.6

[a]Intermediate copolymer for the synthesis of NP-18-TCO-C
[b]Intermediate copolymer for the synthesis of NP-82-TCO-A, NP-82-TCO-B, and NP-82-TCO-C
[c]Intermediate copolymer for the synthesis of MP-90, which was used for the synthesis of MP-90-TCO-C
[d]Estimated by gel permeation chromatography
[e]Determined by ^{1}H-NMR
[h]Determined by ^{19}F-NMR
[f]Determined by UV/Vis spectrophotometry

To examine the impact of linker length on the IEDDA kinetics, the previously described TCO-linkers (TCO-A-NHS, TCO-B-TFP, and TCO-C-TFP) were conjugated to the primary amines of the APMA contained within NP-82. This yielded the corresponding TCO-incorporated copolymers, NP-82-TCO-A, NP-82-TCO-B and NP-82-TCO-C. For examining the impact of copolymer molecular weight on the IEDDA reaction, TCO-C-TFP was similarly coupled to NP-18 under identical conditions to give the NP-18-TCO-C. The TCO content on the copolymers was characterized by ^{1}H- or ^{19}F-NMR, exemplar NMR spectrums are given in Figure 3.11. The characteristics of the TCO-incorporated copolymers including molecular weight, dispersity and TCO content is outlined in Table 3.1. For the larger copolymers, the estimated number of TCO units per polymer was in the range of 23.6 – 35.8 TCO units per polymer chain with molecular weights ranging from 93.7 to 108.7 kDa. NP-18-TCO-C exhibited a molecular weight of 22.7 kDa and contained an average of 6.4 TCO moieties per polymer chain.

Excessive positive charge has been shown to lower the circulation time and increase the MPS-associated sequestration of HPMA copolymers (110, 111, 203). Prior to all *in vitro* Cat S cleavage and *in vivo* experiments, the remaining primary amines of the APMA moieties (i.e., not coupled to TCO-linkers) were neutralized (i.e., capped) by reacting with glycolic acid that was activated by EDC/NHS. The capping yields were high (> 85%) for all of the TCO-incorporated copolymers, as estimated by ninhydrin assay.

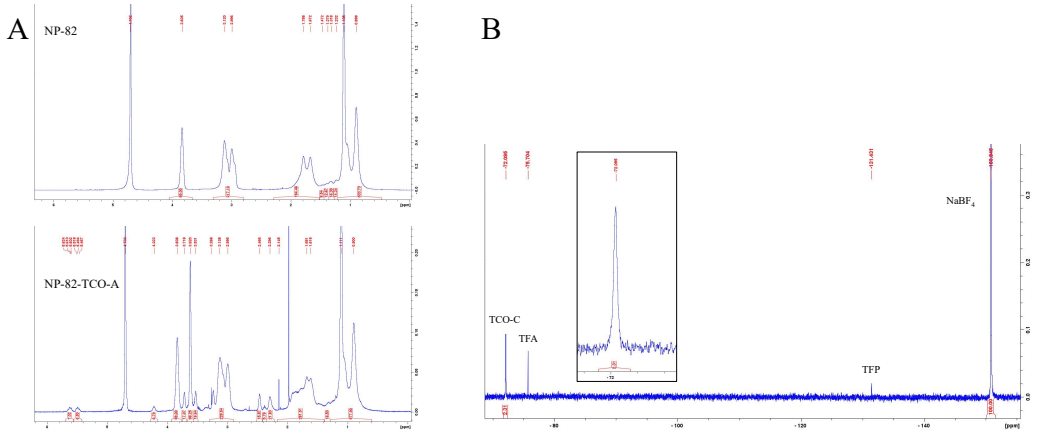

Figure 3.11 ^{1}H-NMR spectra of NP-82 (A top) and NP-TCO-A (A bottom), and ^{19}F-NMR of NP-TCO-C (B).

3.3.4 Synthesis and characterization of Cat S-degradable, TCO-incorporated HPMA copolymers

The synthesis of the Cat S-degradable, TCO-incorporated HPMA copolymer is largely analogous to our original report (117). To synthesis the desired Cat S-degradable HPMA copolymer, a chain transfer agent CTA-2 was synthesized that gives protected thiol on both terminal ends (Figure 3.12A). Using CTA-2, a small HPMA copolymer was made by RAFT polymerization, similar to procedures outlined above, to yield a 20.2 kDa telechelic-block copolymer (BP-20) with protected thiols at the terminal ends (Figure 3.10B). The thiols groups of the BP-20 copolymer were deprotected using hexylamine and TCEP. This was followed by treatment with TFA to remove the t-Bu groups from the incorporated DOTA chelators to give the deprotected BP-20 (d-BP-20). A maleimide-containing Cat S susceptible linker (CL – (Maleimide-PMGLPG)$_2$K) was prepared according to our previous report (Figure 3.12B) (117). Using thiol-ene click chemistry, the combination of the thiol containing d-BP-20 and the maleimide functionalized CL resulted in a condensation reaction to form an extended multi-block copolymer. This multi-block copolymer was fractionated by SEC (Figure 3.13A) to obtain predominantly trimers and higher-order multimers with a molecular weight of 89.8 kDa (Đ = 1.17). Parallel to the procedure outlined above, TCO-C-TFP was incorporated into MP-90 post-polymerization to yield MP-90-TCO-C with a molecular weight of 108.7 kDa and a TCO-incorporation density of 23.6 units per polymer chain. The characteristics of the Cat S-degradable, TCO-incorporated HPMA copolymer including molecular weight, dispersity and TCO content is outlined in Table 3.1. Similar to the above, glycolic acid capping of the primary amines of MP-90-TCO-C was performing prior to *in vitro* Cat S cleavage and *in vivo* biodistribution studies.

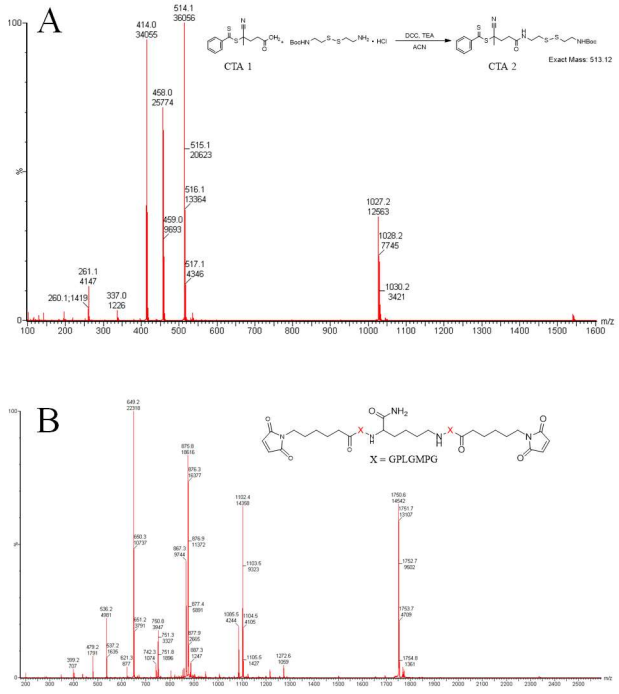

Figure 3.12 Synthesis and MS spectrum of CTA 2 (A) and MS spectrum of Cat S cleavable peptidic linker (CL) (B).

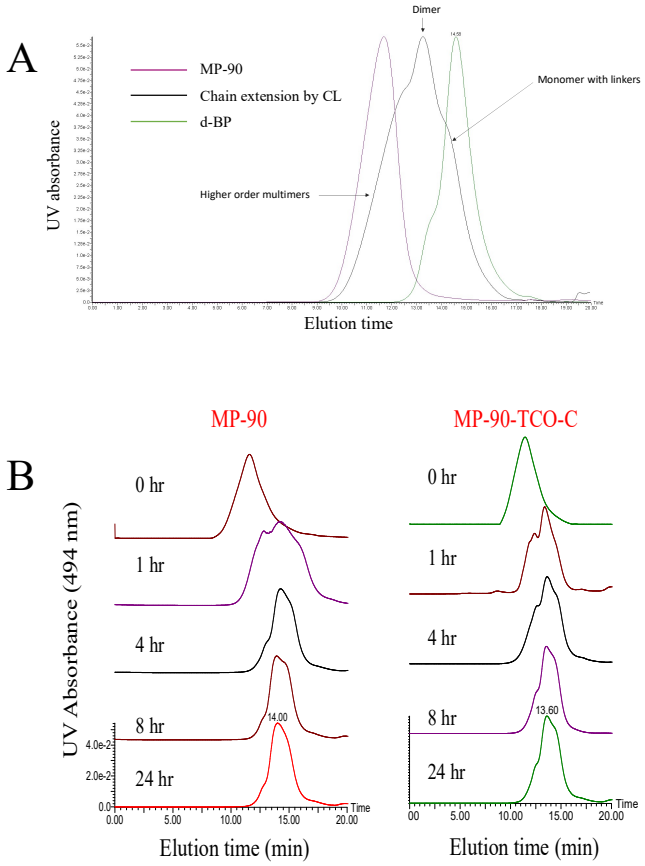

Figure 3.13 SEC-HPLC chromatograms of MP-90 and MP-90-TCO. Chromatograms of d-BP before and after extension with CL (A). Chromatograms of MP-90 and MP-90-TCO-C after incubation with Cat S enzyme (over 24 h) (B). The X-axis represents the absorbance at 494 nm, and Y-axis represents the elution time in min.

3.3.5 Synthesis and characterization of dextran polymer blood masking agent

Excessive amounts of TCO-incorporated copolymer could sequester the tetrazine chaser agent prior to the chaser agent reaching the tumor. It has been demonstrated that the administration of nanomedicine constructs functionalized with tetrazine can mask/inactive TCO in circulation prior to introduction of the chaser agent thereby substantially reducing blood associated retention. As part of our investigation, a dextran polymer (DP) functionalized with tetrazine was prepared (Figure 3.14), as previously described (89), and used as a masking agent in our *in vivo* biodistribution studies. The starting DP molecular weight was approximately 2000 kDa and after functionalization contained 644 tetrazine units per DP.

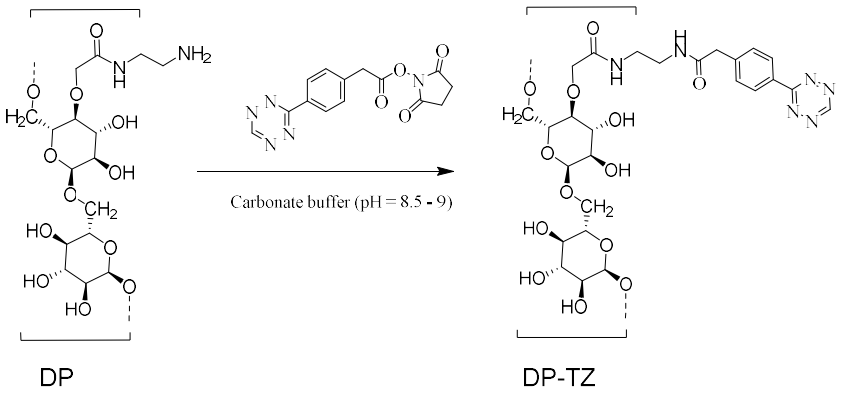

Figure 3.14 Synthesis of DP-TZ.

3.3.6 Radiolabeling of DOTA-TZ probes and TCO-HPMA copolymers

The radiolabeling of DOTA-TZ probes was accomplished by incubation with $^{177}LuCl_3$ in an ammonium acetate buffer (pH = 5.5) at 65 °C for 30 min. The yields of radiolabeling were very high (> 90%) for both probes. The radiolabeling of TCO-HPMA copolymers was also performed using similar conditions with the exception of using DI water instead of ammonium acetate buffer. Depending on the desired experiment, $^{177}LuCl_3$ or $^{111}InCl_3$ was used for the radiolabeling of TCO-HPMA copolymers. The radiolabeling yields for those copolymers were low to moderate (≈ 20 – 40%).

3.3.7 *In vitro* cleavage of multi-block HPMA copolymers (MP-90 and MP-90-TCO-C)

To examine the impact TCO incorporation has on the rate of multi-block copolymers degradation by CatS, MP-90 and capped MP-90-TCO-C were incubated over a 24 h period with Cat S at 37 °C. At specified intervals an aliquot from each mixture was analyzed by SEC to examine the rate of Cat S degradation (Figure 3.13B). The degradation profiles showed a slightly slower cleavage rate over the initial 4 h for the TCO-incorporated copolymer versus vs the unmodified copolymer. Nevertheless, complete Cat S-cleavage is achieved for both polymers by 8 h of incubation. These results indicate that the capped MP-90-TCO-C is indeed susceptible to cleavage by the Cat S protease.

3.3.8 Kinetics studies

Kinetic studies were performed using the unincorporated TCO-B and TCO-C linkers in order to demonstrate their ability to undergo rapid IEDDA reactions as well as to eventually compare the small molecule (i.e., TCO-linker not incorporated into copolymer) vs. the macromolecule (TCO-linker incorporated into copolymer) reaction kinetics Table 3.2. Due to TCO-A being a commercially validated linker, the kinetics of this unincorporated linker were not explored. Using the ^{177}Lu-DOTA-TZ 1, the chaser agent (0.5 μM) was incubated with the TCO-linkers (4 μM) in PBS at 37 °C. Analysis of the reaction was performed by taking aliquots of the solution, quenching the unreacted TCO using excess of an unlabeled TZ and analyzed by radio-RP-HPLC (Figure 3.15**Error! Reference source not found.**). For both the TCO-B and TCO-C linkers, the reaction conditions resulted in more than 95% of the ^{177}Lu-DOTA-TZ-1 reacting within 30 min and K_2 rate constants of 373 ± 54 and 333 ± 12 M^{-1} S^{-1} ($p > 0.05$), respectively. The tetrazine moiety utilized in ^{177}Lu-DOTA-TZ 2 is known to exhibit higher rate constants compared to ^{177}Lu-DOTA-TZ 1 (205). Using ^{177}Lu-DOTA-TZ 2 (0.5 μM), the IEDDA reaction yield with the TCO-C linker (2 μM) was already more than 95% complete after only 3 min with a K_2 rate constant of 9745 ± 742 M^{-1} S^{-1}. It is worth noting that multiple peaks are observed as reaction products in the chromatograms for the radio-HPLC analyses (Figure 3.15). RP-HPLC/MS analysis was performed to confirm these peaks, dihydropyridazine isomers (15.8 and 17.0 min) and a pyridazine rearrangement product (10.0 min), are the result of the IEDDA reaction (Figure 3.16) (207).

Next, the IEEDA reaction kinetics of the non-capped TCO-incorporated HPMA copolymers were investigated. The noted concentrations for TCO-incorporated copolymer are based on the TCO content of the copolymer and not the copolymer concentrations in order to allow for easy comparison with the reaction kinetics of the unincorporated TCO-linkers. Using the ^{177}Lu-DOTA-TZ-1, the chaser agent (0.5 μM) was incubated with NP-82-TCO-A, NP-82-TCO-B and NP-82-TCO-C (4 μM based on TCO content) in PBS at 37 °C. Separation of the unreacted DOTA-

TZ probe from the reaction mixture was performed using centrifugal filter (3 kDa). The radioactivity for each sample was measured by gamma counter (in cpm unit) (Figure 3.15C**Error! Reference source not found.**). The rate constants, maximum observed reaction yield and time to reach maximum yield are listed in Table 3.2. The maximum reaction yields for the copolymers never reached higher than 30% over the 60 min study. This suggested to us that much of the TCO content of the ~100 kDa copolymers is sterically inaccessible to the ^{177}Lu-DOTA-TZ-1 chaser agent (208). To account for this, the rate constants are given in Table 3.2 that do and do not consider the observed reaction plateau as a complete IEDDA reaction. The K_2 value for each reaction was estimated by fitting the data two times in the one-phase association model by adjusting the plateau parameter value at each time. This parameter was not constrained in the first time to estimate the K_2 value based on the accessible TCO within the copolymers. The plateau of the generated best-fit curve using this method represents the maximum observed reaction yield for each TCO/TZ reaction. Estimating the K_2 value using this method would only take into account the accessible (reacted) TCO. In the second time, the plateau parameter was constrained to a value 100, which represents the maximum theoretical reaction yield (100%). NP-82-TCO-C, which contains the longest linker, exhibited the highest reaction yield and a competitive rate constant. Due to this, moving forward, only the HPMA copolymers utilizing the TCO-C linker were investigated.

To examine the impact of the molecular weight of the polymer on the IEDDA reaction, ^{177}Lu-DOTA-TZ-2 (0.5 μM) was reacted with the NP-18-TCO-C and NP-82-TCO-C copolymers (2 μM). The reaction with NP-82-TCO-C plateaued after 5 min suggesting, as mentioned above, that all of the easily accessible TCOs on the surface of the copolymer had undergone reaction. For the NP-18-TCO-C copolymer, the IEDDA reaction proceeded to nearly 90% over the course of 30 min. This indicates that the lower molecular weight reduces steric hindrance and increases TCO accessibility to the ^{177}Lu-DOTA-TZ 2 chaser agent. The rates constant for the smaller NP-18-TCO-C (556 ± 47 $M^{-1}s^{-1}$) was nearly an order of magnitude higher than NP-82-TCO-C (67.9 ± 8.5

$M^{-1}s^{-1}$). Lastly, the reaction kinetics of MP-90-TCO-C with ^{177}Lu-DOTA-TZ 2 was also investigated and found to statistically identical rate constants and reaction yields compared to the NP-82-TCO-C. This suggests that the Cat S-degradable peptides does not influence the IEDDA reaction. However, based on the faster reaction kinetics and higher reaction yields of the NP-18-TCO-C outlined above, reaction kinetics of MP-90-TCO-C would be expected to increase upon fragmentation to smaller TCO-containing copolymer blocks.

Table 3.2 The characteristics of kinetic studies for the reactions between TCO-compounds and DOTA-TZ probes

TCO[a]	Type of DOTA-TZ probe	K_{ob} x 10^5 (s^{-1})[b]	K_2 (M^{-1} s^{-1})[b]	K_{ob} x 10^5 (s^{-1})[c]	K_2 (M^{-1} s^{-1})[c]	Maximum reaction yield	Maximum reaction yield reached at X (min)
TCO-B	1	149 ± 22	373 ± 54			> 95%	30
TCO-C	1	133 ± 5	333 ± 12			> 95%	30
TCO-C	2	1949 ± 148	9745 ± 742			> 95%	3
NP-82-TCO-A	1	8.1 ± 0.3	20.3 ± 0.8	31.9 ± 9.9	79.7 ± 24.8	24 %	60
NP-82-TCO-B	1	3.8 ± 0.3	9.6 ± 0.7	47.6 ± 5.6	119 ± 13	12 %	60
NP-82-TCO-C	1	10.0 ± 2.0	24.9 ± 4.9	28.6 ± 4.3	71.4 ± 10.7	30 %	60
NP-18-TCO-C	2	111.2 ± 9.4	556 ± 47	89.0 ± 10.1	445 ± 50	90%	30
NP-82-TCO-C	2	13.6 ± 1.7	67.9 ± 8.5	807 ± 69	4036 ± 346	~15%	5
MP-90-TCO-C	2	12.6 ± 1.7	63.0 ± 8.5	838 ± 189	4190 ± 946	~15%	5

[a]TCO concentration was 4 μM and 2 μM when DOTA-TZ-1 and DOTA-TZ-2, respectively, were utilized

[b]Data fitted in one-phase association model with two constrains (Y0 = 0, Plateau = 100) to obtain the observed first-order rate constants (K_{ob}), which were utilized for calculating the corresponding estimated the second-order rate constants (K_2)

[c]Data fitted in one-phase association model with one constrain (Y0 = 0) to obtain K_{ob} values, which were utilized for calculating the corresponding estimated K_2 values

All the TCO-HPMA copolymers used in the kinetic studies are non-capped.

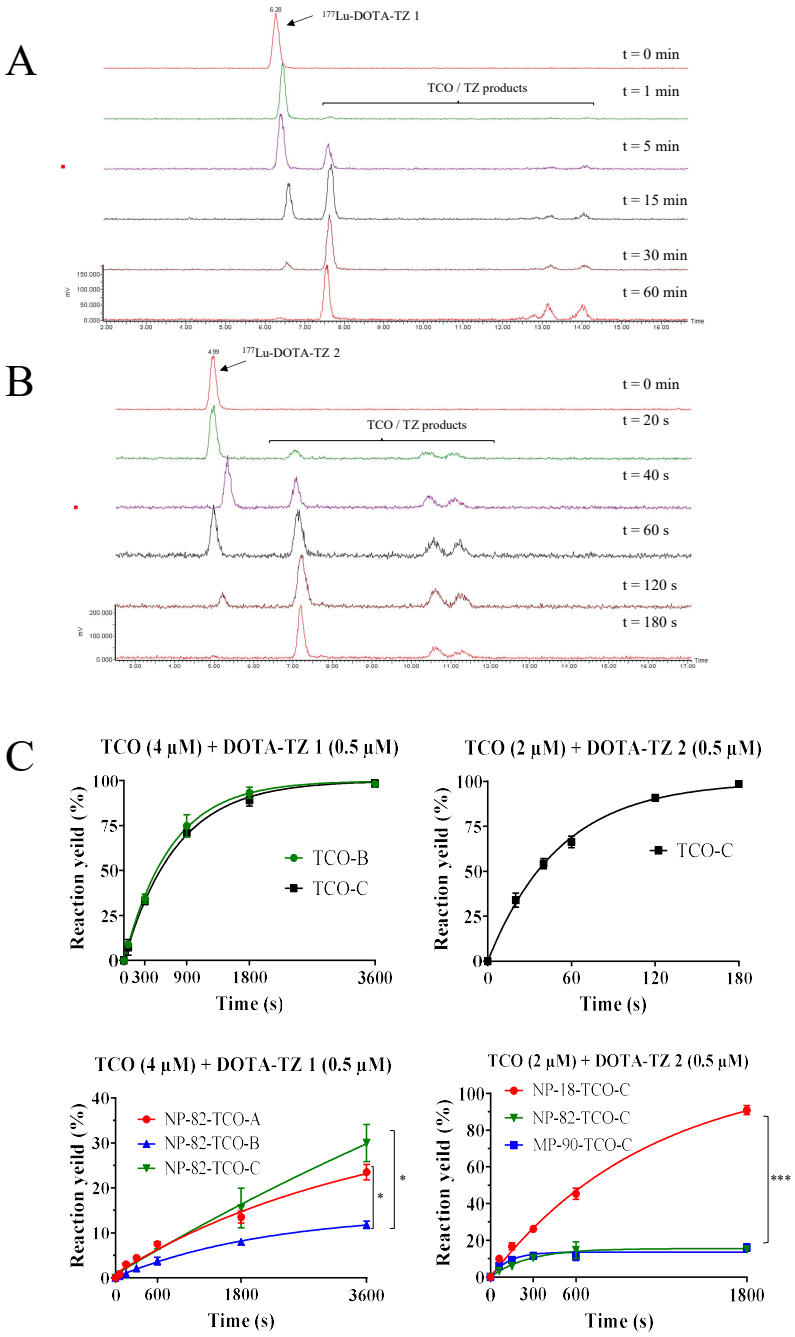

Figure 3.15 Radio-HPLC chromatograms for the reactions between TCO-C and ^{177}Lu-DOTA-T 1(A) and ^{177}Lu-DOTA-TZ 2 (B), and profiles of kinetic studies between DOTA-TZ probes and TCO-linkers / TCO-HPMA copolymers (C). All studies were performed in PBS at 37 ºC. All TCO-HPMA copolymers used for the kinetic studies are non-capped. Data expressed as mean ± SD. * Indicates significance at $p < 0.05$. *** Indicates significance at $p < 0.001$.

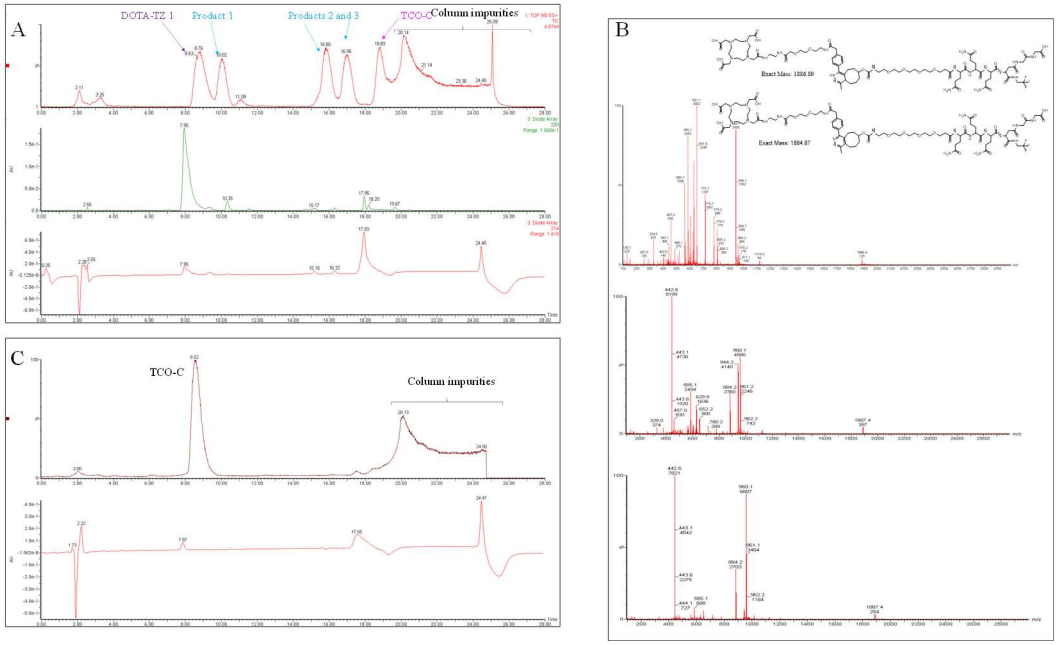

Figure 3.16 LC/MS profile for the reaction between TCO-C and DOTA-TZ 1. The spectrum for a 28-min run (washing phase began at t = 15 min) using gradient separation (90 - 75%) is shown in (A). The molecular weights (M+1) for each of the three new formed peaks due to the TCO/TZ reaction are shown in (B). The spectrum of TCO-C without DOTA-TZ 1 is shown in (C) using a different gradient (75 – 68%).

3.3.9 Stability of the ^{177}Lu-DOTS-TZs in human serum

In order to better understand the potential *in vivo* stability of the ^{177}Lu-DOTA-TZ analogs, the *in vitro* serum stability of ^{177}Lu-DOTA-TZ 1 and ^{177}Lu-DOTA-TZ 2 in human serum was examined over 4 h at 37 °C. At the 0 and 4 h timepoints, an aliquot of each sample was analyzed by the radio-RP-HPLC. As expected, ^{177}Lu-DOTA-TZ 1, which contains the methyltetrazine, exhibited less degradation (~ 89.0) than ^{177}Lu-DOTA-TZ 2 (~ 74.5%) (205). Based on the results from the kinetic and stability studies, ^{177}Lu-DOTA-TZ 2, with its substantially higher IEDDA reaction rate constant and good serum stability, was selected for utilization in all *in vivo* experiments.

3.3.10 *In vivo* Studies

It is known that the large HPMA copolymers (> 50 kDa) circulate for longer times than the smaller copolymers (< 50 kDa), and therefore the large HPMA copolymers show greater tumor accumulations (97, 100). However, the long circulation times of these copolymers lead to greater retentions in the MPS-associated tissues (e.g., liver and spleen) (55, 209). These retentions are considered a major obstacle against the clinical translation of radiolabeled HPMA copolymers (and nanomedicines in general) for radioimaging and radiotherapy of cancer. Previously, our lab developed a strategy to improve the SPECT imaging of pancreatic cancer based on developing large radiolabeled HPMA copolymers (MW ≈ 80 kDa) that can be cleaved by Cat S at the non-target tissues into smaller fragments, which leads to their clearance from these tissues and eventually from the body (117). The strategy is based on the extension of the small single-block HPMA copolymer (MW ≈ 18 kDa) with a Cat S susceptible linker (CL) to afford a larger multi-block HPMA copolymer (MW ≈ 80 kDa). The biodistribution profile of the radiolabeled multi-block HPMA copolymer had similar tumor accumulation (in a pancreatic cancer model) with reduced retentions in the non-target tissues (e.g., liver, spleen, and blood) relative to HPMA copolymers of the same molecular weights but with no CL. The results showed improved SPECT imaging of pancreatic cancer when using the radiolabeled cat S cleavable multi-block HPMA copolymer relative to the non-cleavable HPMA copolymers. These results encouraged us to combine this strategy with an already established pretargeting strategy (*in vivo* TCO/TZ bioorthogonal reaction) that has been shown to improve the tumor to normal tissues (T/NT) ratios of the radiolabeled antibodies/nanomedicines (90, 192, 206, 210). Instead of injecting already radiolabeled antibody/nanomedicine, TCO-modified antibody/nanomedicine is first injected, and the necessary time (e.g., 2 – 3 days) is allowed for the construct to accumulate in the tumor tissues. Then, a radiolabeled TZ probe "chaser agent" is injected to react (ultra-fast reaction rates suitable for radiotracer level) with the already accumulated TCO-modified antibody/nanomedicine at the

tumor tissues to form irreversible covalent bond formation and reside for a long time. The unreacted TZ probe is rapidly excreted from the body with a plasma half-life is in minutes (88).

The feasibility of this approach is dependent on several factors, including efficient tumor accumulation of the TCO-modified construct and its clearance from the non-target tissues (mainly the blood). Unfortunately, injecting the TZ probe in the presence of the TCO-modified construct's traces level can cause a significant premature *in vivo* TCO/TZ reaction in the blood (89, 90). Therefore, we proposed to explore the use of cat S cleavable strategy to reduce the concentration of the HPMA copolymer in the non-target tissues (e.g., blood, liver, and spleen) before injecting the radiolabeled TZ probe. Our goal is to reduce the retention of the TCO-HPMA copolymer in the normal tissues, which would afford improved radioimaging and radiotherapy when the TZ probe is injected. The *in vitro* cat S study revealed that the optimized cat S cleavable TCO-HPMA copolymer (capped MP-90-TCO-C) could indeed be cleaved by cat S into small fragments. These results encouraged us to conduct *in vivo* studies to evaluate our approach.

3.3.10.1Biodistribution in a normal (CF-1) mouse model

We first evaluated the biodistribution of the optimized cat S cleavable TCO-HPMA copolymer (MP-90-TCO-C) and the optimized non-cleavable (NP-82-TCO-C) in a normal (CF-1) mouse model. Both copolymers were capped with glycolic acid (to limit the effect of the positive charges from the unreacted primary amines of the APMA units within the copolymers on the biodistribution of the copolymers) and radiolabeled with ^{177}Lu. The mice were sacrificed after 72 h. As expected, both copolymers showed high retention in the MPS-associated tissues (e.g., liver, spleen, and blood) relative to the remaining tissues Table 3.3. However, the cat S cleavable copolymer (MP-90-TCO-C) showed nearly 36%, 39%, and 42% reduction in the retention (%ID/g) in the liver, spleen, and blood, respectively, relative to the non-cleavable TCO-HPMA copolymer. These retention reductions were accompanied by ~ 22% (%ID) increased excretion of the Cat S cleavable copolymer. The two copolymers had similar molecular weights (108.7 vs. 101.3 kDa).

Therefore, the difference in the biodistribution and excretion profiles were likely due to the *in vivo* degradation of the Cat S cleavable copolymer, which is in agreement with our previous report (117). These results were encouraging, and therefore further evaluations in tumor models were performed. The full data for the biodistribution profiles of the capped NP-82-TCO-C and capped MP-90-TCO-C in the normal (CF-1) mouse model are found in Table 3.3

3.3.10.2 Biodistribution and *in vivo* TCO/TZ reactivity in ovarian cancer models (OVCAR-3 bearing-NOD-SCID and -SCID)

As stated previously, the immune cells such as monocytes and macrophages are associated with MPS uptake, leading to the retention of nanomedicines in tissues like the liver and spleen (55). Cat S is highly expressed in such immune cells, including monocytes, macrophages, and professional antigen-presenting cells (APCs) (e.g., B-lymphocytes and dendritic cells) (114). Therefore, since our strategy using a Cat S cleavable HPMA copolymer is exploiting the expression of Cat S in these immune cells, conducting biodistribution and TCO/TZ reactivity studies for the Cat S cleavable HPMA copolymer in mouse models with different immunity profiles (e.g., normal vs. deficient macrophages) can lead to different results.

Unlike CF-1 mouse model that has normal immunity profiles (e.g., normal counts of T and B lymphocytes and macrophages), SCID mice lack mature B and T lymphocytes due to non-homologous end-joining defects in *Prkdc*^{scid} mutants (211). In addition, NOD mice have defects in the macrophage function, complement pathway, and natural killer cell activity (211-213). Transferring SICD mutation onto a NOD background to afford NOD-SCID mice results in a more severe immune deficiency that combines both NOD and SCID mice's defects. Therefore, to accounts for these variations in the counts of immune cells, which can lead to variations in the expression level of Cat S, we conducted biodistribution and *in vivo* TCO/TZ reactivity studies in two ovarian cancer models (OVCAR-3 bearing-NOD-SCID and -SCID mice).

To perform biodistribution and *in vivo* TCO/TZ reactivity studies, each mouse was injected with two radiolabeled constructs, a ^{111}In-radiolabeled TCO-HPMA copolymer and a ^{177}Lu-radiolabeled TZ-DOTA 2 probe. Unless otherwise indicated, the term biodistribution describes the biodistribution of ^{111}In-radiolabeled TCO-HPMA copolymer, and the term *in vivo* TCO/TZ reactivity describes the biodistribution of ^{177}Lu-DOTA-TZ 2 probe (0.37 MBq, 10 μCi) in mice pre-injected with TCO-HPMA copolymer based on TCO content of 23 nmol (mixed with ^{111}In-radiolabeled of the same TCO-copolymer, 0.37 MBq (10 μCi)). After the mouse was sacrificed, a dual-isotope strategy was performed to trace the ^{111}In-TCO-HPMA copolymer and ^{177}Lu-DOTA-TZ 2 probe in the same excised tissue. To differentiate the ^{111}In signal from the ^{177}Lu signal, we selected a region of interest (ROI) in the NaI (Tl) well detector based on the energy spectra of the two radioisotopes. We were able to identify the signal (and count) of each radioisotope from the same sample (e.g., excised tissue). We also prepared a standard curve for each radioisotope to confirm the accuracy of the counts. The selected ROI is shown in Figure 3.17. In the top image of Figure 3.17A, the selected ROI is shown in the presence of no radioisotope (background counts). Representative examples of ^{111}In and ^{177}Lu spectra are shown in the middle and bottom images, respectively. The ^{111}In and ^{177}Lu signals appeared in the high and low energy levels, respectively. The corresponding standard curves for the ^{111}In and ^{177}Lu counts (at high and low energy levels) vs. different radioactivity amounts (in μCi) are shown in Figure 3.17B snd 3.17C respectively.

3.3.10.2.1 Biodistribution and *in vivo* TCO/TZ reactivity study in ovarian tumor-bearing NOD-SCID mice

A total of five groups (5 mice per group) was included in the biodistribution and *in vivo* TCO/TZ reactivity study in ovarian tumor-bearing NOD-SCID mice. Each group received either non-capped NP-82-TCO-C, capped NP-18-TCO-C, capped NP-82-TCO-C, capped MP-90-TCO-C, and no treatment (control). Each TCO-HPMA copolymer was mixed with the corresponding ^{111}In-radiolabeled copolymer. For example, non-capped NP-82-TCO-C was premixed with ^{111}In-

radiolabeled non-capped NP-82-TCO-C. After 72 h of administration, all the five groups (including the control group) were injected with ^{177}Lu-DOTA-TZ 2, and the mice were sacrificed 4 h later.

3.3.10.2.1.1 Biodistribution profile of DOTA-TZ 2

As expected, the DOTA-TZ 2 (control group) was almost completely excreted (98 ± 1 %ID) from the body at the time of sacrifice (4 h) (Table 3.4). The kidneys showed nearly 1.3 ID%/g, which was the organ with the highest %ID/g of ^{177}Lu-DOTA-TZ 2. These results indicate the rapid excretion of ^{177}Lu-DOTA-TZ 2, which agree with reports using similar probes (88, 205).

3.3.10.2.1.2 Biodistribution and *in vivo* reactivity profiles of capped NP-18-TCO-C

We investigated the biodistribution and the *in vivo* TCO/TZ reactivity of a small-molecular size TCO-HPMA copolymer (22.7 kDa), capped NP-18-TCO-C, to predict the behavior of the small fragments of Cat S cleavable HPMA copolymer after cleavage by Cat S. We found nearly 97% of this small TCO-HPMA copolymer was excreted, with no tumor accumulation Table 3.4. This result was expected based on the molecular size that is less than the renal threshold (< 50 kDa) (97, 107). This copolymer's high excretion profile led to very poor *in vivo* TCO/TZ reactivity when ^{177}Lu-DOTA-TZ 2 was administered.

3.3.10.2.1.3 Biodistribution and *in vivo* reactivity of the large copolymers (capped NP-82-TCO-C and capped MP-90-TCO-C)

The larger capped TCO-HPMA copolymers (capped NP-82-TCO-C and capped MP-90-TCO-C) showed lower excretion rates than the smaller capped TCO-polymer conjugate. The excretions of the NP-82-TCO-C and MP-90-TCO-C were 8.8 ± 2.5 and 11.3 ± 2.8 %ID, respectively (Table 3.4). However, there was no difference ($p > 0.05$) in the biodistribution profiles of the two large capped TCO-HPMA copolymers. The organs with the highest retentions were the spleen (capped NP-82-TCO-C = 21 ± 7 %ID/g and MP-90-TCO-C = 26 ± 12) and the liver (capped NP-82-TCO-C = 20 ± 2.5 %ID/g and MP-90-TCO-C = 14.8 ± 5.2 %ID/g). The average retentions of the two copolymers in the blood were comparable to the tumor retentions, 12.4 ± 6.0 vs. 11.6 ± 5.0 %ID/g for the capped NP-82-TCO-C and 11.5 ± 0.6 vs. 9.8 ± 3.0 %ID/g for the capped MP-90-TCO-C.

The similar biodistribution profiles of both capped NP-82-TCO-C and capped MP-90-TCO-C (specifically in the spleen, liver, and blood) indicate that the *in vivo* cleavage of the latter copolymer in this mouse model was insignificant. A possible explanation of the lack of biodegradation in this tumor-bearing mouse model is the lack of some immune cells (e.g., macrophages) associated with increased expression of Cat S enzyme (114, 116, 212, 214).

The *in vivo* TCO/TZ reactivity profiles of the two copolymers (capped NP-82-TCO-C and capped MP-90-TCO-C) were very high relative to the control (no TCO pre-injection), but they did not differ from each other. The %ID of ^{177}Lu-DOTA-TZ 2 remained in the body after 4 h of administration were 58% and 64% ($p > 0.05$) in the mice pre-injected with the capped NP-82-TCO-C and the capped MP-90-TCO-C, respectively, relative to only 2% in the control group ($p < 0.001$). The %ID/g found in the tumor tissues were 2.5 ± 1.6 and 2.0 ± 0.7% ($p > 0.05$) in the mice pre-injected with the capped NP-82-TCO-C and the capped MP-90-TCO-C, respectively, indicating the *in vivo* TCO/TZ reactivity at the tumor tissues. However, the majority of the reacted ^{177}Lu-DOTA-TZ 2 was found in the blood for both copolymers. The %ID/g of ^{177}Lu-DOTA-TZ 2 in the blood was approximately ten-fold greater than the %ID/g in the tumor tissues of mice pre-injected with either of the copolymers. The tumor tissues ranked the seventh in terms of excised organs/tissues with the highest %ID/g of ^{177}Lu-DOTA-TZ 2 in mice pre-injected with either of the two copolymers, after the blood, lung, heart, kidneys, liver, and spleen.

3.3.10.2.1.4 Biodistribution and *in vivo* reactivity of the large non-capped non-cleavable copolymer (non-capped NP-82-TCO-C)

To evaluate the effect of the charge on the biodistribution and *in vivo* TCO/TZ reactivity, we also evaluated the non-capped NP-82-TCO-C. The unreacted primary amines of APMA units within this copolymer were not reacted with glycolic acid. Therefore, it is expected at physiologic condition (pH = 7.4), the copolymer becomes positively charged. An earlier investigation of the charge effect on the biodistribution of HPMA copolymers showed faster clearance for the positively charged vs. neutrally charged copolymers (107). Indeed, after 76 h of administration, the non-

capped NP-82-TCO-C showed greater excretion value relative to the capped NP-82-TCO-C (48 ± 8 vs. 8.8 ± 2.5 %ID/g, $p < 0.001$) (Table 3.4). Increased excretion was associated with increased renal retention (167, 215). It was also associated with reduced tumor accumulation by more than 50% relative to the capped copolymer (5.2 ± 0.3 vs. 11.6 ± 6.0) and retention in non-target tissues (e.g., blood and liver). The faster clearance rate of non-capped NP-82-TCO-C relative to the capped NP-82-TCO-C was also associated with reduced *in vivo* TCO/TZ reactivity. While nearly 58 %ID of ^{177}Lu-DOTA-TZ 2 remained in the body of the mice pre-injected with the capped NP-82-TCO-C, only 7 %ID/g remained in the body of the mice pre-injected with non-capped NP-82-TCO-C. Similar to the profile of the capped NP-82-TCO-C, the blood contained the highest %ID/g of ^{177}Lu-DOTA-2, with the tumor tissues being the seventh-highest %ID/g among the excised organs/tissues. In addition, the %ID/g of the probe in the tumor tissues was approximately 13-fold lower when mice pre-injected with the non-capped relative to the capped NP-82-TCO-C. Therefore, in the next *in vivo* study, we used only the capped copolymers.

3.3.10.2.2 Biodistribution and *in vivo* TCO/TZ reactivity studies in ovarian tumor-bearing SCID mice

In an attempt to address the high TCO/TZ reaction in off-target tissues (mainly the blood) and the insignificant *in vivo* degradation of the cleavable copolymer (MP-90-TCO-C), the biodistribution and TCO/TZ reactivity studies were also evaluated in tumor bearing-SCID mouse model (Table 3.5). Unlike the NOD-SCID model, the SCID mouse model does not have a deficiency in dendritic and macrophage cells, which are highly expressing Cat S (211, 212). Therefore, we anticipated the cleavable copolymer would be degraded into smaller fragments, due to Cat S cleavage, in the SCID mouse model. In addition, due to the high retentions of the large TCO-HPMA copolymers (including the capped MP-90-TCO-C) in the previous *in vivo* study using NOD-SCID, we explored the utility of a masking agent (DP-TZ). This masking agent consists of a dextran-polymer that is modified with TZ moieties. It has been demonstrated in a previous report that injecting this masking agent several minutes to one hour before injecting the TZ probe can deactivate the remaining TCOs (due to the presence of TZ moieties) in the blood without affecting

the TCOs in the tumor tissues (89). We utilized this masking agent to reduce the TCO/TZ reactivity at the non-target tissues (mainly the blood).

The mice were injected with either the capped NP-82-TCO, capped MP-TCO-C without the masking agent, or capped MP-TCO-C with masking agent (TZ content = 60 nmol) followed by injection of ^{177}Lu-DOTA-TZ 2. The masking agent was injected 30 min before injecting the ^{177}Lu-DOTA-TZ 2. The biodistribution profiles of the TCO-HPMA copolymers were also comparable in the NOD-SCID model, with no apparent advantages of using the Cat S susceptible linker in MP-TCO-C (Table 3.5). The lack of the difference in the biodistribution profiles between the cleavable and non-cleavable copolymers indicates the lack of biodegradation of the cleavable copolymer. Although no attempt was made to explore the reasons, a possible explanation would be the negative impact of the hydrophobic TCO on the *in vivo* biodegradation (216). The excretions (%ID) were nearly 11% for both copolymers, with no statistical difference in the group administered DP-TZ (12.7 ± 8.5 %ID).

The estimated TCO/TZ reactions were also similar between the two copolymers. The %ID/g of ^{177}Lu-DOTA-TZ 2 remained in the body were 45 and 43 %ID/g in the mice pre-injected with the capped NP-82-TCO-C and capped MP-90-TCO-C, respectively. Similar to the previous *in vivo* TCO/TZ reactivity studies using NOD-SCID, the majority of the TCO/TZ reaction occurred in the blood. The administration of the masking agent (30 min before the ^{177}Lu-DTOA-TZ 2 probe) before the ^{177}Lu-DOTA-TZ probe administration reduced the *in vivo* TCO/TZ reactivity (between the capped MP-90-TCO-C and the TZ probe) to afford only 11 versus 47 %ID (with no pre-administered DP-TZ) of ^{177}Lu-DOTA-TZ 2 remained in the body. This reduction in the TCO/TZ reactivity is mainly attributed to the reduction of reactivity in the blood due to the deactivation of the circulating TCOs within the capped MP-90-TCO-C. The %ID/g of ^{177}Lu-DOTA-TZ 2 was reduced in all the excised tissues, but the blood had the highest reductions (16.4 versus 0.7 %ID/g, $p < 0.001$), which afforded nearly 23 folds reduction.

Poor T/NT ratios were found for the ^{177}Lu-DOTA-TZ 2 in the groups that were preinjected with either the capped NP-82-TCO-C or capped MP-90-TCO-C (with no masking agent). However, in the group pre-injected with both the capped MP-90-TCO-C and the masking agent, T/NT ratios were significantly improved. Using the masking agent led the tumor tissues to contain the second-highest %ID/g of ^{177}L-DOTA-TZ 2 (after only the kidney) relative to the seventh-highest %ID/g in the group with no pre-injection of the masking agent (Table 3.5 and Figure 3.18). Due to the limited extravasation of the masking agent outside the systemic circulation (89), this improved T/NT ratio is mainly based on the deactivation of the reactive TCOs remaining in the blood without impacting the TCOs in the tumor tissues.

Table 3.3 Biodistribution of TCO-HPMA copolymers in normal (CF-1) mice

	^{177}Lu-NP-82-TCO-C (%ID /g)	^{177}Lu-MP-90-TCO-C (%ID / g)
Blood	6.2 ± 0.9	3.6 ± 0.6
Heart	3.0 ± 0.3	2.4 ± 0.5
Lung	4.3 ± 4.0	2.6 ± 0.7
Liver	11.0 ± 1.6	7.0 ± 0.8
Pancreas	2.6 ± 1.0	1.1 ± 0.5
Stomach	1.0 ± 0.3	0.88 ± 0.27
Spleen	18 ± 4	11.0 ± 2.2
Small intestine	1.1 ± 0.4	0.7 ± 0.22
Large intestine	0.75 ± 0.16	0.91 ± 0.22
Kidney	3.5 ± 0.8	2.6 ± 0.4
Muscle	1.0 ± 0.1	1.1 ± 0.3
Bone	1.4 ± 0.4	1.0 ± 0.6
Brain	0.54 ± 0.10	0.57 ± 0.20
Excretion (%ID)	32 ± 2	39 ± 4

Values represent mean ± SD (n = 5).

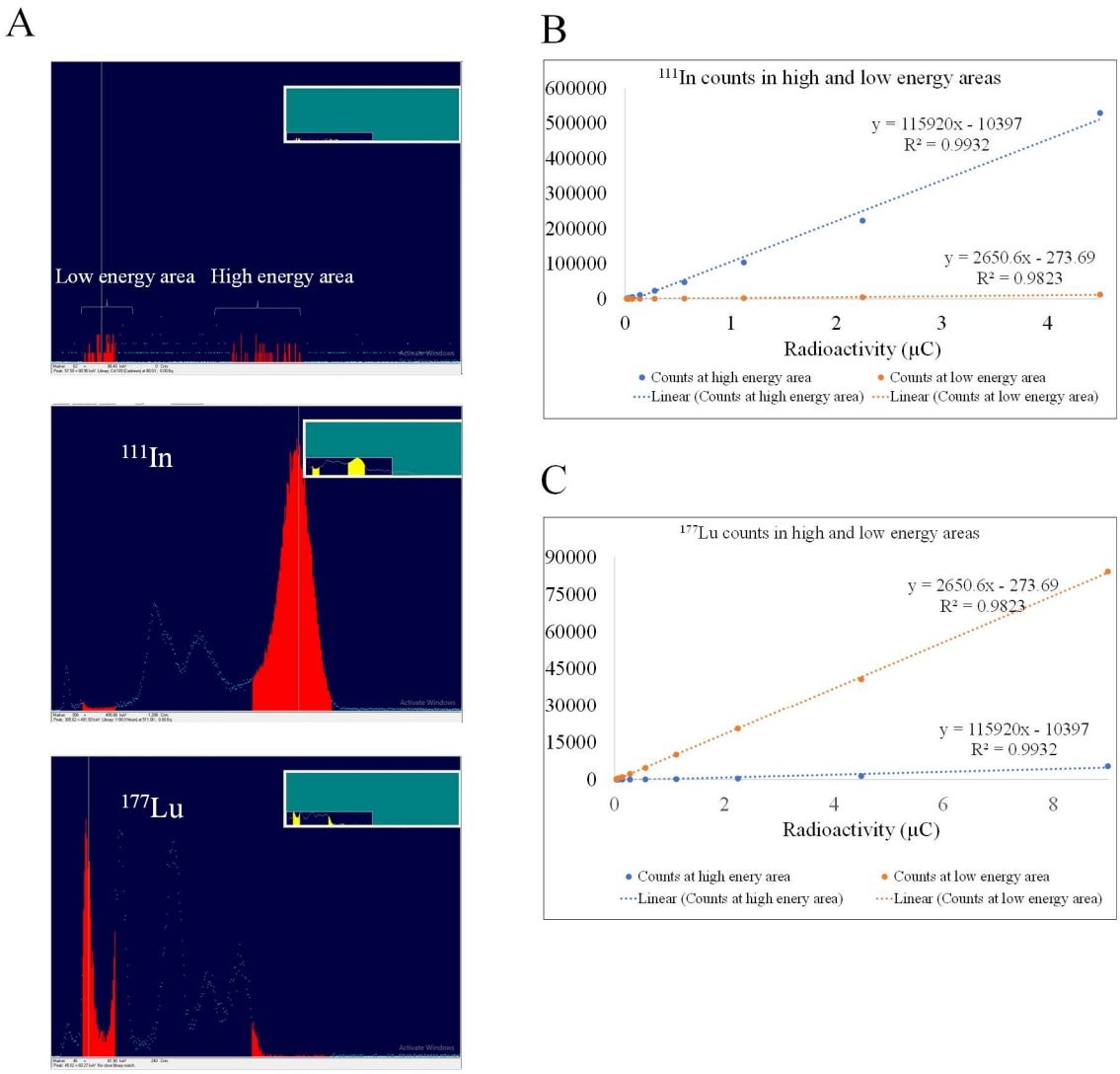

Figure 3.17 The selected region of interest (ROI) used for the dual-radioisotope studies. The spectrum with no radioisotope, with only ^{111}In, and only ^{177}Lu are shown in (A). The counts at high and low energy areas for ^{111}In and ^{177}Lu are shown in (B) and (C), respectively.

Table 3.4 Biodistribution and TCO/TZ reactivity profiles of selected TCO-HPMA copolymers and biodistribution of ^{177}Lu-DOTA-TZ 2in NOD-SCID mice (%ID/g)

	Capped NP-18-TCO-C		Capped NP-82-TCO-C		Capped MP-90-TCO-C		Non-capped NP-82-TCO-C		^{177}Lu-DOTA-TZ 2
	^{111}In	^{177}Lu	^{111}In	^{177}Lu	^{111}In	^{177}Lu	^{111}In	^{177}Lu	^{177}Lu
Blood	0 ± 0	0 ± 0	12.4 ± 6.0	22 ± 4	11.5 ± 0.6	23 ± 1	5.6 ± 1.0	1.8 ± 0.3	0 ± 0
Heart	0 ± 0	0 ± 0	8.3 ± 3.3	6.6 ± 3.8	7.7 ± 4.7	6.6 ± 4.5	2.6 ± 0.5	0.2 ± 0.2	0 ± 0
Lung	0 ± 0	0 ± 0	3.7 ± 0.6	7.3 ± 0.9	5.2 ± 1.1	7.0 ± 2.2	3.5 ± 0.9	0.5 ± 0.2	0.03 ± 0.03
Liver	0.60 ± 0.01	0.29 ± 0.17	20.0 ± 2.5	3.6 ± 0.7	14.8 ± 5.2	4.0 ± 0.2	8.8 ± 1.8	0.6 ± 0.1	0.21 ± 0.05
Pancreas	0 ± 0	0 ± 0	3.5 ± 0.8	1.8 ± 0.7	2.8 ± 0.8	1.5 ± 0.4	1.9 ± 0.9	0.04 ± .06	0 ±0
Stomach	0 ± 0	0 ± 0	2.4 ± 0.6	1.0 ± 0.2	1.8 ± 0.3	1.3 ± 0.5	1.1 ± 0.6	0.12 ± 0.14	0.02 ± 0.04
Spleen	0.18 ± 0.30	0 ± 0	21 ± 7	3.7 ± 1.7	26 ± 12	3.7 ± 2.5	20 ± 10	0 ± 0	0 ± 0
Small intestine	0.04 ± 0.02	0.04 ± 0.01	3.8 ± 0.7	1.4 ± 0.4	1.9 ± 0.6	1.2 ± 0.4	1.4 ± 0.4	0.16 ± .04	0.10 ± 0.07
Large intestine	0.12 ± 0.10	0.51 ± 0.17	2.3 ± 0.3	1.7 ± 0.7	2.4 ± 0.4	1.8 ± 0.7	1.6 ± 0.4	0.6 ± 0.3	0.48 ± 0.14
Kidney	2.9 ± 0.9	2.1 ± 1.1	6.9 ± 1.1	4.3 ± 1.0	8.5 ± 1.3	4.6 ± 0.5	42 ± 7	1.5 ± 0.2	1.3 ± 0.3
Tumor	0.03 ± 0.05	0 ± 0	11.7 ± 5.0	2.5 ± 1.6	9.8 ± 3.0	2.0 ± 0.7	5.2 ± 0.3	0.19 ± 0.18	0 ± 0
Muscle	0 ± 0	0 ± 0	2.5 ± 0.4	1.0 ± 0.2	2.7 ± 0.6	0.85 ± 0.20	1.0 ± 0.3	0.05 ± 0.06	0 ± 0
Bone	0 ± 0	0 ± 0	2.9 ± 3.6	1.4 ± 0.6	5.9 ± 3.4	2.0 ± 1.2	2.1 ± 0.9	0.03 ± 0.03	0 ± 0
Brain	0 ± 0	0 ± 0	0.26 ± 0.09	0.64 ± 0.13	0.40 ± 0.06	0.63 ± 0.13	0.16 ± 0.06	0 ± 0	0 ± 0
Excretion (%ID)	97 ± 1	98 ± 1	8.8 ± 2.5	42 ± 6	11.3 ± 2.8	36 ± 2	48 ± 8	93 ±1	98 ± 1

Values represent mean (%ID/g) ± SD (n = 5).

Table 3.5 Biodistribution and *in vivo* TCO/TZ chemistry profiles of the capped TCO-HPMA copolymers in SCID mice based on dual-radioisotope study (^{111}In-TCO-HPMA copolymer and ^{177}Lu-DOTA-TZ 2 probe)a

	Capped NP-82-TCO-C		Capped MP-90-TCO-C		Capped MP-90-TCO-C + DP-TZ		^{177}Lu-TZ-2
	^{111}In[b]	^{177}Lu[c]	^{111}In[b]	^{177}Lu[c]	^{111}In[b]	^{177}Lu[c]	^{177}Lu[d]
Blood	15.4 ± 2.1	17.4 ± 2.9	12.2 ± 0.6	16.4 ± 1.5	12.5 ± 3.5	0.70 ± 0.28	0 ± 0
Heart	5.4 ± 0.7	2.9 ± 0.8	4.8 ± 1.4	2.6 ± 0.6	4.2 ± 1.0	0.06 ± 0.07	0 ± 0
Lung	6.0 ± 1.8	5.1 ± 1.1	6.4 ± 0.6	5.4 ± 1.3	6.3 ± 1.3	0.93 ± 0.40	0.03 ± 0.03
Liver	13.0 ± 1.0	3.8 ± 0.8	13.6 ± 0.8	3.2 ± 0.4	12.4 ± 1.2	0.60 ± 0.09	0.21 ± 0.05
Pancreas	2.3 ± 0.2	0.83 ± 0.30	2.4 ± 0.2	1.1 ± 0.3	2.6 ± 0.2	0.09 ± 0.06	0 ± 0
Stomach	1.4 ± 0.3	0.59 ± 0.19	1.6 ± 0.3	0.8 ± 0.3	1.6 ± 0.2	0.02 ± 0.04	0.02 ± 0.04
Spleen	39 ± 13	7.5 ± 3.2	42 ± 11	4.2 ± 2.0	35 ± 15	0.12 ± 0.24	0 ± 0
Small intestine	1.6 ± 0.2	0.66 ± 0.34	2.0 ± 0.5	1.1 ± 0.4	2.2 ± 0.4	0.29 ± 0.09	0.10 ± 0.07
Large intestine	1.0 ± 0.4	1.0 ± 0.3	1.8 ± 0.5	4.1 ± 1.4	1.7 ± 0.4	0.84 ± 0.53	0.48 ± 0.14
Kidney	5.6 ± 1.2	3.6 ± 1.0	7.2 ± 2.4	2.5 ± 0.7	8.1 ± 1.9	1.8 ± 0.5	1.3 ± 0.3
Tumor	13.9 ± 3.2	2.4 ± 0.6	12.0 ± 2.8	2.5 ± 0.7	14.1 ± 1.8	1.2 ± 0.5	0 ± 0
Muscle	2.5 ± 0.5	0.65 ± 0.15	2.4 ± 0.4	0.81 ± 0.24	2.2 ± 0.4	0.18 ± 0.26	0 ± 0
Bone	2.6 ± 0.4	0.42 ± 0.33	2.8 ± 0.4	0.71 ± 0.57	2.6 ± 0.4	0 ± 0	0 ± 0
Brain	0.48 ± 0.21	0.24 ± 0.19	0.30 ± 0.05	0.28 ± 0.08	0.34 ± 0.08	0 ± 0	0 ± 0
Excretion (%ID)	11.0 ± 0.8	55 ± 4	10.8 ± 2.4	53 ± 5	12.7 ± 8.5	89 ± 1	98 ±1

[a]Two reading counts (from high and low energy areas) were obtained for each tissue to estimate the ^{111}In and ^{177}Lu signals

[b]Data for the biodistribution profiles of ^{111}In-labeled TCO-HPMA copolymer (76 h)

[c]Data for the biodistribution profiles of ^{177}Lu-DOTA-TZ 2 (4 h) in mice pre-administered with the designated TCO-HPMA copolymer (72 h)

[d]Data for the biodistribution profiles of ^{177}Lu-DOTA-TZ 2 (4 h) in NOD-SCID mice (control), with no pre-administered compound

Data expressed as mean ± SD (n = 5)

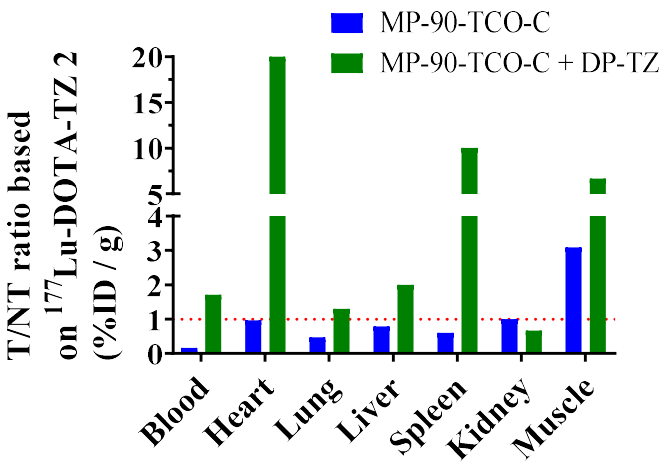

Figure 3.18 Effect of DP-TZ on tumor / normal tissues (T/NT) ratios. Blue columns represent data from SCID mice that were injected with MP-90-TCO-C followed by injection of ^{177}Lu-DOTATZ 2 before animal sacrifice. Green columns represent data from SCID mice that were injected with MP-90-TCO-C followed by injection DP-TZ and finally injection of ^{177}Lu-DOTA-TZ 2 before animal sacrifice. Data expressed as mean (n = 5).

3.4 Conclusion

In this study, a multi-block Cat S-susceptible HPMA copolymer modified with TCO (MP-90-TCO-C) was synthesized and characterized for *in vivo* pretargeting via bioorthogonal reaction. We evaluated the effect of the TCO linker length, TZ moiety type, molecular size, and the introduction of a Cat S cleavable linker to the HPMA copolymer on the reaction kinetics. The *in vitro* Cat S cleavage study revealed the optimized Cat S cleavable copolymer's susceptibility to the enzyme. The *in vivo* studies were conducted to evaluate the biodegradation of the cleavable TCO-HPMA copolymer in mouse models with different immunity profiles, the feasibility of *in vivo* TCO/TZ pretargeting in ovarian-cancer models, and the effect of the charge on the biodistribution and *in vivo* TCO/TZ pretargeting of the TCO-HPMA copolymers. The biodistribution of MP-90-TCO-C in a CF-1 mouse model showed *in vivo* biodegradation. The *in vivo* TCO/TZ reactivity studies in ovarian cancer models showed the feasibility of using HPMA copolymer for the pretargeting approach, with excellent T/NT ratios when a masking agent was pre-injected. The positively-charged copolymer containing free amines showed greater clearance with lower *in vivo* TCO/TZ reactivity profiles relative to the capped copolymers, indicating a significant role for the charge. Overall, these results are promising and present a proof of concept for further optimization.

4 Chapter 4. Prophylactic Chelation Therapy Using DTPA-HPMA Copolymer (P-DTPA): *In vitro* and *In vivo* Evaluations

4.1 Introduction

Actinides such as plutonium, uranium and americium are widely used for medical, industrial, and military purposes (134). Their release, caused by natural disasters, industrial or military accidents, or terrorist attacks, remains a major potential public health concern (217). Internal contamination by actinides can occur via inhalation, ingestion, and absorption through wounds. Once absorbed, these radiometals make their way to the blood circulation where they are systemically distributed throughout the body. This leads to the actinide being either excreted from the body or being deposited in tissues, most commonly the liver and bone (217). Tissue deposition of these radioactive metals is known to cause serious adverse effects (e.g., cancer) as a result of long-term exposure (218).

The current clinical treatment for internal contamination is chelation therapy (219). This approach involves the administration of small organic ligands that selectively form stable and water-soluble complexes with deposited actinides to enhance clearance from the body. Currently, DTPA (as $CaNa_3$ and $ZnNa_3$ salt forms) is the only FDA-approved medication for the chelation therapy for individuals contaminated with plutonium, americium or curium (220). While clearly an important treatment regimen, DTPA is not a panacea for all actinide-based cases of internal contamination. The oxidation state and coordination chemistry of the actinide and localization (intracellular vs. extracellular) greatly impacts the efficacy of the chelation agent. Due to this, a variety of investigators are pursuing the development of chelation agents with more optimal chelation and bioavailability characteristics (134, 221, 222).

The development of prophylactic chelation therapy approaches has been of interest for the protection of individuals at risk of exposure due to the intentional or accidental release of actinides into the environment. DTPA is not ideal for this purpose due to its poor oral bioavailability and rapid clearance from the blood circulation limiting its duration of prophylactic protection (139). One approach in the development of effective prophylactic chelation therapies is to incorporate chelation agents into nanomedicine constructs (e.g., liposomes, micelles, and polymeric conjugates) (144, 145, 223-225). This approach is attractive due to its ability to greatly increase the circulation time of the chelation agent in the blood thereby allowing the maintenance of effective concentrations to intercept absorbed actinides before tissue deposition occurs. Additionally, the versatility of nanomedicine constructs allows for the design and development of multi-functional platforms (226). For instance, in the context of chelation therapy, this could include the creation of formulations that contain two or more chelators to optimize the capture and clearance of a specific or a broad set of actinides from the body.

Herein, we explore the development of a nanomedicine-based prophylactic chelation therapeutic. Specifically, we have designed and synthesized a polymer conjugate construct in which DTPA is incorporated into a N-(2-hydroxypropyl)methacrylamide (HPMA) copolymer. HPMA copolymers were chosen as the carrier platform due to their non-immunogenic, biocompatible, and non-toxic nature (97, 227) as well as being able to be administered via different routes (e.g., i.v. and s.c.) (228). Additionally, HPMA copolymer constructs have undergone multiple clinical trials and demonstrated their safety as nanomedicine drug carriers (164, 229). Our aim is to examine if a DTPA-incorporated HPMA copolymer (P-DTPA) exhibits increased radionuclide removal and prophylactic protection relative to DTPA. To achieve this goal, the lanthanide Lu-177 served as our actinide model due to our institutions' regulatory prohibition on actinide possession. Lutetium has a similar oxidation state, coordination chemistry and DTPA formation constant (Lu = $10^{22.4}$ and Am=$10^{23.1}$) compared to americium (230). P-DTPA was characterized using a variety of *in vitro* studies to examine the selectivity, stability, and cytotoxicity of the carrier. *In vivo* studies were

carried out in a CF-1 mouse model to investigate the prophylactic protection of P-DTPA against exposure to radiometal contamination.

4.2 Materials and methods

4.2.1 Chemicals

If not otherwise indicated, all solvents used for the polymer reactions and silica gel purifications were ACS grade obtained from Fisher Scientific. Water was deionized using a Milli-Q® Integral Water Purification System (Millipore Corp., U.S.). Acetonitrile (ACN) was HPLC grade and purchased from Fisher Scientific (U.S.). N,N-dimethylformamide (DMF) was purchased from Fisher Scientific (U.S.). Fluorescein isothiocyanate (FITC), 4-cyano-4-(phenylcarbono-thioylthio)pentanoic acid (chain transfer agent, CTA), 2,2′-Azobis(2-methylpropionitrile) (AIBN), and ethylenediaminetetraacetic acid (EDTA) were purchased from Sigma-Aldrich (U.S.). N-(2-Hydroxypropyl)methacrylamide (HPMA) and N-(3-aminopropyl)methacrylamide (APMA) were obtained from Polysciences (U.S.). S-2-(4-Isothiocyanatobenzyl)-diethylenetriamine pentaacetic acid (p-SCN-Bn-DTPA) was purchased from Macrocyclics (U.S.). Diethylenetriaminepentaacetic acid calcium trisodium salt (DTPA) was acquired from TCI America (U.S.). N,N-Diisopropylethylamine (DIEA) was obtained from ChemPep (U.S.). Phosphate buffered saline (PBS) was purchased from Fisher Scientific (U.S.). Human type AB serum was obtained from Fisher BioReagents (U.S.). Ham's F-12K medium and fetal bovine serum (FBS) were obtained from Gibco (U.S.). L-glutamine and PrestoBlue® were purchased from Thermo Fisher Scientific (U.S.). Endothelial cell growth supplement was obtained from R&D Systems (U.S.). Zeba™ Spin Desalting Columns (7K MWCO, 0.5 mL) were purchased from Thermo Fisher Scientific (U.S.). Silica Gel 60 A was obtained from Sigma-Aldrich (U.S.).

4.2.2 Instrumentation

A Waters Qtof Micro electrospray ionization mass spectrometer (U.S.) was used to perform mass characterization of the small molecules. A Bruker Avance-III HD 600 MHz instrument (U.S.)

was used to record ^{1}H-NMR. Weight and size measurements of the HPMA copolymer was performed using a Viscotek TDA max system (Malvern Instruments Inc., U.S.) equipped with a Shodex Asahipak GF-510 HQ size exclusion chromatography column (SEC-TDA). Evaluation and/or purification of radiolabeled chelators were performed on a Waters 1515 binary pump equipped with a Waters 2489 absorption detector and a Bioscan Flow Count radiometric detector system. A Shodex Asahipak GF-510 HQ GPC column was employed for the purification and evaluation of the radiolabeled copolymeric chelator. Autoradiography was recorded via BAS storage phosphor screens and scanned by a GE Lifesciences Typhoon FLA 9500 variable mode imager. A Multi-Wiper nuclear medicine gamma counter (LTI, U.S.) was used for counting the radioactivity in the selectivity and *in vitro* chelation studies. A Tecan Infinite F200 Fluorescence Microplate Reader (Switzerland) was used for the cytotoxicity studies. A CRC-25R dose calibrator (U.S.) was used for measuring the radioactivity for the serum chelation study. Quantitative measurement of the *in vivo* administered ^{177}Lu was performed using a NaI (Tl) well detector constructed by AlphaSpectra Inc. (U.S.).

4.2.3 Synthesis and characterization of the DTPA-modified HPMA copolymer (P-DTPA)

4.2.3.1 Synthesis of monomers

The APMA-DTPA monomer was synthesized according to a published report (231). Briefly, to a solution of APMA (0.154 mmol, 27.5 mg) in 300 µL dry DMF was added to a solution of p-SCN-Bn-DTPA (0.154 mmol, 100 mg) in 500 µL dry DMF followed by the addition of DIEA (0.769 mmol). The reaction mixture was stirred at room temperature under nitrogen. After 24 h, the crude product was concentrated by purging with nitrogen and was purified by silica gel column chromatography using an elution system containing isopropyl alcohol/water/NH_4OH (8:1:1). The solvent was evaporated under vacuum to afford the product as a solid residue (53.3 mg, 50.7%).

The product was characterized by ^{1}H-NMR and mass spectrometry ($[M+H]^{+}$ = 683.1). APMA-FITC was synthesized according to a previously published report (168).

4.2.3.2 Reversible addition-fragmentation chain transfer (RAFT) polymerization

With modifications made to our previously described published method (203), reversible addition-fragmentation chain transfer (RAFT) polymerization was employed to synthesize the HPMA-DTPA copolymer (P-DTPA). Briefly, HPMA, APMA-DTPA, and APMA-FITC monomers were dissolved in dioxane/DI water (2:1) at a molar ratio of 89.5, 10.0, and 0.5, respectively, with a total monomer concentration of 0.269 mmol. To this mixture was added CTA (1.34 µmol, 0.375 mg) and AIBN (1.54 µmol, 0.254 mg). The final volume of the reaction solution was 600 µL. The mixture was transferred to a glass amber ampule and purged with nitrogen for 40 min. The ampule was flame sealed, and the reaction mixture was stirred at 50 °C for 48 h. The reaction mixture was cooled to room temperature, and the copolymer was subsequently purified by a Sephadex LH-20 column using methanol as an eluent to afford 27.2 mg (yield = 51%) of P-DTPA. The molecular weight analysis was performed using size exclusion chromatography (SEC-TDA) with an ACN/PBS (40:60) elution. The DTPA and FITC contents within the copolymer were characterized by ^{1}H-NMR and UV spectroscopy (absorbance at 494 nm) (203), respectively.

4.2.4 Selectivity studies

Selectivity studies were conducted in solutions containing endogenous metals to examine the impact of their presence on ^{177}Lu sequestration. A solution containing similar concentrations (1X) of biologically relevant metals (Zn^{+2}, Ca^{+2}, $Fe^{+2/+3}$, and Cu^{+2}) found in human serum (232) and another solution containing ten times (10X) these concentrations were prepared to conduct the selectivity studies. To prepare the 1X solution, $FeCl_2$ (51.06 µg), $FeCl_3$ (65.35 µg), $ZnCl_2$ (56.28 µg), $CaCl_2$ (8.3 mg), $NaHCO_3$ (1 mg), $CuSo_4$ (0.15 µg), Na_2HPO_4 (4.26 mg), and KCl (0.258 mg) were dissolved in 30 mL of PBS (pH = 7.4). The 10X solution was prepared analogously using ten-fold the endogenous metal content.

To carry out the DTPA selectivity studies, 190 µL of either the 1X or 10X biological metal solution described above were added in a microcentrifuge tube and preheated to 37 °C. To this solution was added $^{177}LuCl_3$ (5 µL in PBS) followed by the addition of DTPA (5 µL in PBS) to make a 2 or 20 µM solution. The final volume of the above solution was 200 µL and the concentration of ^{177}Lu was ≈ 6 nM (100,000 cpm / 50 µL). The mixture was heated to 37 °C. After 15 min a sample was withdrawn (6 µL), and the ^{177}Lu-DTPA complex was separated from the free ^{177}Lu by thin-layer chromatography (TLC) using an eluent mixture of water/methanol/NH_4OH (2:1:0.1). Under these conditions, the ^{177}Lu-DTPA complex migrates with the solvent front while the free ^{177}Lu remains at the origin point (233, 234). Autoradiographic images of the TLC plates were collected, analogous to our previous report (235), for $^{177}LuCl_3$ and ^{177}Lu-DTPA controls to confirm this behavior. To quantify the free ^{177}Lu vs. ^{177}Lu-DTPA, the TLC plate was cut into two halves, and the radioactivity in each half was recorded using a gamma counter. This study was performed in triplicate.

For the P-DTPA selectivity studies, 190 µL of either the 1X and 10X biological metal solutions described above were added to a microcentrifuge tube and preheated to 37 °C. To this solution was added $^{177}LuCl_3$ (5 µL in PBS) followed by the addition of P-DTPA (5 µL in PBS) to make a 2 or 20 µM (based on DTPA amount) solution. The final volume of the above solution was 200 µL and the concentration of the ^{177}Lu was ≈ 6 nM (100,000 cpm / 50 µL). After 15 min a 50 µL aliquot of the solution was withdrawn and analyzed. The ^{177}Lu-bound P-DTPA was separated from free ^{177}Lu using a desalting spin column following the manufacturer's protocol. Briefly, the excess liquid in the column was first removed (1,500 x g for 1 min). Then, the 50 µL sample aliquot described above was added to the center of compacted resin and centrifuged for 2 min at 1,500 x g. The radioactivity remaining in the column (free ^{177}Lu) or eluted (^{177}Lu-bound P-DTPA) was measured using a gamma counter. This study was done in duplicate.

4.2.5 Chelation in human serum

The efficacy of DTPA and P-DTPA to sequester $^{177}LuCl_3$ in human serum was examined. To 195 µL of human serum was added the desired amount of DTPA dissolved in PBS (5 µL) to achieve a 20 µM (based on DTPA content) solution. The mixture was preheated to 37 °C. To this mixture was added 350 µCi (≈ 488 nM) of $^{177}LuCl_3$ (2.5 µL in DI water). After 15 min, a 100 µL aliquot was analyzed by radio-HPLC (equipped with an analytical Proteo C_{12} column) using isocratic separation (95% DI water in ACN) with a flow rate of 1.5 mL/min. The percentage of the bound ^{177}Lu-DTPA complex in solution was determined by the integration of the associated peak relative to the unchelated ^{177}Lu peak. Similarly, the chelation of ^{177}Lu by P-DTPA in human serum was examined at 20 µM, based on the content of DTPA. After 15 min, a 100 µL aliquot was analyzed by radio-SEC (equipped Shodex Asahipak GF-510 HQ GPC column) using ACN/PBS (40:60) elution with a flow rate of 0.6/mL to collect the fraction of ^{177}Lu-P-DTPA. The radioactivity in the collected fraction was measured using a dose calibrator. The radioacitivity in the collected fraction was divided by the total injected radioacitivity (to the radio-SEC) to estimate the chelated ^{177}Lu.

4.2.6 Stability of ^{177}Lu-P-DTPA in human serum

To examine the stability of the ^{177}Lu-bound P-DTPA in human serum, P-DTPA was first radiolabeled with $^{177}LuCl_3$ and purifed. Briefly, 500 µCi of $^{177}LuCl_3$ was added to a solution containing 100 µg of P-DTPA in 50 µL DI water and heated to 37 °C for 30 min. The ^{177}Lu-P-DTPA was purified by the radio-SEC system following the previously described conditions. Once purified, ^{177}Lu-P-DTPA (200 µCi) was added to 500 µL of human serum and heated at 37 °C for 144 h. Aliquots were withdrawn and analyzed using a desalting spin column, as previously described, followed by injection into the radio-HPLC to evaluate the ^{177}Lu-bound to P-DTPA or serum proteins. Another sample was withdrawn, diluted in PBS to obtain 100,000 cpm /50 µL, and desalted using a spin column. The eluted and column-associated radioactivity was counted, as described previously, to estimate the ^{177}Lu in unbound form.

4.2.7 Cell viability

Cell viability studies using human umbilical vein endothelial cells (HUVEC) were performed for DTPA and P-DTPA at concentrations ranging from 31.25 to 1000 µM. The cells were seeded in 96-well plates at a density of 3000 cells (100 µL) per well. After 24 h, the media was replaced with fresh media-containing the desired concentration of DTPA or P-DTPA and incubated at 37 °C. After 48 h, the media was aspirated out and fresh media containing the PrestoBlue® reagent (10% by volume) was added and incubated at 37 °C for 1 h. The fluorescence measurements were then recorded using a plate reader (excitation: 560 nm and emission: 590 nm). A one-binding site model using Graphpad Prism 7 (U.S.) was employed to determine the IC_{50} values.

4.2.8 Cell culture

Human umbilical vein endothelial cells (HUVEC) (ATTC, U.S.) were cultured in F-12K medium containing heparin (0.1 mg/mL), endothelial cell growth supplement (0.2 mg/mL), FBS (1mL / 10 mL), L-glutamine (2 mM), and sodium bicarbonate (1500 mg/L) at 37 °C in a humidified environment of 5% CO_2.

4.2.9 *In vivo* prophylactic studies

All animal protocols conformed to the Guide for the Care and Use of Laboratory Animals of the National Institutes of Health and were approved by the Institutional Animal Care and Use Committee (IACUC) at the University of Nebraska Medical Center. The mice used in the studies were female CF-1 mice (Charles River Laboratories, U.S.) weighing ~ 27 g. They were housed in a room with a controlled temperature (~ 22 ºC) and a 12-h light cycle. A total of 30 mice were randomly allocated into two arms (15 mice per arm) based on the prophylactic chelator administration time (either 6- or 24-hr) and post-contamination with $^{177}LuC_3$. In each arm, 15 mice were randomized into three groups (five mice per group) to receive either no chelator treatment, DTPA (30 µmol/kg), or P-DTPA (30 µmol/kg based on the DTPA content). After 6 or 24 hr,

$^{177}LuCl_3$ (20 μCi per mouse) in 100 μL of PBS was administered intravenously via the tail vein. The mice were singly-housed, and the bedding material was collected and replaced every other day (a total of six collections over the course of the study). The radioactive content of the bedding materials was analyzed to examine the excretion/clearance of ^{177}Lu over time. At 14 – 15 days post-administration of the ^{177}Lu, biodistribution studies were conducted by sacrificing the mice, excising, and determining the mass of select tissues and measuring the associated radioactivity for each. From this data, percent injected dose (%ID) or %ID/gram of tissue (%ID/g) could be determined.

4.2.10 Statistical analysis

Data is presented as mean ± standard deviation (SD). GraphPad Prism version 7.0 (GraphPad Software Inc., U.S.) was used to perform the Student's *t*-test (two groups) or one-way ANOVA with Bonferroni post-tests (> two groups). A *p*-value of less than 0.05 was considered significant.

4.3 Results and discussion

Upon the unintended or deliberate release of actinides into the environment, internal contamination by actinides will results in the retention of the radionuclides in vital organs, mainly the liver and skeleton, leading to acute and long-term radiotoxicity (134). Chelation therapy with DTPA is currently the only FDA-approved therapy to remove select actinides from the body (219). DTPA is a small, hydrophilic molecule capable of rapidly distributing to the extracellular tissue compartments and chelating actinides to facilitate their removal from the body. However, the efficacy of this decorporation therapy is highly dependent on the lag time between exposure to the actinide contaminate and the administration of chelation therapy. Prompt administration of the chelators is necessary to ensure efficient decorporation and, as a result, better therapeutic outcomes are achieved when compared to delayed treatments (236). In situations of mass population exposure

to actinides or when prompt and in-depth medical treatment may not be viable, a prophylactic chelation therapy would be valuable to mitigate risks to individuals with the potential of exposure. Unfortunately, the rapid plasma clearance of DTPA, with a half-life measured in minutes, does not readily lend itself to prophylactic applications (140, 237).

Similar to other innovative reports (144, 223-225), we seek to explore if nanomedicine constructs can be utilized to increase the circulation time and prophylactic action of chelation therapies and reduce the irreversible deposition of actinides in the body. HPMA copolymers have been widely investigated in preclinical studies and several promising constructs have entered into clinical trials (100). The molecular weight of these copolymers can be adjusted to increase plasma retention from hours to days, with increased molecular weight promoting longer circulation times (107, 228). The molecular weight of the copolymers also impacts the primary clearance pathway with copolymers below approximately 45 kDa clearing via renal excretion and copolymers above this threshold clearing predominately through the hepatobiliary system. With this in mind, DTPA was incorporated into a HPMA copolymer (P-DTPA, 33.9 kDa) with a molecular weight that would allow for adequate plasma retention (days) but still predominately clear renally. Using this P-DTPA copolymer, we hypothesized that the enhanced plasma retention of this construct would increase the prophylactic decorporation efficacy relative to DTPA treatment.

4.3.1 Synthesis and characterization of P-DTPA

The DTPA chelation moiety was incorporated into the polymeric construct by initially synthesizing the APMA-DTPA monomer. This was accomplished by using p-SCN-Bn-DTPA, a common bifunctional chelator that allows for a chemo-selective conjugation to amine functional groups within molecules (238) while still retaining all eight coordination sites present in DTPA that are needed to strongly chelate metals. p-SCN-Bn-DTPA was conjugated with the primary amine of the APMA monomer via a thiourea linkage yielding the desired APMA-DTPA monomer (Figure 4.1A). Characterizations of APMA-DTPA included ^{1}H-NMR and mass spectrometry, as shown in

Figure 4.1A. With the HPMA, APMA-FITC (168) and APMA-DTPA monomers in hand, the copolymeric construct was synthesized using RAFT polymerization. HPMA copolymers with molecular weights greater than 45 kDa are unable to efficiently be cleared by the renal systems resulting in extensive blood circulation times and clearance primarily by the hepatobiliary system (97, 228). To avoid hepatobiliary clearance, an HPMA copolymer molecular weight of less than 45 kDa was targeted to allow efficient renal clearance of the polymeric decorporation agent while also allowing sufficient blood circulation times (i.e., days). The polymerization yielded the desired DTPA-incorporated polymeric construct (P-DTPA, Figure 4.1B) with a molecular weight of 33.9 kDa and a narrow dispersity (Đ = 1.09) as given in Table 4.1. The DTPA content was calculated based on ^{1}H-NMR and yielded a value of 5.2 mol% which translates to an average of 10.2 DTPA units per polymer chain (Table 4.1).

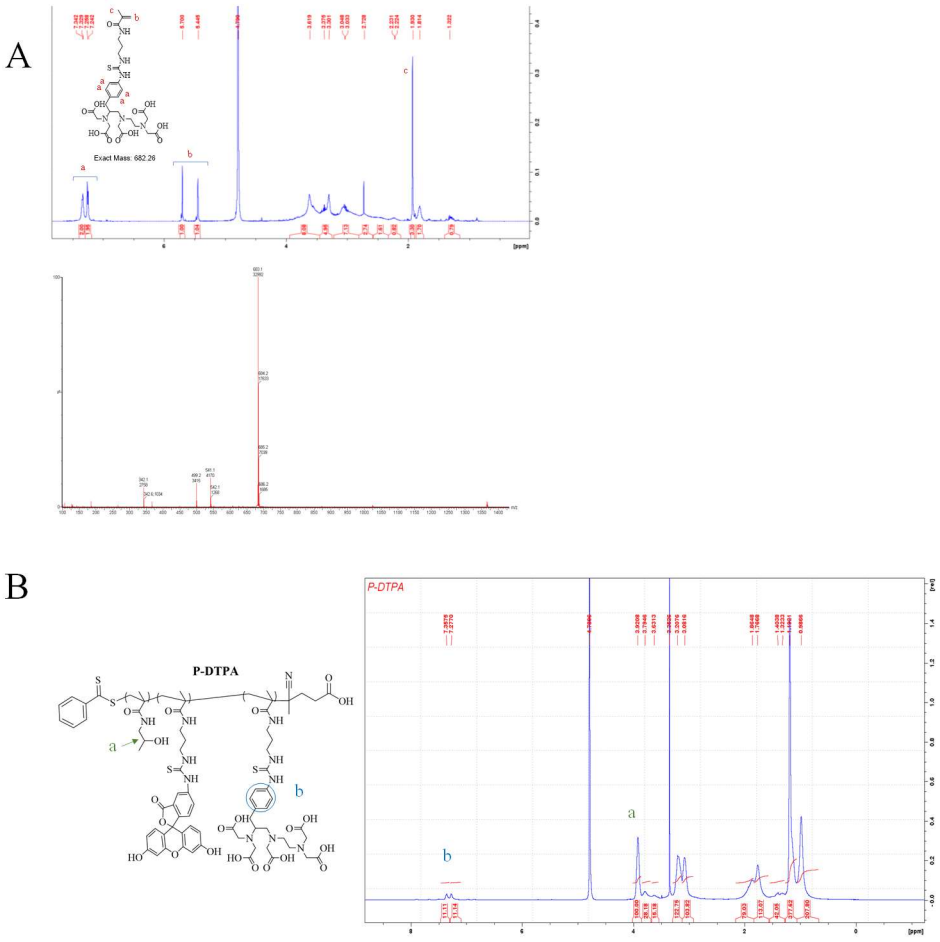

Figure 4.1 ^{1}H-NMR (in D_2O)and MS spectra of APMA-DTPA (A) and ^{1}H-NMR spectrum of P-DTPA (in D_2O) (B).

Table 4.1 Characteristics of P-DTPA

	P-DTPA
Estimated MW (kDa)[a]	33.9
Đ[a]	1.09
Rh (nm)	4.23
DTPA content (mol%)[b]	5.2
FITC content (mol%)[c]	0.5

[a]As determined by SEC-TDA system

[b]As estimated by ^{1}H-NMR

[c] Based on UV/visible spectrometric analysis

4.3.2 Selectivity studies of DTPA and P-DTPA

Previous investigations of DTPA have explored the impact other competing metals in solution can have on the sequestration efficacy of the chelator for ^{177}Lu (233, 239). From these studies, it was found that the identity of the metal and its relative concentration to the ^{177}Lu played the greatest role in impacting chelation efficacy. For example, in one study, substantial decreases in ^{177}Lu chelation yields were observed when the ratio of $Fe^{2+}/^{177}Lu^{3+}$ and $Zn^{2+}/^{177}Lu^{3+}$ increased above 1 and 10, respectively (233). However, no change in DTPA chelation efficacy for ^{177}Lu was observed when Ca^{2+} was added at concentrations up to100-fold equivalent excess. In order to examine how endogenous biologically relevant metals might interfere with the chelation of ^{177}Lu, selectivity studies were performed with DTPA and P-DTPA in the presence of competing metals Na^{+}, K^{+}, Mg^{2+}, Ca^{2+}, Zn^{+2}, $Fe^{2+/+3}$ and Cu^{+}.

For the selectivity studies, two solutions were prepared. The first solution (1X) contains concentrations of the above mentioned metals at levels commonly found in human blood (232). The second solution (10X) was prepared in based on metal concentrations that were 10-fold higher than the 1X solution. In each of these solutions, 2 or 20 μM of DTPA and P-DTPA (based on the DTPA content) was incubated with 6 nM of $^{177}LuCl_3$. For the DTPA selectivity studies, the analysis of the chelation efficacy was monitored by radio-TLC which separated the remaining free ^{177}Lu (remains at the origin) from the ^{177}Lu-DTPA (moves with the solvent front). With respect to the P-DTPA copolymer, the chelation efficacy was determined using a spin desalting column (7 kDa) to separate free ^{177}Lu from ^{177}Lu-bound to the copolymer. The results of these studies are given in Figure 4.2.

For the selectivity studies utilizing DTPA, the 20 μM concentration of the chelator gave a complexation yield of 93.0 ± 2.0% in the 1X solution but fell to 36.2 ± 7.2% in the 10X solution. This observation agrees well with previously reported literature in which increasing competitive metal concentrations was inversely related to complexation yields of ^{177}Lu (233). In contrast, the

complexation yields of ^{177}Lu by P-DTPA showed no change between the 1X (79.1 ± 2.0%) and 10X (76.8 ± 0.6%) at the 20 μM concentration (based on DTPA content of the copolymer). At a 2 μM concentration of DTPA, the ^{177}Lu complexation yield was 21.5 ± 3.5% in the 1X solution and was reduced over 13-fold to 1.6 ± 0.3% in the 10X solution. Similarly, the complexation yield at 2 μM of P-DTPA for ^{177}Lu was 43.0 ± 1.2% in the 1X solution but showed a more modest 4.9-fold reduction to 8.7 ± 0.7% in the 10X solution.

These results indicate that DTPA is the better chelator at higher concentrations but is substantively poorer at chelating ^{177}Lu at lower concentrations or when it is in the presence of higher competitive metal concentrations. In contrast, P-DTPA demonstrated chelation efficacies that were significantly better at lower concentrations and were not as detrimentally impacted when higher competitive metal concentrations were present. One possible explanation for these observations is the fact that different chelators were employed. The chelator of P-DTPA utilizes the p-SCN-Bn-DTPA derivative. Compared to the parent DTPA, the introduction of a rigid benzene ring has been shown to not only increase the kinetic stability of the metal-DTPA complex (238, 240, 241) but also to enhance its complexation kinetics (221). Additionally, we postulate that steric shielding might also play a role in the increased chelation efficacy of the P-DTPA. After thermodynamically favorable chelation of ^{177}Lu is achieved by P-DTPA, the increased steric bulk of the copolymer may impede transchelation thereby increasing the kinetic stability of the complex.

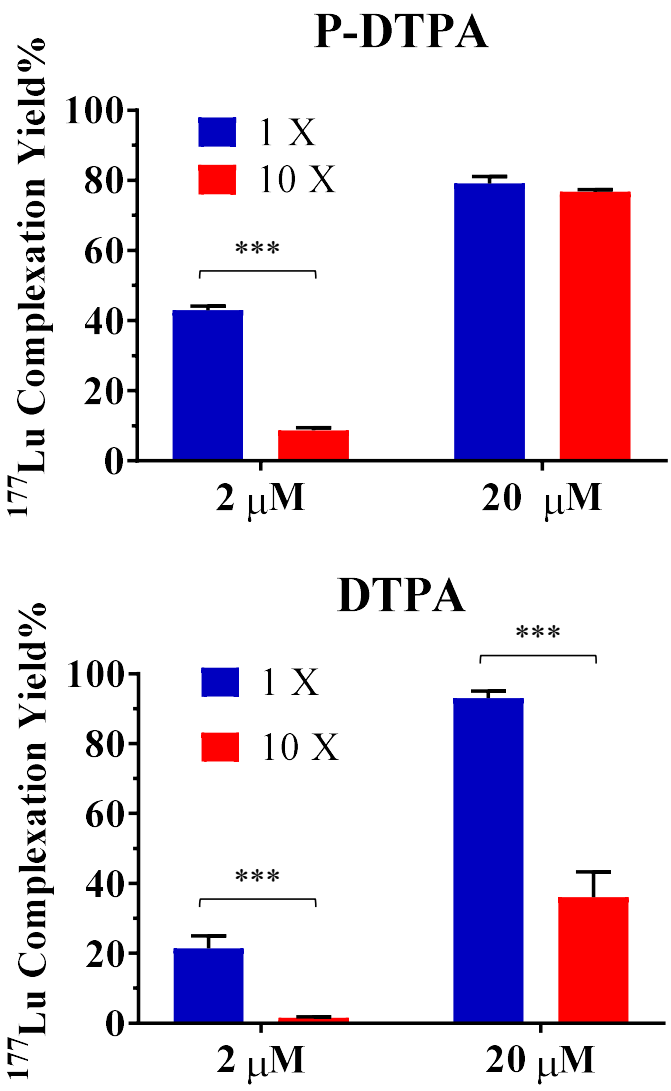

Figure 4.2 Selectivity study profiles of DTPA and P-DTPA after 15 mins incubation with 1X and 10X solutions containing ^{177}LuCl3. Values represent mean ± SD.

4.3.3 Chelation and stability in human serum

An *in vitro* chelation study was performed to evaluate the ability of DTPA and P-DTPA to sequester free ^{177}Lu in human serum. The study was conducted at equivalent 20 μM DTPA and P-DTPA (based on total DTPA content for the polymer) concentrations in the presence of 350 μCi (488 nM) of $^{177}LuCl_3$ at 37°C. After 15 min, the complexation yields were 94.2 ± 2.5 and 50.0 ± 0.3 for DTPA and P-DTPA, respectively. This observation is in agreement with the results from the selectivity studies using the 1X formulation in which the DTPA exhibited a higher sequestration efficacy than P-DTPA at this concentration (233, 239).

Once chelated to the radiometal, a decorporation agent is expected to exhibit minimal transchelation and maintain complexation until eliminated from the body. To examine the ability of P-DTPA to maintain stable complexes to ^{177}Lu, the *in vitro* stability of ^{177}Lu-labeled P-DTPA was examined in human serum at 37°C for six days (144 h). Analysis of the stability of the ^{177}Lu-labeled polymeric complex was conducted by employing a desalting spin column to segregate large from small molecular weight molecules in the serum. The large molecular weight fractions were subsequently analyzed by radio-SEC analysis. Radiometric analysis of the low- and high-molecular weight fractions shows that 12% of ^{177}Lu was released from P-DTPA. These results indicate there is a limited release of the ^{177}Lu from the chelator over an extended time, which is in agreement with previously published reports (242, 243).

4.3.4 Cytotoxicity

The HUVEC cell line is commonly used for investigating the cytotoxicity of nanomedicines due to prolonged exposure (i.e., long blood circulation times) of the nanomedicine constructs with the vasculature (244). The HUVEC cells were exposed to DTPA and P-DTPA (based on DTPA content) concentrations ranging from 31.25 to 1000 μM for 48 h and evaluated for viability using a commercial fluorescence assay. Up to 125 μM, the DTPA and p-DTPA demonstrated no statistically significant differences in cellular viability (Error! Reference source

not found.). At concentrations of 250 μM, a statistically significant 15% decline in cellular viability was observed for the P-DTPA relative to DTPA ($p < 0.001$). For the P-DTPA, declines in cellular viability continued as the concentration of the polymeric construct increased resulting in a minimal cellular viability of 28% at the highest (1 mM) concentration. A statistically significant 25% decline relative to the untreated controls ($p < 0.01$) was observed for the DTPA at the 1 mM concentration.

The cytotoxicity of DTPA has been demonstrated to be due to interference with cellular proteins and DNA synthetic pathways (245). The cytotoxicity of the P-DTPA may also be due, in part, to the presence of DTPA units within the copolymer. However, the P-DTPA also contains a diothiobenzoate functional group on one of the termini of the copolymer. It has been demonstrated that the diothiobenzoate terminal end of HPMA copolymers can cause cytotoxicity at elevated (> 200 μM) concentrations (incubated for 24 h) (246). Based on our data, the calculated IC_{50} after 48 h P-DTPA incubation was 371 ± 45 μM (based on the DTPA concentration that is approximately 10 folds higher than the concentration of diothiobenzoate within P-DTPA). The higher observed cytotoxicity using P-DTPA may also be attributed the presence of the diothiobenzoate within the copolymer. In practice, chelation therapy using DTPA is commonly administered at i.v. doses of 30 μmol / kg (134, 220, 247). The administration of the copolymer at doses equivalent to this DTPA concentration would result in a 650 μM concentration of the copolymer in the plasma, but this concentration would be short-lived (< 1 h) with the copolymer rapidly distributing to other tissue compartments as well as being renally excreted (97, 248). Therefore, despite the higher observed cytotoxicity of P-DTPA compared to DTPA, these results indicate that the P-DTPA would likely be well tolerated at the proposed prophylactic administration dose (30 μmol / kg based on DTPA content).

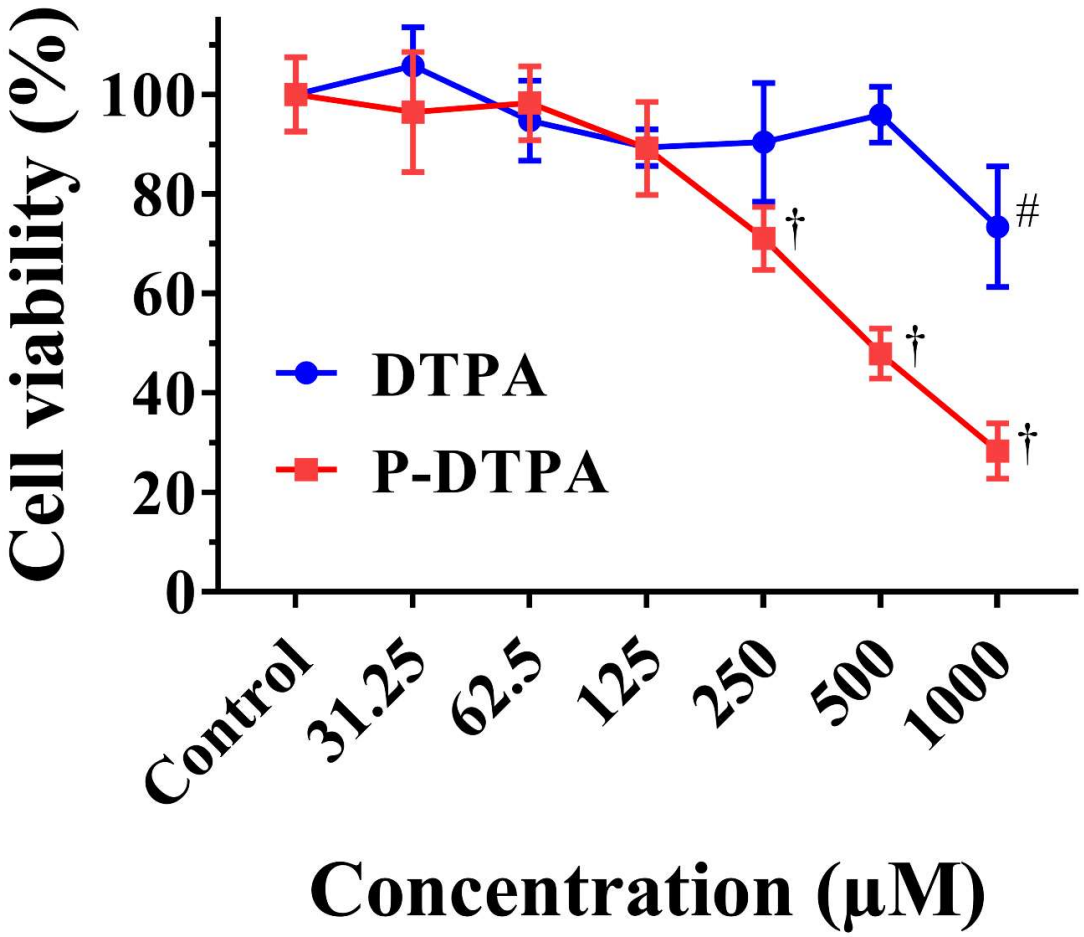

Figure 4.3 Cell viability profiles of DTPA and P-DTPA after two days incubation with HUVEC cell line. # and † indicate significance at $p < 0.001$ compared to the control (no chelator treatment). Values represent mean ± SD.

4.3.5 *In vivo* prophylactic studies

To examine the prophylactic capabilities of P-DTPA and DTPA, the decorporation agents were administered at 6 and 24 h prior to the administration of the ^{177}Lu contaminate (timepoint = 0 day) (Figure 4.4A). These time points were chosen in order to observe if there was a time-dependent effect on prophylactic administration and decorporation efficacy. Each 6 or 24 h prophylactic arm includes an untreated control, DTPA (30 μmol/kg), or P-DTPA (30 μmol/kg based on the DTPA content) groups. The excretion of the radioactivity was monitored over 14 – 15 days by radiometric analysis of the bedding material every other day and is represented by an overall %ID excretion format illustrated in Figure 4.4C. The enhanced excretion of the ^{177}Lu contaminate over time in the DTPA and P-DTPA groups relative to the untreated control group can be visualized in Figure 4.4B**Error! Reference source not found.**. Finally, at the end of the decorporation experiments, the mice were sacrificed to examine the differences in the ^{177}Lu tissue deposition between study arms (6 and 24 h) and groups (untreated control, DTPA, and P-DTPA) (Figure 4.5).

Examination of the rate of excretion over time (Figure 4.4B and C) revealed that DTPA and P-DTPA enhanced the decorporation of ^{177}Lu in both prophylactic arms. For the 6 h prophylactic arm, analysis of excretion relative to the control demonstrated that DTPA and P-DTPA had a maximal decorporation enhancement at day 4 with a respective 3.8- and 4.5-fold increase in clearance relative to the untreated control group. From that point, the decorporation enhancement for the DTPA group gradually declined, but was statistically higher than the control, until day 10. Conversely, for the P-DTPA group, a greater than 3-fold enhancement in clearance relative to the control was observed in the remaining time points of the study. At the end of the 14 day study for the 6-h prophylactic treatment arm, the P-DTPA and DTPA groups decorporated 56.4 ± 3.1 and 43.4 ± 2.0 %ID, respectively, relative to 20.6 ± 1.6 %ID for the untreated control.

For the 24 h prophylactic arm, the enhancement in decorporation for the DTPA and P-DTPA groups was more modest. DTPA enhancement of ^{177}Lu clearance plateaued at a value 1.7 to

1.8-fold greater than the control but, similarly to the 6 h arm, by day 10 had a comparable excretion rate as the control. For the P-DTPA group, with the exception of day 2, all time points demonstrated a greater than 2-fold increase in ^{177}Lu clearance relative to the control. At the conclusion of the 15 day study for the 24 h prophylactic arm, 45.4 ± 1.9, 32.7 ± 2.7, and 23.6 ± 1.4 %ID of the ^{177}Lu had decorporated from the mice for the P-DTPA, DTPA, and untreated control groups, respectively. As expected, the 6 h prophylactic treatment arm demonstrated significantly higher rates of excretion relative to the 24 h arm. This is almost certainly due to the higher concentration of the decorporation agents in the plasma and tissue compartments improving sequestration efficacy in the 6 h prophylactic treatment arm compared to the 24 h arm.

The capability of DTPA to enhance the decorporation of ^{177}Lu in the 6 and 24 h prophylactic treatment groups is, at first glance, surprising given its relative rapid plasma clearance. However, a small but significant amount of DTPA is known to be retained in intracellular reservoirs within tissues (249). Through slow externalization of the DTPA decorporation agent and chelation of internalized ^{177}Lu, the DTPA is able to substantially increase decorporation relative to the untreated control group. Similar results were reported by Grémy and co-workers when examining the plutonium and americium decorportation efficacy of DTPA (249). In contrast to DTPA, polymer conjugates such as P-DTPA can circulate in the blood for many hours to days. Previous studies of HPMA copolymers of similar molecular weights to P-DTPA demonstrated that these copolymers circulate in the blood for more than 24 h (107, 248, 250-252). For example, a study reported that after i.v. injection in tumor-bearing mice, an HPMA copolymer (MW = 35.7 kDa) modified with five DTPA units per chain showed a rapid reduction of blood levels from 7% (%ID/g) to nearly 3% after 6 h, followed by a slower reduction over 48 h to 1% (248). Similar to DTPA, nanomedicine constructs, such as P-DTPA, are known to be substantially internalized, particularly by hepatocytes and immune cells composing the mononuclear phagocyte system (253). These nanomedicine platforms can enter cells through a number of mechanisms and are most

predominately trafficked to the endolysosomal compartments of the cell (254). Coincidently, this is also the predominant subcellular storage site for several known actinides (i.e., plutonium and americium) (255-257). The selective trafficking, concentration and colocalization of drug delivery systems and actinides into these cellular compartments may give the nanoconstruct an advantage with regard to intracellular decorporation. Taking the above into account, the more effective decorporation rates of the P-DTPA relative to DTPA over the course of these studies is likely due to improvements in both extracellular and intracellular chelation of the ^{177}Lu. Additionally, the more prolonged clearance of the ^{177}Lu for the P-DTPA groups is likely reflective of the slower release from tissue compartments and the inherently longer circulation time of the polymeric decorporation agent.

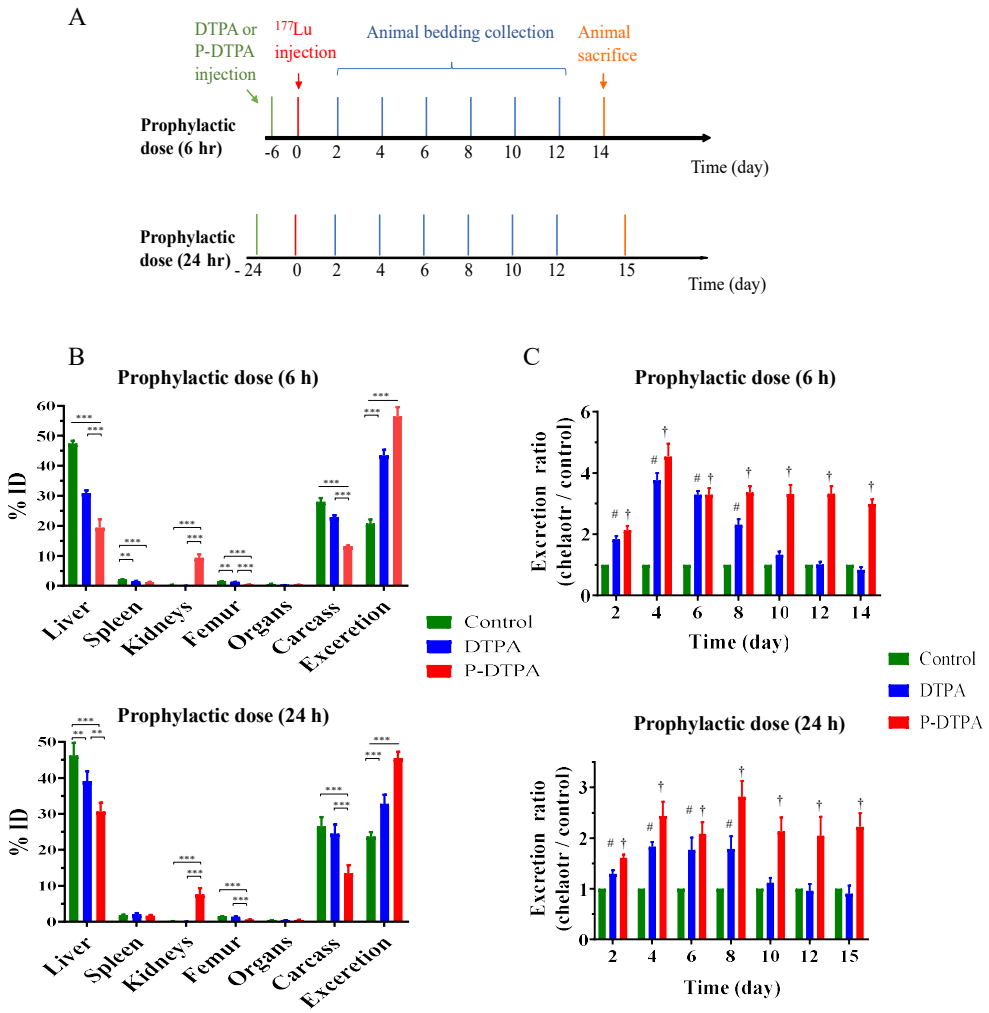

Figure 4.4 Schematic representation of *in vivo* studies and the excretion profiles. In the schematic representation for the timelines for the two arms of *in vivo* studies (A), the top and bottom timelines represent the 6 h- and 24 h-arms, respectively. In the excretion ratios (B) of ^{177}Lu for the DTPA and P-DTPA to the control, the average of % ID excreted per interval for the control (no chelator) is normalized to give a value of 1.0. # and † indicate significance at $p < 0.001$ compared to the control (no chelator treatment). Cumulative excretion of ^{177}Lu over 14-15 days (C). Values represent mean ± SD (n = 5).

At the end of the study, the mice were sacrificed and underwent a biodistribution study to examine the remaining ^{177}Lu tissue deposition (Figure 4.5). Excluding the liver, spleen, kidneys, and femur (skeleton), the total radioactivity (%ID) retained in the internal organs was minimal (< 1 %ID) for all the groups. The femur was used as a proxy for measuring skeletal uptake. The majority of the radioactivity remaining in the carcass after tissue excision is almost certainly due to the known skeletal adsorption of free ^{177}Lu (258, 259). As expected, for all treatment arms, the liver and skeleton were the major sites of ^{177}Lu deposition (258-260). In the 6 h prophylactic treatment arm, P-DTPA and DTPA reduced liver retention to 19.3 ± 3.0 and 30.8 ± 1.1 %ID, respectively, compared to 47.2 ± 1.1 %ID for the untreated control group. Likewise for the femur, P-DTPA and DTPA reduced femur deposition to 0.50 ± 0.04 and 1.27 ± 0.10 %ID, respectively, relative to 1.47 ± 0.07 %ID for the untreated control group. Similar tissue deposition reductions were observed in the carcass values which is attributed primarily to the remaining skeletal activity. For the 24 h prophylactic treatment arm, a similar pattern was observed with the exception of a diminished liver decorporation efficacy for the experimental groups. The P-DTPA and DTPA groups reduced liver retention to 30.6 ± 2.6 and 39.0 ± 2.9 %ID, respectively, relative to 46.1 ± 3.8 %ID for the untreated control. Interestingly, femur decorporation with P-DTPA and DTPA in the 24 h arm provided statistically identical decorporation amounts compared to the 6 h arm, suggesting, at least in this study's timeframe, that the skeletal decorporation was not impacted by the increased timeframe of prophylactic administration.

One detriment to the utilization of the P-DTPA as a decorporation agent was the substantial increase in kidney uptake and retention. For both prophylactic treatment arms, renal uptake for the untreated control or DTPA groups was minimal (≤ 0.2 %ID) with no significant difference (p > 0.05) amongst the groups. However, in 6 and 24 h study arms, the P-DTPA group exhibited a substantially higher renal retention of 9.3 ± 1.2 and 7.6 ± 1.8 %ID, respectively ($p < 0.001$ compared to the control and DTPA groups). This increased renal uptake is likely attributable to the

anionic charge of the copolymer due to the incorporation of the DTPA moieties. Previous reports of polymers modified with anionic functional groups (e.g., methacrylic acid) indicate that this can substantially increase the renal uptake primarily due to increased recognition and internalization by the proximal tubule cells of the kidney (107, 261, 262). Modification of the copolymer to reduce the net anionic charge or the incorporation of metabolizable linkers to increase renal clearance may be approaches that could help ameliorate this renal uptake in future optimization studies.

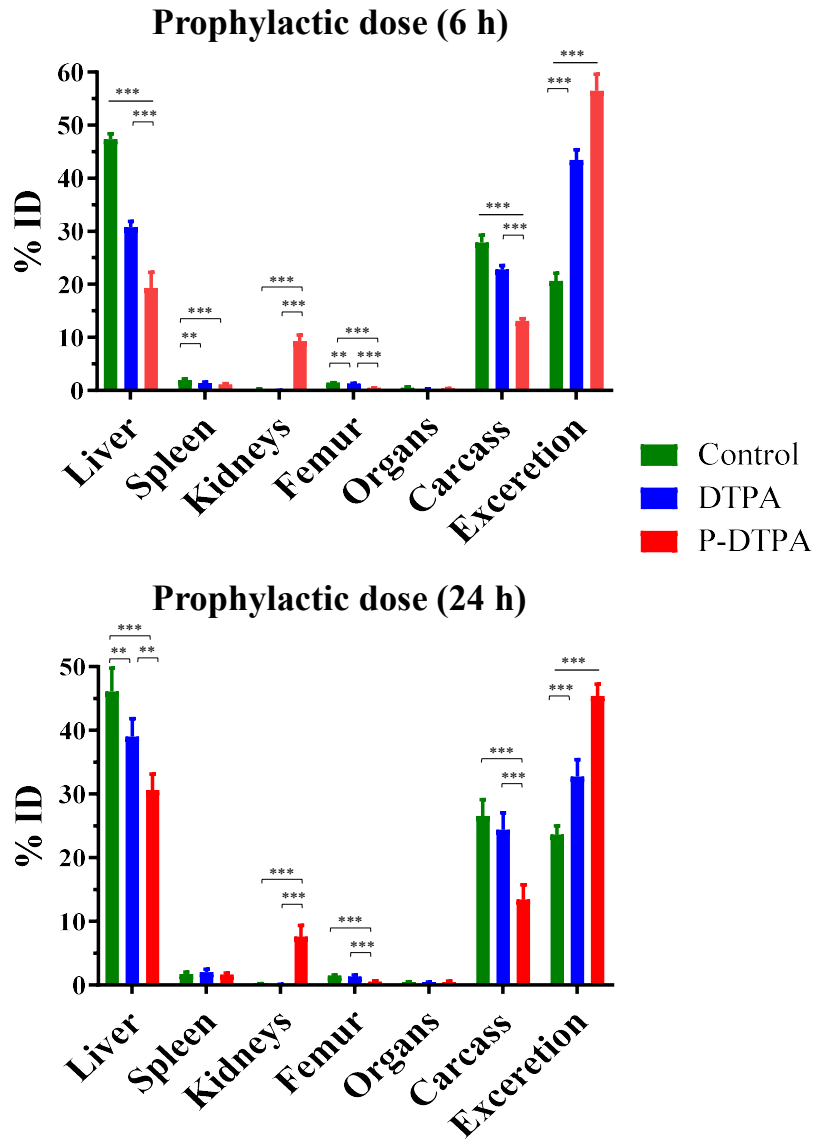

Figure 4.5 Total ^{177}Lu body content and distribution after 14 and 15 days of ^{177}Lu contamination for the 6-h and 24-h prophylactic treatments, respectively. Organs represent combined data from heart, lungs, pancreas, stomach, small and large intestines, brain, and an average of 0.60 g of muscle tissues. * $p < 0.05$, ** $p < 0.01$, *** $p < 0.001$. Values represent mean ± SD (n = 5).

4.4 Conclusion

In this study, a DTPA-incorporated HPMA copolymer was synthesized and its potential as a prophylactic decorporation agent against radiometal deposition was examined relative to DTPA. The P-DTPA demonstrated chelation efficacies that were better than DTPA at lower concentration of the decorporation agent. In addition, the chelation efficacy of P-DTPA was not as negatively impacted by the presence of competitive metals as was DTPA. The P-DTPA demonstrated good chelation efficacy to ^{177}Lu and chelate stability in human serum. Cytotoxicity studies revealed that the P-DTPA copolymer exhibited toxicity only at concentration ranges exceeding 200 μM and was determined to be viable for *in vivo* examination. The *in vivo* decorporation studies in mice showed a greater decorporation effect for P-DTPA compared to the FDA-approved DTPA in the context of prophylactic treatment. These results are promising and represent a proof of concept that justifies the further development of DTPA-incorporated HPMA copolymers as prophylactic decorporation agents.

5 Chapter 5. Summary and future directions

5.1 Summary

Depending on the type, polymeric drug delivery systems can be easily multifunctional. They can be designed to carry radionuclides, targeting ligands, chemotherapeutic drugs, and other agents. In this dissertation, we aimed to explore the advantages that the HPMA copolymer offers using various strategies to improve cancer therapy and radionuclide corporation.

Radiolabeled bombesin (BBN) peptide analogs are widely evaluated in preclinical and clinical trials for prostate cancer imaging and therapy due to their nanomolar affinity for GRPR, which is overexpressed in prostate cancer. One of the main drawbacks of using receptor-targeted peptides for therapy is their short tumor residence time due to intrinsically high diffusion and efflux rates. On the contrary, large polymeric systems (e.g., HPMA copolymers) can retain for an extended time, exploiting the tumor tissues' lack of drainage. Inspired by the need for targeted polymeric delivery systems to improve prostate cancer radiotherapy, we developed BBN-modified HPMA copolymers. The synthesized BBN peptide analogs included charged residues (arginine or glutamic acid) to improve their solubility because the majority of amino acids in the active moiety of BBN peptide analogs are hydrophobic. The introduction of charged residues decreases the self-assembly of hydrophobic peptides within the polymeric delivery systems (216). To test the effect of the peptide and charge content of the BBN-HPMA copolymers, we varied the peptide type and content on the HPMA copolymers to afford four positive, four negative, and two zwitterionic BBN-HPMA copolymers. Only the positive copolymers showed high GRPR-based uptake, with internalization percentages ranging from 0.7 to 20% over 4 h. The blocking experiment study using BBN peptide antagonist confirmed this finding. These positive BBN-HPMA copolymers were then evaluated in a normal (CF-1) mouse model to evaluate the immune response. Unfortunately, the majority of the injected dose of these positive copolymers (except the copolymer with the lowest

BBN content) were found in the liver and spleen after only 4 h of administration, indicating rapid recognition by the immune cells. These results show the need for further optimization to the current design.

The field of *in vivo* bioorthogonal reaction via IEDDA has been an active research area in the past ten years. This chemistry was extensively explored to improve the safety profiles of radiolabeled antibodies. Due to their large sizes relative to small molecules and targeted peptides, antibodies circulate long times (e.g., few days) before they are eliminated from the blood and retain high tumor to non-target ratios. Using the *in vivo* bioorthogonal chemistry via IEDAA, TCO-tagged antibodies are first injected and allowed to accumulate in the tumor tissues and cleared from the circulation. Then, a radiolabeled TZ probe is injected. This probe has high specificity and affinity to react with TCO, which is presumably found in the tumor tissues tagged to the antibody. The probe usually has a very short plasma half-life (several minutes). Therefore, any unreacted TZ probe is quickly cleared from the body. The TZ probe that reacted with the TCO-tagged antibody at the tumor tissues will reside for long times. We wanted to explore this strategy using HPMA copolymer because of its attractive properties over antibodies (e.g., multifunctionality and capacity to carry folds higher of TCO units). TCO-tagged copolymer's molecular weight (≈ 110 kDa) was larger than the renal threshold because we wanted this copolymer to circulate for an extended time to allow high tumor accumulation. The copolymer was synthesized to exploit the abundant cathepsin S enzyme in MPS-associated tissues (e.g., liver and spleen). The copolymer was synthesized by extension of small molecular weight HPMA copolymers (≈ 20 kDa) with a linker cleaved by cathepsin S enzyme. The *in vitro* cathepsin S enzyme study showed that this copolymer could be cleaved by the enzyme into smaller fragments.

The reaction kinetics were evaluated between the TCO-HPMA copolymer and two different types of TZ probes. The optimized TZ probe (DOTA-TZ 2) was used for the *in vivo* analysis. Relative to a non-cleavable TCO-HPMA copolymer (NP-82-TCO-C) having a similar

molecular size, the cleavable TCO-HPMA copolymer (MP-90-TCO-C) was cleared from the blood, liver, and spleen at a faster rate in a normal mouse model, indicating that this copolymer was likely biodegraded by cathepsin S enzyme. This copolymer failed to show a significant difference relative to the non-cleavable copolymer in immunocompromised ovarian cancer mouse models (NOD and SCID), indicating the major role of normal immunity. The *in vivo* TCO / TZ chemistry was achieved for the non-cleavable and cleavable copolymers at the tumor tissues, but most TZ probe signal was found in the blood (in both NOD and SCID models). This issue made us investigate the utility of a masking agent (dextran modified with TZ), which was previously shown to deactivate the residual TCO in the blood without a significant effect on TCO in the tumor tissues. This masking agent was injected 30 min before injecting the TZ probe. We found a huge reduction in the TZ probe signal from mainly the blood. The tumor / non-target ratio was higher than one for all the non-target tissues (except kidneys). These results show the feasibility of the *in vivo* TCO/TZ bioorthogonal chemistry approach.

The release of actinides in case of an accident is a major public health concern. Internal contamination via inhalation ingestion or through wounds can lead to their retentions in the liver and skeleton for years, which leads to long term exposure. The lag time between internal contamination and starting chelation therapy is crucial for effective therapy. Delaying the chelation therapy leads to poor decorporation results. The currently approved chelation therapy is based on DTPA. It has a short half-life (< 2 h), which does not render itself a good candidate for prophylactic application. We aimed to develop a DTPA-modified HPMA copolymer (P-DTPA) that can circulate for hours to a few days to address this issue. Our *in vitro* analysis showed P-DTPA's ability to chelate the actinide model even in the presence of biological competing metals at concentrations that are ten folds higher than their serum concentrations. We also found that P-DTPA has superior decorporation efficacy in a mouse model when compared head to head with DTPA. We found that P-DTPA increased the actinide model's excretion (^{177}Lu) over two weeks of monitoring when

administered 6- and 24-h before contamination with ^{177}Lu. However, we found higher retention of ^{177}Lu in the kidneys of mice injected with P-DTPA. A similar issue was reported previously using radiolabeled negatively charged polymers. Such polymers can retain in the proximal tubes of kidneys for days to a few weeks. Overall, P-DTPA showed enhanced decorporation and proved to be feasible for prophylactic applications.

5.2 Future directions

5.2.1 Charge-switch BBN-HPMA copolymer

As discussed earlier, while the *in vitro* studies showed enhanced internalization of positive BBN-HPMA copolymers into PC-3 cells via GRPR targeting, the *in vivo* studies showed rapid recognition by the immune cells. One approach to address this issue is by designing a charge-switch BBN-HPMA copolymer. The positive BBN-HPMA copolymer can also be designed to contain an acid-labile bond that links a carboxylic acid group to the copolymer's backbone, which will afford a zwitterionic BBN-HPMA copolymer. For example, instead of modifying the BBN peptide analog with two arginines, a modification is made so that it contains an arginine residue and a lysine residue. The same strategy for BBN conjugation to the HPMA copolymer is applied, and the free amines of lysine amino acids within the copolymer are reacted with 2,3-dimethyl maleic anhydride in the last step to afford acid-labile bonds (263, 264). If necessary, APMA-DTPA can replace the APMA-DOTA to perform the radiolabeling with ^{177}Lu under physiologic conditions (e.g., 37 °C and pH = 7.4). This approach is expected to increase the stability against easy recognition by immune cells (due to a zwitterionic polymeric backbone instead of positively charged backbone (265, 266)). It is also expected to render the BBN-HPMA copolymer GRPR-active (due to charge switch into positive at the extracellular environment of the tumor tissues).

5.2.2 Improving reaction kinetics by using a more strained TCO (sTCO)

In the third chapter, we discussed the reaction kinetics between the synthesized TCO-C linker and DOTA-TZ 2. The second-order rate constant was estimated to be ~ 10,000 $M^{-1} S^{-1}$. The type of TCO used in our study is considered a first-generation. Recent studies showed that using a more strained TCO (sTCO) leads to second-order constants 100,000 to 3,300,000 $M^{-1} S^{-1}$ (92, 267, 268). The development of an sTCO-HPMA copolymer can show better *in vivo* reactivity at the tumor tissues. For this approach, using a masking agent (e.g., DP-TZ) is necessary to deactivate the highly reactive sTCO in the blood.

5.2.3 Optimizing the DTPA content to reduce kidney retention of P-DTPA

The observed kidney retention of ^{177}Lu in the group of mice injected with P-DTPA indicates the retention of complexed ^{177}Lu-P-DTPA. It has been reported that HPMA copolymers with higher carboxylic acid content (e.g., carboxylic acid-containing monomer) retain in the kidneys for longer times than HPMA copolymers with lower content (261, 262). The mol. concentration of the DTPA per HPMA copolymer in our system, P-DTPA, was 5.2%. The development of HPMA copolymers with DTPA contents that are lower than the tested DTPA content may lead to lower retention of the copolymers in the kidneys.

REFERENCES

1. Siegel RL, Miller KD, Jemal A. Cancer statistics, 2020. CA: A Cancer Journal for Clinicians. 2020;70(1):7-30.
2. Waldron N. Prostate cancer. Medicine (Abingdon 1995, UK ed);48(2):119-122.
3. Litwin MS, Tan H-J. The diagnosis and treatment of prostate cancer: a review. Jama. 2017;317(24):2532-2542.
4. Balk SP, Ko Y-J, Bubley GJ. Biology of prostate-specific antigen. Journal of clinical oncology. 2003;21(2):383-391.
5. Buyyounouski MK, Choyke PL, McKenney JK, Sartor O, Sandler HM, Amin MB, Kattan MW, Lin DW. Prostate cancer–major changes in the American Joint Committee on Cancer eighth edition cancer staging manual. CA: a cancer journal for clinicians. 2017;67(3):245-253.
6. Evans JD, Jethwa KR, Ost P, Williams S, Kwon ED, Lowe VJ, Davis BJ. Prostate cancer–specific PET radiotracers: A review on the clinical utility in recurrent disease. Practical radiation oncology. 2018;8(1):28-39.
7. Weiner A, Matulewicz R, Eggener S, Schaeffer EM. Increasing incidence of metastatic prostate cancer in the United States (2004–2013). Prostate cancer and prostatic diseases. 2016;19(4):395-397.
8. Sumanasuriya S, De Bono J. Treatment of advanced prostate cancer—A review of current therapies and future promise. Cold Spring Harbor Perspectives in Medicine. 2018;8(6):a030635.
9. Mottet N, Bellmunt J, Bolla M, Briers E, Cumberbatch MG, De Santis M, Fossati N, Gross T, Henry AM, Joniau S. EAU-ESTRO-SIOG guidelines on prostate cancer. Part 1: screening, diagnosis, and local treatment with curative intent. European urology. 2017;71(4):618-629.
10. Sturge J, Caley MP, Waxman J. Bone metastasis in prostate cancer: emerging therapeutic strategies. Nature reviews Clinical oncology. 2011;8(6):357.
11. Goyal J, Antonarakis ES. Bone-targeting radiopharmaceuticals for the treatment of prostate cancer with bone metastases. Cancer letters. 2012;323(2):135-146.
12. Parker CC, James ND, Brawley CD, Clarke NW, Hoyle AP, Ali A, Ritchie AW, Attard G, Chowdhury S, Cross W. Radiotherapy to the primary tumour for newly diagnosed, metastatic prostate cancer (STAMPEDE): a randomised controlled phase 3 trial. The Lancet. 2018;392(10162):2353-2366.
13. Howlader N, Noone A, Krapcho M, Miller D, Brest A, Yu M. SEER Cancer Statistics Review, 1975–2017, National Cancer Institute. Bethesda, MD. 2020. In.
14. Cho KR, Shih I-M. Ovarian cancer. Annual Review of Pathology: Mechanisms of Disease. 2009;4:287-313.
15. Lheureux S, Gourley C, Vergote I, Oza AM. Epithelial ovarian cancer. The Lancet. 2019;393(10177):1240-1253.
16. Prat J, Oncology FCoG. Staging classification for cancer of the ovary, fallopian tube, and peritoneum. International journal of gynaecology and obstetrics: the official organ of the International Federation of Gynaecology and Obstetrics. 2014;124(1):1.
17. Ryerson AB, Eheman C, Burton J, McCall N, Blackman D, Subramanian S, Richardson LC. Symptoms, diagnoses, and time to key diagnostic procedures among older US women with ovarian cancer. Obstetrics & Gynecology. 2007;109(5):1053-1061.
18. Chandra A, Pius C, Nabeel M, Nair M, Vishwanatha JK, Ahmad S, Basha R. Ovarian cancer: Current status and strategies for improving therapeutic outcomes. Cancer medicine. 2019;8(16):7018-7031.
19. Roett MA, Evans P. Ovarian cancer: an overview. American family physician. 2009;80(6):609-616.

20. Duffy M, Bonfrer J, Kulpa J, Rustin G, Soletormos G, Torre G, Tuxen M, Zwirner M. CA125 in ovarian cancer: European Group on Tumor Markers guidelines for clinical use. International Journal of Gynecologic Cancer. 2005;15(5).

21. Jacobs IJ, Menon U, Ryan A, Gentry-Maharaj A, Burnell M, Kalsi JK, Amso NN, Apostolidou S, Benjamin E, Cruickshank D. Ovarian cancer screening and mortality in the UK Collaborative Trial of Ovarian Cancer Screening (UKCTOCS): a randomised controlled trial. The Lancet. 2016;387(10022):945-956.

22. Mutch DG, Prat J. 2014 FIGO staging for ovarian, fallopian tube and peritoneal cancer. Gynecologic oncology. 2014;133(3):401-404.

23. Khiewvan B, Torigian DA, Emamzadehfard S, Paydary K, Salavati A, Houshmand S, Werner TJ, Alavi A. An update on the role of PET/CT and PET/MRI in ovarian cancer. European journal of nuclear medicine and molecular imaging. 2017;44(6):1079-1091.

24. Doubeni CA, Doubeni AR, Myers AE. Diagnosis and management of ovarian cancer. American family physician. 2016;93(11):937-944.

25. Matulonis UA, Sood AK, Fallowfield L, Howitt BE, Sehouli J, Karlan BY. Ovarian cancer. Nature Reviews Disease Primers. 2016;2(1):1-22.

26. Dilruba S, Kalayda GV. Platinum-based drugs: past, present and future. Cancer chemotherapy and pharmacology. 2016;77(6):1103-1124.

27. Kobayashi-Kato M, Yunokawa M, Bun S, Miyasaka N, Kato T, Tamura K. Platinum-free interval affects efficacy of following treatment for platinum-refractory or-resistant ovarian cancer. Cancer chemotherapy and pharmacology. 2019;84(1):33-39.

28. Du Bois A, Reuss A, Pujade-Lauraine E, Harter P, Ray-Coquard I, Pfisterer J. Role of surgical outcome as prognostic factor in advanced epithelial ovarian cancer: a combined exploratory analysis of 3 prospectively randomized phase 3 multicenter trials: by the Arbeitsgemeinschaft Gynaekologische Onkologie Studiengruppe Ovarialkarzinom (AGO-OVAR) and the Groupe d'Investigateurs Nationaux Pour les Etudes des Cancers de l'Ovaire (GINECO). Cancer. 2009;115(6):1234-1244.

29. Franzese E, Centonze S, Diana A, Carlino F, Guerrera LP, Di Napoli M, De Vita F, Pignata S, Ciardiello F, Orditura M. PARP inhibitors in ovarian cancer. Cancer Treatment Reviews. 2019;73:1-9.

30. McCormack M. Radiation Therapy in Ovarian Cancer: An Overview and Future Directions. Clin Oncol (R Coll Radiol). 2018;30(8):504-506.

31. Iorio GC, Martini S, Arcadipane F, Ricardi U, Franco P. The role of radiotherapy in epithelial ovarian cancer: a literature overview. Med Oncol. 2019;36(7):64.

32. Rochet N, Lindel K, Katayama S, Schubert K, Herfarth K, Schneeweiss A, Sohn C, Harms W, Debus J. Intensity-modulated whole abdomen irradiation following adjuvant carboplatin/taxane chemotherapy for FIGO stage III ovarian cancer : four-year outcomes. Strahlenther Onkol. 2015;191(7):582-589.

33. Frangioni JV. New technologies for human cancer imaging. Journal of clinical oncology. 2008;26(24):4012.

34. Garibaldi C, Jereczek-Fossa BA, Marvaso G, Dicuonzo S, Rojas DP, Cattani F, Starzyńska A, Ciardo D, Surgo A, Leonardi MC. Recent advances in radiation oncology. ecancermedicalscience. 2017;11.

35. Pimlott SL, Sutherland A. Molecular tracers for the PET and SPECT imaging of disease. Chemical Society Reviews. 2011;40(1):149-162.

36. Hennrich U, Benešová M. [68Ga] Ga-DOTA-TOC: The First FDA-Approved 68Ga-Radiopharmaceutical for PET Imaging. Pharmaceuticals. 2020;13(3):38.

37. Altai M, Membreno R, Cook B, Tolmachev V, Zeglis BM. Pretargeted imaging and therapy. Journal of Nuclear Medicine. 2017;58(10):1553-1559.

38. Pooja D, Gunukula A, Gupta N, Adams DJ, Kulhari H. Bombesin Receptors as Potential Targets for Anticancer Drug Delivery and Imaging. The international journal of biochemistry & cell biology. 2019:105567.
39. Byun Y, Pullambhatla M, Wang H, Mease RC, Pomper MG. Synthesis and Biological Evaluation of Substrate-Based Imaging Agents for the Prostate-Specific Membrane Antigen. Macromol Res. 2013;21(5):565-573.
40. De Ruysscher D, Niedermann G, Burnet NG, Siva S, Lee AW, Hegi-Johnson F. Radiotherapy toxicity. Nature Reviews Disease Primers. 2019;5(1):1-20.
41. Gudkov SV, Shilyagina NY, Vodeneev VA, Zvyagin AV. Targeted radionuclide therapy of human tumors. International journal of molecular sciences. 2016;17(1):33.
42. Baum RP, Singh A, Schuchardt C, Kulkarni HR, Klette I, Wiessalla S, Osterkamp F, Reineke U, Smerling C. 177Lu-3BP-227 for neurotensin receptor 1–targeted therapy of metastatic pancreatic adenocarcinoma: First clinical results. Journal of Nuclear Medicine. 2018;59(5):809-814.
43. Sgouros G, Bodei L, McDevitt MR, Nedrow JR. Radiopharmaceutical therapy in cancer: clinical advances and challenges. Nature Reviews Drug Discovery. 2020:1-20.
44. Wester H-J, Schottelius M. PSMA-targeted radiopharmaceuticals for imaging and therapy. In.Seminars in nuclear medicine: Elsevier; 2019. p. 302-312.
45. Goldsmith SJ. Radioimmunotherapy of lymphoma: Bexxar and Zevalin. In.Seminars in nuclear medicine: Elsevier; 2010. p. 122-135.
46. Green DJ, Press OW. Whither radioimmunotherapy: to be or not to be? Cancer research. 2017;77(9):2191-2196.
47. Hennrich U, Kopka K. Lutathera®: The First FDA-and EMA-approved radiopharmaceutical for peptide receptor radionuclide therapy. Pharmaceuticals. 2019;12(3):114.
48. Hossen S, Hossain MK, Basher M, Mia M, Rahman M, Uddin MJ. Smart nanocarrier-based drug delivery systems for cancer therapy and toxicity studies: A review. Journal of advanced research. 2019;15:1-18.
49. Rosenblum D, Joshi N, Tao W, Karp JM, Peer D. Progress and challenges towards targeted delivery of cancer therapeutics. Nature communications. 2018;9(1):1410.
50. Shi J, Kantoff PW, Wooster R, Farokhzad OC. Cancer nanomedicine: progress, challenges and opportunities. Nature Reviews Cancer. 2017;17(1):20.
51. Barenholz YC. Doxil®—the first FDA-approved nano-drug: lessons learned. Journal of controlled release. 2012;160(2):117-134.
52. Bobo D, Robinson KJ, Islam J, Thurecht KJ, Corrie SR. Nanoparticle-based medicines: a review of FDA-approved materials and clinical trials to date. Pharmaceutical research. 2016;33(10):2373-2387.
53. Sofias AM, Dunne M, Storm G, Allen C. The battle of "nano" paclitaxel. Adv Drug Deliv Rev. 2017;122:20-30.
54. Kobayashi H, Watanabe R, Choyke PL. Improving conventional enhanced permeability and retention (EPR) effects; what is the appropriate target? Theranostics. 2014;4(1):81.
55. Gustafson HH, Holt-Casper D, Grainger DW, Ghandehari H. Nanoparticle uptake: the phagocyte problem. Nano today. 2015;10(4):487-510.
56. Ishida T, Ichihara M, Wang X, Kiwada H. Spleen plays an important role in the induction of accelerated blood clearance of PEGylated liposomes. J Control Release. 2006;115(3):243-250.
57. Owens III DE, Peppas NA. Opsonization, biodistribution, and pharmacokinetics of polymeric nanoparticles. International journal of pharmaceutics. 2006;307(1):93-102.
58. Sun X, Yan X, Jacobson O, Sun W, Wang Z, Tong X, Xia Y, Ling D, Chen X. Improved tumor uptake by optimizing liposome based RES blockade strategy. Theranostics. 2017;7(2):319.
59. Mohamed M, Abu Lila AS, Shimizu T, Alaaeldin E, Hussein A, Sarhan HA, Szebeni J, Ishida T. PEGylated liposomes: immunological responses. Science and technology of advanced materials. 2019;20(1):710-724.

60. Fang Y, Xue J, Gao S, Lu A, Yang D, Jiang H, He Y, Shi K. Cleavable PEGylation: a strategy for overcoming the "PEG dilemma" in efficient drug delivery. Drug Delivery. 2017;24(2):22-32.
61. Cao B, Tang Q, Li L, Lee CJ, Wang H, Zhang Y, Castaneda H, Cheng G. Integrated zwitterionic conjugated poly(carboxybetaine thiophene) as a new biomaterial platform. Chem Sci. 2015;6(1):782-788.
62. Folkman J. Fundamental concepts of the angiogenic process. Current molecular medicine. 2003;3(7):643-651.
63. Hashizume H, Baluk P, Morikawa S, McLean JW, Thurston G, Roberge S, Jain RK, McDonald DM. Openings between defective endothelial cells explain tumor vessel leakiness. The American journal of pathology. 2000;156(4):1363-1380.
64. Matsumura Y, Maeda H. A new concept for macromolecular therapeutics in cancer chemotherapy: mechanism of tumoritropic accumulation of proteins and the antitumor agent smancs. Cancer research. 1986;46(12 Part 1):6387-6392.
65. Maeda H. Polymer therapeutics and the EPR effect. Journal of drug targeting. 2017;25(9-10):781-785.
66. Shi Y, van der Meel R, Chen X, Lammers T. The EPR effect and beyond: Strategies to improve tumor targeting and cancer nanomedicine treatment efficacy. Theranostics. 2020;10(17):7921.
67. Goos JA, Cho A, Carter LM, Dilling TR, Davydova M, Mandleywala K, Puttick S, Gupta A, Price WS, Quinn JF. Delivery of polymeric nanostars for molecular imaging and endoradiotherapy through the enhanced permeability and retention (EPR) effect. Theranostics. 2020;10(2):567.
68. Danhier F. To exploit the tumor microenvironment: Since the EPR effect fails in the clinic, what is the future of nanomedicine? Journal of Controlled Release. 2016;244:108-121.
69. Wilhelm S, Tavares AJ, Dai Q, Ohta S, Audet J, Dvorak HF, Chan WC. Analysis of nanoparticle delivery to tumours. Nature reviews materials. 2016;1(5):1-12.
70. Sindhwani S, Syed AM, Ngai J, Kingston BR, Maiorino L, Rothschild J, MacMillan P, Zhang Y, Rajesh NU, Hoang T. The entry of nanoparticles into solid tumours. Nature materials. 2020;19(5):566-575.
71. Bazak R, Houri M, El Achy S, Kamel S, Refaat T. Cancer active targeting by nanoparticles: a comprehensive review of literature. Journal of cancer research and clinical oncology. 2015;141(5):769-784.
72. Ji X, Pan Z, Yu B, De La Cruz LK, Zheng Y, Ke B, Wang B. Click and release: bioorthogonal approaches to "on-demand" activation of prodrugs. Chemical Society Reviews. 2019;48(4):1077-1094.
73. Royzen M, Yee N, Mejia Oneto JM. In Vivo Bioconjugation Using Bio-orthogonal Chemistry. Handbook of In Vivo Chemistry in Mice: From Lab to Living System. 2020:249-279.
74. Patel O, Shulkes A, Baldwin GS. Gastrin-releasing peptide and cancer. Biochimica et Biophysica Acta (BBA)-Reviews on Cancer. 2006;1766(1):23-41.
75. Zhang Q, Thomas SM, Lui VWY, Xi S, Siegfried JM, Fan H, Smithgall TE, Mills GB, Grandis JR. Phosphorylation of TNF-α converting enzyme by gastrin-releasing peptide induces amphiregulin release and EGF receptor activation. Proceedings of the National Academy of Sciences. 2006;103(18):6901-6906.
76. Baratto L, Jadvar H, Iagaru A. Prostate cancer theranostics targeting gastrin-releasing peptide receptors. Molecular Imaging and Biology. 2018;20(4):501-509.
77. Moreno P, Ramos-Alvarez I, Moody TW, Jensen RT. Bombesin related peptides/receptors and their promising therapeutic roles in cancer imaging, targeting and treatment. Expert opinion on therapeutic targets. 2016;20(9):1055-1073.
78. Gibbens-Bandala B, Morales-Avila E, Ferro-Flores G, Santos-Cuevas C, Meléndez-Alafort L, Trujillo-Nolasco M, Ocampo-García B. 177Lu-Bombesin-PLGA (paclitaxel): A targeted

controlled-release nanomedicine for bimodal therapy of breast cancer. Materials Science and Engineering: C. 2019;105:110043.
79. Radhakrishnan R, Pooja D, Kulhari H, Gudem S, Ravuri HG, Bhargava S, Ramakrishna S. Bombesin conjugated solid lipid nanoparticles for improved delivery of epigallocatechin gallate for breast cancer treatment. Chemistry and physics of lipids. 2019;224:104770.
80. Salouti M, Saghatchi F. BBN conjugated GNPs: a new targeting contrast agent for imaging of breast cancer in radiology. IET Nanobiotechnol. 2017;11(5):604-611.
81. Chanda N, Kattumuri V, Shukla R, Zambre A, Katti K, Upendran A, Kulkarni RR, Kan P, Fent GM, Casteel SW, Smith CJ, Boote E, Robertson JD, Cutler C, Lever JR, Katti KV, Kannan R. Bombesin functionalized gold nanoparticles show in vitro and in vivo cancer receptor specificity. Proc Natl Acad Sci U S A. 2010;107(19):8760-8765.
82. Cai H, Xie F, Mulgaonkar A, Chen L, Sun X, Hsieh J-T, Peng F, Tian R, Li L, Wu C. Bombesin functionalized 64Cu-copper sulfide nanoparticles for targeted imaging of orthotopic prostate cancer. Nanomedicine. 2018(0).
83. Sletten EM, Bertozzi CR. From mechanism to mouse: a tale of two bioorthogonal reactions. Accounts of chemical research. 2011;44(9):666-676.
84. Baskin JM, Prescher JA, Laughlin ST, Agard NJ, Chang PV, Miller IA, Lo A, Codelli JA, Bertozzi CR. Copper-free click chemistry for dynamic in vivo imaging. Proceedings of the National Academy of Sciences. 2007;104(43):16793-16797.
85. Selvaraj R, Fox JM. trans-Cyclooctene—a stable, voracious dienophile for bioorthogonal labeling. Current opinion in chemical biology. 2013;17(5):753-760.
86. Royzen M, Yap GP, Fox JM. A photochemical synthesis of functionalized trans-cyclooctenes driven by metal complexation. Journal of the American Chemical Society. 2008;130(12):3760-3761.
87. Blackman ML, Royzen M, Fox JM. Tetrazine ligation: fast bioconjugation based on inverse-electron-demand Diels− Alder reactivity. Journal of the American Chemical Society. 2008;130(41):13518-13519.
88. Läppchen T, Rossin R, van Mourik TR, Gruntz G, Hoeben FJ, Versteegen RM, Janssen HM, Lub J, Robillard MS. DOTA-tetrazine probes with modified linkers for tumor pretargeting. Nuclear medicine and biology. 2017;55:19-26.
89. Meyer J-P, Tully KM, Jackson J, Dilling TR, Reiner T, Lewis JS. Bioorthogonal masking of circulating antibody–TCO groups using tetrazine-functionalized dextran polymers. Bioconjugate chemistry. 2018;29(2):538-545.
90. Goos JA, Davydova M, Dilling TR, Cho A, Cornejo MA, Gupta A, Price WS, Puttick S, Whittaker MR, Quinn JF. Design and preclinical evaluation of nanostars for the passive pretargeting of tumor tissue. Nuclear medicine and biology. 2020.
91. Qiu L, Mao W, Yin H, Tan H, Cheng D, Shi H. Pretargeted Nuclear Imaging and Radioimmunotherapy Based on the Inverse Electron-Demand Diels–Alder Reaction and Key Factors in the Pretargeted Synthetic Design. Contrast Media & Molecular Imaging. 2019;2019.
92. Rossin R, van den Bosch SM, ten Hoeve W, Carvelli M, Versteegen RM, Lub J, Robillard MS. Highly reactive trans-cyclooctene tags with improved stability for Diels–Alder chemistry in living systems. Bioconjugate chemistry. 2013;24(7):1210-1217.
93. Mandikian D, Rafidi H, Adhikari P, Venkatraman P, Nazarova L, Fung G, Figueroa I, Ferl GZ, Ulufatu S, Ho J. Site-specific conjugation allows modulation of click reaction stoichiometry for pretargeted SPECT imaging. In.Mabs: Taylor & Francis; 2018. p. 1269-1280.
94. Membreno R, Cook BE, Fung K, Lewis JS, Zeglis BM. Click-mediated pretargeted radioimmunotherapy of colorectal carcinoma. Molecular pharmaceutics. 2018;15(4):1729-1734.
95. Jatzkewitz H. Peptamin (glycyl-L-leucyl-mescaline) bound to blood plasma expander (polyvinylpyrrolidone) as a new depot form of a biologically active primary amine (mescaline). Z Naturforsch. 1955;10:27-31.

96. Ringsdorf H. Structure and properties of pharmacologically active polymers. In.Journal of Polymer Science: Polymer Symposia: Wiley Online Library; 1975. p. 135-153.
97. Kopeček J, Kopečková P. HPMA copolymers: origins, early developments, present, and future. Advanced drug delivery reviews. 2010;62(2):122-149.
98. Alconcel SN, Baas AS, Maynard HD. FDA-approved poly (ethylene glycol)–protein conjugate drugs. Polymer Chemistry. 2011;2(7):1442-1448.
99. Ekladious I, Colson YL, Grinstaff MW. Polymer–drug conjugate therapeutics: advances, insights and prospects. Nature reviews Drug discovery. 2019;18(4):273-294.
100. Rani S, Gupta U. HPMA-based polymeric conjugates in anticancer therapeutics. Drug Discovery Today. 2020.
101. Yang J, Kopeček J. Design of smart HPMA copolymer-based nanomedicines. Journal of Controlled Release. 2016;240:9-23.
102. Moad G, Chong Y, Postma A, Rizzardo E, Thang SH. Advances in RAFT polymerization: the synthesis of polymers with defined end-groups. Polymer. 2005;46(19):8458-8468.
103. Nuhn L, Barz M, Zentel R. New Perspectives of HPMA-based Copolymers Derived by Post-Polymerization Modification. Macromolecular bioscience. 2014;14(5):607-618.
104. Tao L, Liu J, Davis TP. Branched polymer− protein conjugates made from mid-chain-functional P (HPMA). Biomacromolecules. 2009;10(10):2847-2851.
105. Liu J, Bauer H, Callahan J, Kopečková P, Pan H, Kopeček J. Endocytic uptake of a large array of HPMA copolymers: Elucidation into the dependence on the physicochemical characteristics. Journal of Controlled Release. 2010;143(1):71-79.
106. Li L, Yang Q, Zhou Z, Zhong J, Huang Y. Doxorubicin-loaded, charge reversible, folate modified HPMA copolymer conjugates for active cancer cell targeting. Biomaterials. 2014;35(19):5171-5187.
107. Lammers T, Kuhnlein R, Kissel M, Subr V, Etrych T, Pola R, Pechar M, Ulbrich K, Storm G, Huber P, Peschke P. Effect of physicochemical modification on the biodistribution and tumor accumulation of HPMA copolymers. J Control Release. 2005;110(1):103-118.
108. Mitra A, Nan A, Ghandehari H, McNeil E, Mulholland J, Line BR. Technetium-99m-Labeled N-(2-hydroxypropyl) methacrylamide copolymers: synthesis, characterization, and in vivo biodistribution. Pharmaceutical research. 2004;21(7):1153-1159.
109. Lammers T, Kühnlein R, Kissel M, Subr V, Etrych T, Pola R, Pechar M, Ulbrich K, Storm G, Huber P. Effect of physicochemical modification on the biodistribution and tumor accumulation of HPMA copolymers. Journal of controlled release. 2005;110(1):103-118.
110. Mccormick LA, Seymour LC, Duncan R, Kopecek J. Interaction of a cationic N-(2-hydroxypropyl) methacrylamide copolymer with rat visceral yolk sacs cultured in vitro and rat liver in vivo. Journal of Bioactive and Compatible Polymers. 1986;1(1):4-19.
111. Armstrong BK, Smith Q, Rapoport SI, Strohalm J, Kopeček J, Duncan R. Osmotic opening of the blood-brain barrier permeability to N-(2-hydroxypropyl)methacrylamide copolymers. Effect of polymer -Mw charge and hydrophobicity. Journal of Controlled Release. 1989;10(1):27-35.
112. Berdowska I. Cysteine proteases as disease markers. Clinica chimica acta. 2004;342(1-2):41-69.
113. McDowell SH, Gallaher SA, Burden RE, Scott CJ. Leading the invasion: The role of Cathepsin S in the tumour microenvironment. Biochimica et Biophysica Acta (BBA)-Molecular Cell Research. 2020:118781.
114. Olson OC, Joyce JA. Cysteine cathepsin proteases: regulators of cancer progression and therapeutic response. Nature Reviews Cancer. 2015;15(12):712-729.
115. Pišlar A, Jewett A, Kos J. Cysteine cathepsins: Their biological and molecular significance in cancer stem cells. In.Seminars in cancer biology: Elsevier; 2018. p. 168-177.
116. Dheer D, Nicolas J, Shankar R. Cathepsin-sensitive nanoscale drug delivery systems for cancer therapy and other diseases. Advanced Drug Delivery Reviews. 2019;151:130-151.

117. Fan W, Shi W, Zhang W, Jia Y, Zhou Z, Brusnahan SK, Garrison JC. Cathepsin S-cleavable, multi-block HPMA copolymers for improved SPECT/CT imaging of pancreatic cancer. Biomaterials. 2016;103:101-115.
118. Pan H, Sima M, Yang J, Kopeček J. Synthesis of Long-Circulating, Backbone Degradable HPMA Copolymer–Doxorubicin Conjugates and Evaluation of Molecular-Weight-Dependent Antitumor Efficacy. Macromolecular bioscience. 2013;13(2):155-160.
119. Zhang R, Luo K, Yang J, Sima M, Sun Y, Janát-Amsbury MM, Kopeček J. Synthesis and evaluation of a backbone biodegradable multiblock HPMA copolymer nanocarrier for the systemic delivery of paclitaxel. Journal of Controlled Release. 2013;166(1):66-74.
120. Fan W, Zhang W, Jia Y, Brusnahan SK, Garrison JC. Investigation into the Biological Impact of Block Size on Cathepsin S-Degradable HPMA Copolymers. Molecular pharmaceutics. 2017;14(5):1405-1417.
121. Seymour LW, Ferry DR, Anderson D, Hesslewood S, Julyan PJ, Poyner R, Doran J, Young AM, Burtles S, Kerr DJ. Hepatic drug targeting: phase I evaluation of polymer-bound doxorubicin. Journal of clinical oncology. 2002;20(6):1668-1676.
122. Seymour LW, Ferry DR, Kerr DJ, Rea D, Whitlock M, Poyner R, Boivin C, Hesslewood S, Twelves C, Blackie R. Phase II studies of polymer-doxorubicin (PK1, FCE28068) in the treatment of breast, lung and colorectal cancer. International journal of oncology. 2009;34(6):1629-1636.
123. Terwogt JMM, ten Bokkel Huinink WW, Schellens JH, Schot M, Mandjes IA, Zurlo MG, Rocchetti M, Rosing H, Koopman FJ, Beijnen JH. Phase I clinical and pharmacokinetic study of PNU166945, a novel water-soluble polymer-conjugated prodrug of paclitaxel. Anti-cancer drugs. 2001;12(4):315-323.
124. Rademaker-Lakhai JM, Terret C, Howell SB, Baud CM, de Boer RF, Pluim D, Beijnen JH, Schellens JH, Droz J-P. A Phase I and pharmacological study of the platinum polymer AP5280 given as an intravenous infusion once every 3 weeks in patients with solid tumors. Clinical Cancer Research. 2004;10(10):3386-3395.
125. Nowotnik DP, Cvitkovic E. ProLindac™(AP5346): a review of the development of an HPMA DACH platinum polymer therapeutic. Advanced drug delivery reviews. 2009;61(13):1214-1219.
126. Dozono H, Yanazume S, Nakamura H, Etrych T, Chytil P, Ulbrich K, Fang J, Arimura T, Douchi T, Kobayashi H. HPMA copolymer-conjugated pirarubicin in multimodal treatment of a patient with stage IV prostate cancer and extensive lung and bone metastases. Targeted oncology. 2016;11(1):101-106.
127. Williams M, Sizemore DC. Biologic, chemical, and radiation terrorism review. In. StatPearls [Internet]: StatPearls Publishing; 2020.
128. Hasegawa A, Ohira T, Maeda M, Yasumura S, Tanigawa K. Emergency responses and health consequences after the Fukushima accident; evacuation and relocation. Clinical Oncology. 2016;28(4):237-244.
129. Yamamoto M, Takada T, Nagao S, Koike T, Shimada K, Hoshi M, Zhumadilov K, Shima T, Fukuoka M, Imanaka T. An early survey of the radioactive contamination of soil due to the Fukushima Dai-ichi Nuclear Power Plant accident, with emphasis on plutonium analysis. Geochemical Journal. 2012;46(4):341-353.
130. Hirose K. 2011 Fukushima Dai-ichi nuclear power plant accident: summary of regional radioactive deposition monitoring results. Journal of environmental radioactivity. 2012;111:13-17.
131. Koo Y-H, Yang Y-S, Song K-W. Radioactivity release from the Fukushima accident and its consequences: A review. Progress in Nuclear Energy. 2014;74:61-70.
132. Zheng J, Tagami K, Watanabe Y, Uchida S, Aono T, Ishii N, Yoshida S, Kubota Y, Fuma S, Ihara S. Isotopic evidence of plutonium release into the environment from the Fukushima DNPP accident. Scientific reports. 2012;2(1):1-8.

133. Peterson J, MacDonell M, Haroun L, Monette F, Hildebrand RD, Taboas A. Radiological and chemical fact sheets to support health risk analyses for contaminated areas. Argonne National Laboratory Environmental Science Division. 2007;133.
134. Ansoborlo É, Amekraz B, Moulin C, Moulin V, Taran F, Bailly T, Burgada R, Hengé-Napoli M-H, Jeanson A, Den Auwer C. Review of actinide decorporation with chelating agents. Comptes Rendus Chimie. 2007;10(10-11):1010-1019.
135. Taylor DM. The biodistribution and toxicity of plutonium, americium and neptunium. Science of the total environment. 1989;83(3):217-225.
136. Stannard J. Toxicology of radionuclides. Annual Review of Pharmacology. 1973;13(1):325-357.
137. Guilmette R, Cohen N, Wrenn M. Distribution and retention of 241Am in the baboon. Radiation research. 1980;81(1):100-119.
138. Volf V. Effect of drinking Zn-DTPA on 238-Pu and 241-Am in rat bones. Radiation and environmental biophysics. 1984;23(2):141-143.
139. McAfee JG, Gagne G, Atkins HL, Kirchner PT, Reba RC, Blaufox MD, Smith EM. Biological distribution and excretion of DTPA labeled with Tc-99m and In-111. Journal of Nuclear Medicine. 1979;20(12):1273-1278.
140. Stather J, Smith H, Bailey M, Birchall A, Bulman R, Crawley F. The retention of 14C-DTPA in human volunteers after inhalation or intravenous injection. Health physics. 1983;44(1):45-52.
141. Fattal E, Tsapis N, Phan G. Novel drug delivery systems for actinides (uranium and plutonium) decontamination agents. Advanced drug delivery reviews. 2015;90:40-54.
142. An DD, Kullgren B, Jarvis EE, Abergel RJ. From early prophylaxis to delayed treatment: Establishing the plutonium decorporation activity window of hydroxypyridinonate chelating agents. Chemico-biological interactions. 2017;267:80-88.
143. Jech J, Andersen B, Heid K. Interpretation of human urinary excretion of plutonium for cases treated with DTPA. Health physics. 1972;22(6):787-792.
144. Grémy O, Miccoli L, Lelan F, Bohand S, Cherel M, Mougin-Degraef M. Delivery of DTPA through liposomes as a good strategy for enhancing plutonium decorporation regardless of treatment regimen. Radiation research. 2018;189(5):477-489.
145. Léost L, Roques J, Van Der Meeren A, Vincent L, Sbirrazzuoli N, Hennig C, Rossberg A, Aupiais J, Pagnotta S, Den Auwer C. Towards the development of chitosan nanoparticles for plutonium pulmonary decorporation. Dalton Transactions. 2018;47(33):11605-11618.
146. Chen S, Ko R, Lai EP, Wyatt H, Abergel RJ, Li C. Encapsulated 3, 4, 3-LI (1, 2-HOPO) in chitosan nanoparticles for decorporation via inhalation. Radiation protection dosimetry. 2018;182(1):107-111.
147. Markwalder R, Reubi JC. Gastrin-releasing peptide receptors in the human prostate: Relation to neoplastic transformation. Cancer Research. 1999;59(5):1152-1159.
148. Yu Z, Ananias HJ, Carlucci G, Hoving HD, Helfrich W, Dierckx RA, Wang F, de Jong IJ, Elsinga PH. An update of radiolabeled bombesin analogs for gastrin-releasing peptide receptor targeting. Curr Pharm Des. 2013;19(18):3329-3341.
149. Aloj L, Attili B, Lau D, Caraco C, Lechermann LM, Mendichovszky IA, Harper I, Cheow H, Casey RT, Sala E. The emerging role of cell surface receptor and protein binding radiopharmaceuticals in cancer diagnostics and therapy. Nuclear Medicine and Biology. 2020.
150. Accardo A, Galli F, Mansi R, Del Pozzo L, Aurilio M, Morisco A, Ringhieri P, Signore A, Morelli G, Aloj L. Pre-clinical evaluation of eight DOTA coupled gastrin-releasing peptide receptor (GRP-R) ligands for in vivo targeting of receptor-expressing tumors. EJNMMI research. 2016;6(1):17.
151. Hoppenz P, Els-Heindl S, Beck-Sickinger AG. Identification and stabilization of a highly selective gastrin-releasing peptide receptor agonist. Journal of Peptide Science. 2019;25(12):e3224.

152. Kurth J, Krause BJ, Schwarzenbock SM, Bergner C, Hakenberg OW, Heuschkel M. First-in-human dosimetry of gastrin-releasing peptide receptor antagonist [(177)Lu]Lu-RM2: a radiopharmaceutical for the treatment of metastatic castration-resistant prostate cancer. Eur J Nucl Med Mol Imaging. 2020;47(1):123-135.
153. Zhang J, Niu G, Fan X, Lang L, Hou G, Chen L, Wu H, Zhu Z, Li F, Chen X. PET Using a GRPR Antagonist (68)Ga-RM26 in Healthy Volunteers and Prostate Cancer Patients. J Nucl Med. 2018;59(6):922-928.
154. Wieser G, Mansi R, Grosu AL, Schultze-Seemann W, Dumont-Walter RA, Meyer PT, Maecke HR, Reubi JC, Weber WA. Positron emission tomography (PET) imaging of prostate cancer with a gastrin releasing peptide receptor antagonist--from mice to men. Theranostics. 2014;4(4):412-419.
155. Rizzo LY, Theek B, Storm G, Kiessling F, Lammers T. Recent progress in nanomedicine: therapeutic, diagnostic and theranostic applications. Curr Opin Biotechnol. 2013;24(6):1159-1166.
156. Lammers T, Aime S, Hennink WE, Storm G, Kiessling F. Theranostic nanomedicine. Acc Chem Res. 2011;44(10):1029-1038.
157. Soares S, Sousa J, Pais A, Vitorino C. Nanomedicine: Principles, Properties, and Regulatory Issues. Front Chem. 2018;6:360.
158. Maeda H. Toward a full understanding of the EPR effect in primary and metastatic tumors as well as issues related to its heterogeneity. Adv Drug Deliv Rev. 2015;91:3-6.
159. Bertrand N, Wu J, Xu X, Kamaly N, Farokhzad OC. Cancer nanotechnology: the impact of passive and active targeting in the era of modern cancer biology. Advanced drug delivery reviews. 2014;66:2-25.
160. Lee C-M, Jeong H-J, Cheong S-J, Kim E-M, Kim DW, Lim ST, Sohn M-H. Prostate cancer-targeted imaging using magnetofluorescent polymeric nanoparticles functionalized with bombesin. Pharmaceutical research. 2010;27(4):712-721.
161. Li R, Gao R, Wang Y, Liu Z, Xu H, Duan A, Zhang F, Ma L. Gastrin releasing peptide receptor targeted nano-graphene oxide for near-infrared fluorescence imaging of oral squamous cell carcinoma. Scientific Reports. 2020;10(1):1-12.
162. Kirpotin DB, Drummond DC, Shao Y, Shalaby MR, Hong K, Nielsen UB, Marks JD, Benz CC, Park JW. Antibody targeting of long-circulating lipidic nanoparticles does not increase tumor localization but does increase internalization in animal models. Cancer Res. 2006;66(13):6732-6740.
163. Schmidt MM, Wittrup KD. A modeling analysis of the effects of molecular size and binding affinity on tumor targeting. Mol Cancer Ther. 2009;8(10):2861-2871.
164. Chytil P, Koziolová E, Etrych T, Ulbrich K. HPMA Copolymer–Drug Conjugates with Controlled Tumor-Specific Drug Release. Macromolecular bioscience. 2018;18(1):1700209.
165. Pike DB, Ghandehari H. HPMA copolymer-cyclic RGD conjugates for tumor targeting. Adv Drug Deliv Rev. 2010;62(2):167-183.
166. Allmeroth M, Moderegger D, Gündel D, Buchholz HG, Mohr N, Koynov K, Rosch F, Thews O, Zentel R. PEGylation of HPMA-based block copolymers enhances tumor accumulation in vivo: a quantitative study using radiolabeling and positron emission tomography. Journal of controlled release. 2013;172(1):77-85.
167. Allmeroth M, Moderegger D, Biesalski B, Koynov K, Rösch F, Thews O, Zentel R. Modifying the body distribution of HPMA-based copolymers by molecular weight and aggregate formation. Biomacromolecules. 2011;12(7):2841-2849.
168. Omelyanenko V, Kopeckova P, Gentry C, Kopecek J. Targetable HPMA copolymer-adriamycin conjugates. Recognition, internalization, and subcellular fate. J Control Release. 1998;53(1-3):25-37.
169. Li C, Winnard PT, Takagi T, Artemov D, Bhujwalla ZM. Multimodal image-guided enzyme/prodrug cancer therapy. Journal of the American Chemical Society. 2006;128(47):15072-15073.

170. Buckway B, Frazier N, Gormley AJ, Ray A, Ghandehari H. Gold nanorod-mediated hyperthermia enhances the efficacy of HPMA copolymer-90Y conjugates in treatment of prostate tumors. Nuclear medicine and biology. 2014;41(3):282-289.
171. Yi Y, Kim HJ, Mi P, Zheng M, Takemoto H, Toh K, Kim BS, Hayashi K, Naito M, Matsumoto Y. Targeted systemic delivery of siRNA to cervical cancer model using cyclic RGD-installed unimer polyion complex-assembled gold nanoparticles. Journal of controlled release. 2016;244:247-256.
172. Yang M, Gao H, Zhou Y, Ma Y, Quan Q, Lang L, Chen K, Niu G, Yan Y, Chen X. 18F-labeled GRPR agonists and antagonists: a comparative study in prostate cancer imaging. Theranostics. 2011;1:220.
173. Zhang W, Fan W, Ottemann BM, Alshehri S, Garrison JC. Development of Improved Tumor-Residualizing, GRPR-Targeted Agents: Preclinical Comparison of an Endolysosomal Trapping Approach in Agonistic and Antagonistic Constructs. Journal of Nuclear Medicine. 2020;61(3):443-450.
174. Montet X, Weissleder R, Josephson L. Imaging pancreatic cancer with a peptide–nanoparticle conjugate targeted to normal pancreas. Bioconjugate chemistry. 2006;17(4):905-911.
175. Etrych T, Šubr V, Strohalm J, Šírová M, Říhová B, Ulbrich K. HPMA copolymer-doxorubicin conjugates: The effects of molecular weight and architecture on biodistribution and in vivo activity. Journal of controlled release. 2012;164(3):346-354.
176. Pike DB, Ghandehari H. HPMA copolymer–cyclic RGD conjugates for tumor targeting. Advanced drug delivery reviews. 2010;62(2):167-183.
177. de Aguiar Ferreira C, Fuscaldi LL, Townsend DM, Rubello D, de Barros ALB. Radiolabeled bombesin derivatives for preclinical oncological imaging. Biomedicine & Pharmacotherapy. 2017;87:58-72.
178. He C, Hu Y, Yin L, Tang C, Yin C. Effects of particle size and surface charge on cellular uptake and biodistribution of polymeric nanoparticles. Biomaterials. 2010;31(13):3657-3666.
179. Gu F, Zhang L, Teply BA, Mann N, Wang A, Radovic-Moreno AF, Langer R, Farokhzad OC. Precise engineering of targeted nanoparticles by using self-assembled biointegrated block copolymers. Proceedings of the National Academy of Sciences. 2008;105(7):2586-2591.
180. Varasteh Z, Mitran B, Rosenström U, Velikyan I, Rosestedt M, Lindeberg G, Sörensen J, Larhed M, Tolmachev V, Orlova A. The effect of macrocyclic chelators on the targeting properties of the 68Ga-labeled gastrin releasing peptide receptor antagonist PEG2-RM26. Nuclear medicine and biology. 2015;42(5):446-454.
181. Volková M, Mandikova J, Lázníčková A, Lázníček M, Bárta P, Trejtnar F. The involvement of selected membrane transport mechanisms in the cellular uptake of 177Lu-labeled bombesin, somatostatin and gastrin analogues. Nuclear medicine and biology. 2015;42(1):1-7.
182. Patel S, Kim J, Herrera M, Mukherjee A, Kabanov AV, Sahay G. Brief update on endocytosis of nanomedicines. Advanced drug delivery reviews. 2019;144:90-111.
183. Shan D, Li J, Cai P, Prasad P, Liu F, Rauth AM, Wu XY. RGD-conjugated solid lipid nanoparticles inhibit adhesion and invasion of α v β 3 integrin-overexpressing breast cancer cells. Drug delivery and translational research. 2015;5(1):15-26.
184. Alkilany AM, Zhu L, Weller H, Mews A, Parak WJ, Barz M, Feliu N. Ligand density on nanoparticles: A parameter with critical impact on nanomedicine. Advanced Drug Delivery Reviews. 2019;143:22-36.
185. Nanda PK, Pandey U, Bottenus BN, Rold TL, Sieckman GL, Szczodroski AF, Hoffman TJ, Smith CJ. Bombesin analogues for gastrin-releasing peptide receptor imaging. Nuclear medicine and biology. 2012;39(4):461-471.
186. Shi W, Ogbomo SM, Wagh NK, Zhou Z, Jia Y, Brusnahan SK, Garrison JC. The influence of linker length on the properties of cathepsin S cleavable 177Lu-labeled HPMA copolymers for pancreatic cancer imaging. Biomaterials. 2014;35(22):5760-5770.

187. Zhang C, Yan L, Wang X, Zhu S, Chen C, Gu Z, Zhao Y. Progress, challenges, and future of nanomedicine. Nano Today. 2020;35:101008.
188. Polyak A, Ross TL. Nanoparticles for SPECT and PET imaging: towards personalized medicine and theranostics. Current Medicinal Chemistry. 2018;25(34):4328-4353.
189. Satterlee AB, Yuan H, Huang L. A radio-theranostic nanoparticle with high specific drug loading for cancer therapy and imaging. Journal of Controlled Release. 2015;217:170-182.
190. Petersen AL, Henriksen JR, Binderup T, Elema DR, Rasmussen PH, Hag AM, Kjær A, Andresen TL. In vivo evaluation of PEGylated 64 Cu-liposomes with theranostic and radiotherapeutic potential using micro PET/CT. European journal of nuclear medicine and molecular imaging. 2016;43(5):941-952.
191. Jarrett BR, Gustafsson Br, Kukis DL, Louie AY. Synthesis of 64Cu-labeled magnetic nanoparticles for multimodal imaging. Bioconjugate Chemistry. 2008;19(7):1496-1504.
192. Steen EJL, Edem PE, Norregaard K, Jorgensen JT, Shalgunov V, Kjaer A, Herth MM. Pretargeting in nuclear imaging and radionuclide therapy: Improving efficacy of theranostics and nanomedicines. Biomaterials. 2018;179:209-245.
193. Rondon A, Ty N, Bequignat J-B, Quintana M, Briat A, Witkowski T, Bouchon B, Boucheix C, Miot-Noirault E, Pouget J-P. Antibody PEGylation in bioorthogonal pretargeting with trans-cyclooctene/tetrazine cycloaddition: in vitro and in vivo evaluation in colorectal cancer models. Scientific reports. 2017;7(1):1-11.
194. Meyer J-P, Kozlowski P, Jackson J, Cunanan KM, Adumeau P, Dilling TR, Zeglis BM, Lewis JS. Exploring structural parameters for pretargeting radioligand optimization. Journal of medicinal chemistry. 2017;60(19):8201-8217.
195. Keinänen O, Mäkilä EM, Lindgren R, Virtanen H, Liljenbäck H, Oikonen V, Sarparanta M, Molthoff C, Windhorst AD, Roivainen A. Pretargeted PET imaging of trans-cyclooctene-modified porous silicon nanoparticles. ACS omega. 2017;2(1):62-69.
196. Hou S, Choi J-s, Garcia MA, Xing Y, Chen K-J, Chen Y-M, Jiang ZK, Ro T, Wu L, Stout DB. Pretargeted positron emission tomography imaging that employs supramolecular nanoparticles with in vivo bioorthogonal chemistry. ACS nano. 2016;10(1):1417-1424.
197. Locatelli E, Franchini MC. Biodegradable PLGA-b-PEG polymeric nanoparticles: synthesis, properties, and nanomedical applications as drug delivery system. Journal of Nanoparticle Research. 2012;14(12):1316.
198. He J, Zheng N, Xie D, Zheng Y, Song W. Multicomponent polymerization toward biodegradable polymers with diverse responsiveness in tumor microenvironments. Polymer Chemistry. 2020;11(6):1198-1210.
199. Etrych T, Kovář L, Strohalm J, Chytil P, Říhová B, Ulbrich K. Biodegradable star HPMA polymer–drug conjugates: Biodegradability, distribution and anti-tumor efficacy. Journal of controlled release. 2011;154(3):241-248.
200. Mužíková G, Pola R, Laga R, Pechar M. Biodegradable Multiblock Polymers Based on N-(2-Hydroxypropyl) methacrylamide Designed as Drug Carriers for Tumor-Targeted Delivery. Macromolecular Chemistry and Physics. 2016;217(15):1690-1703.
201. Liu DS, Tangpeerachaikul A, Selvaraj R, Taylor MT, Fox JM, Ting AY. Diels–Alder cycloaddition for fluorophore targeting to specific proteins inside living cells. Journal of the American Chemical Society. 2012;134(2):792-795.
202. Golden AL, Battrell CF, Pennell S, Hoffman AS, J. Lai J, Stayton PS. Simple fluidic system for purifying and concentrating diagnostic biomarkers using stimuli-responsive antibody conjugates and membranes. Bioconjugate chemistry. 2010;21(10):1820-1826.
203. Alshehri S, Fan W, Zhang W, Garrison JC. In Vitro Evaluation and Biodistribution Studies of HPMA Copolymers Targeting the Gastrin Releasing Peptide Receptor in Prostate Cancer. Pharmaceutical Research. 2020;37(11):229.
204. Ogbomo SM, Shi W, Wagh NK, Zhou Z, Brusnahan SK, Garrison JC. 177Lu-labeled HPMA copolymers utilizing cathepsin B and S cleavable linkers: synthesis, characterization and

preliminary in vivo investigation in a pancreatic cancer model. Nuclear medicine and biology. 2013;40(5):606-617.

205. Karver MR, Weissleder R, Hilderbrand SA. Synthesis and evaluation of a series of 1, 2, 4, 5-tetrazines for bioorthogonal conjugation. Bioconjugate chemistry. 2011;22(11):2263-2270.

206. Maggi A, Ruivo E, Fissers J, Vangestel C, Chatterjee S, Joossens J, Sobott F, Staelens S, Stroobants S, Van der Veken P. Development of a novel antibody–tetrazine conjugate for bioorthogonal pretargeting. Organic & biomolecular chemistry. 2016;14(31):7544-7551.

207. Selvaraj R, Giglio B, Liu S, Wang H, Wang M, Yuan H, Chintala SR, Yap L-P, Conti PS, Fox JM. Improved metabolic stability for 18F PET probes rapidly constructed via tetrazine trans-cyclooctene ligation. Bioconjugate chemistry. 2015;26(3):435-442.

208. Rahim MK, Kota R, Haun JB. Enhancing reactivity for bioorthogonal pretargeting by unmasking antibody-conjugated trans-cyclooctenes. Bioconjugate chemistry. 2015;26(2):352-360.

209. Pan H, Sima M, Kopečková P, Wu K, Gao S, Liu J, Wang D, Miller SC, Kopecek J. Biodistribution and pharmacokinetic studies of bone-targeting N-(2-hydroxypropyl) methacrylamide copolymer− alendronate conjugates. Molecular pharmaceutics. 2008;5(4):548-558.

210. Rossin R, Läppchen T, Van Den Bosch SM, Laforest R, Robillard MS. Diels–Alder reaction for tumor pretargeting: in vivo chemistry can boost tumor radiation dose compared with directly labeled antibody. Journal of Nuclear Medicine. 2013;54(11):1989-1995.

211. Greiner DL, Hesselton RA, Shultz LD. SCID mouse models of human stem cell engraftment. Stem cells. 1998;16(3):166-177.

212. Greiner DL, Shultz LD, Yates J, Appel MC, Perdrizet G, Hesselton RM, Schweitzer I, Beamer WG, Shultz KL, Pelsue SC. Improved engraftment of human spleen cells in NOD/LtSz-scid/scid mice as compared with CB-17-scid/scid mice. The American journal of pathology. 1995;146(4):888.

213. Ito R, Takahashi T, Katano I, Ito M. Current advances in humanized mouse models. Cellular & molecular immunology. 2012;9(3):208-214.

214. Piganelli JD, Martin T, Haskins K. Splenic macrophages from the NOD mouse are defective in the ability to present antigen. Diabetes. 1998;47(8):1212-1218.

215. Sadekar S, Ray A, Janat-Amsbury M, Peterson C, Ghandehari H. Comparative biodistribution of PAMAM dendrimers and HPMA copolymers in ovarian-tumor-bearing mice. Biomacromolecules. 2011;12(1):88-96.

216. Ding H, Kopečková P, Kopeček J. Self-association properties of HPMA copolymers containing an amphipathic heptapeptide. Journal of drug targeting. 2007;15(7-8):465-474.

217. McClellan RO. Health effects of nuclear weapons and releases of radioactive materials. In. Handbook of Toxicology of Chemical Warfare Agents: Elsevier; 2020. p. 707-743.

218. Blanusa M, Varnai VM, Piasek M, Kostial K. Chelators as antidotes of metal toxicity: therapeutic and experimental aspects. Current medicinal chemistry. 2005;12(23):2771-2794.

219. Abergel RJ. Chelation of Actinides. Chapter 6. In.: Lawrence Berkeley National Lab.(LBNL), Berkeley, CA (United States); 2017.

220. Ménétrier F, Grappin L, Raynaud P, Courtay C, Wood R, Joussineau S, List V, Stradling G, Taylor D, Bérard P. Treatment of accidental intakes of plutonium and americium: guidance notes. Applied radiation and isotopes. 2005;62(6):829-846.

221. Kang CS, Chen Y, Dadachova E, Chong H-S. Evaluation of benzyl-substituted DTPA analogues as decorporation agents of radionuclides. Journal of Radioanalytical and Nuclear Chemistry. 2015;303(3):2407-2411.

222. Lahrouch F, Siberchicot B, Fèvre J, Leost L, Aupiais J, Solari PL, Den Auwer C, Di Giorgio C. Carboxylate-and Phosphonate-Modified Polyethylenimine: Toward the Design of Actinide Decorporation Agents. Inorganic Chemistry. 2019;59(1):128-137.

223. Phan G, Le Gall B, Grillon G, Rouit E, Fouillit M, Benech H, Fattal E, Deverre J-R. Enhanced decorporation of plutonium by DTPA encapsulated in small PEG-coated liposomes. Biochimie. 2006;88(11):1843-1849.

224. Phan G, Herbet A, Cholet S, Benech H, Deverre J-R, Fattal E. Pharmacokinetics of DTPA entrapped in conventional and long-circulating liposomes of different size for plutonium decorporation. Journal of controlled release. 2005;110(1):177-188.

225. Chen S. Improving Decorporation Efficacy of DTPA and HOPO Using Chitosan/TPP Nanoparticles: Preparation, Characterization and Release Testing. In.: Carleton University; 2016.

226. Pelaz B, Alexiou C, Alvarez-Puebla RA, Alves F, Andrews AM, Ashraf S, Balogh LP, Ballerini L, Bestetti A, Brendel C, Bosi S, Carril M, Chan WCW, Chen C, Chen X, Chen X, Cheng Z, Cui D, Du J, Dullin C, Escudero A, Feliu N, Gao M, George M, Gogotsi Y, Grünweller A, Gu Z, Halas NJ, Hampp N, Hartmann RK, Hersam MC, Hunziker P, Jian J, Jiang X, Jungebluth P, Kadhiresan P, Kataoka K, Khademhosseini A, Kopeček J, Kotov NA, Krug HF, Lee DS, Lehr C-M, Leong KW, Liang X-J, Ling Lim M, Liz-Marzán LM, Ma X, Macchiarini P, Meng H, Möhwald H, Mulvaney P, Nel AE, Nie S, Nordlander P, Okano T, Oliveira J, Park TH, Penner RM, Prato M, Puntes V, Rotello VM, Samarakoon A, Schaak RE, Shen Y, Sjöqvist S, Skirtach AG, Soliman MG, Stevens MM, Sung H-W, Tang BZ, Tietze R, Udugama BN, VanEpps JS, Weil T, Weiss PS, Willner I, Wu Y, Yang L, Yue Z, Zhang Q, Zhang Q, Zhang X-E, Zhao Y, Zhou X, Parak WJ. Diverse Applications of Nanomedicine. ACS Nano. 2017;11(3):2313-2381.

227. Říhová B, Kovář M. Immunogenicity and immunomodulatory properties of HPMA-based polymers. Advanced drug delivery reviews. 2010;62(2):184-191.

228. Seymour L, Duncan R, Strohalm J, Kopeček J. Effect of molecular weight (M w) of N-(2-hydroxypropyl) methacrylamide copolymers on body distribution and rate of excretion after subcutaneous, intraperitoneal, and intravenous administration to rats. Journal of biomedical materials research. 1987;21(11):1341-1358.

229. Liu X-M, Miller SC, Wang D. Beyond oncology—application of HPMA copolymers in non-cancerous diseases. Advanced drug delivery reviews. 2010;62(2):258-271.

230. Smith RM, Martell AE. Critical stability constants, enthalpies and entropies for the formation of metal complexes of aminopolycarboxylic acids and carboxylic acids. Science of the total environment. 1987;64(1-2):125-147.

231. Mitra A, Nan A, Papadimitriou JC, Ghandehari H, Line BR. Polymer-peptide conjugates for angiogenesis targeted tumor radiotherapy. Nuclear medicine and biology. 2006;33(1):43-52.

232. Kratz A, Ferraro M, Sluss PM, Lewandrowski KB. Laboratory reference values. New England Journal of Medicine. 2004;351:1548-1564.

233. Watanabe S, Hashimoto K, Ishioka NS. Lutetium-177 complexation of DOTA and DTPA in the presence of competing metals. Journal of Radioanalytical and Nuclear Chemistry. 2015;303(2):1519-1521.

234. Vora MM. HPLC analysis of indium-111 diethylenetriaminepentaacetic acid (111In-DTPA) radiopharmaceutical. International journal of radiation applications and instrumentation Part A Applied radiation and isotopes. 1991;42(1):19-24.

235. Fan W, Zhang W, Alshehri S, Neeley TR, Garrison JC. Enhanced tumor retention of NTSR1-targeted agents by employing a hydrophilic cysteine cathepsin inhibitor. European journal of medicinal chemistry. 2019;177:386-400.

236. Lloyd RD, Taylor GN, Mays CW, Jones CW, Bruenger FW, Atherton DR. Dependency of chelation efficacy upon time after first DTPA injection. Radiation research. 1979;78(3):448-454.

237. Sueda K, Sadgrove MP, Jay M, Di Pasqua AJ. Species-dependent effective concentration of DTPA in plasma for chelation of 241Am. Health physics. 2013;105(2):208.

238. Brechbiel MW, Gansow OA. Backbone-substituted DTPA ligands for yttrium-90 radioimmunotherapy. Bioconjugate chemistry. 1991;2(3):187-194.

239. Pandey U, Gamre N, Lohar SP, Dash A. A systematic study on the utility of CHX-A''-DTPA-NCS and NOTA-NCS as bifunctional chelators for 177Lu radiopharmaceuticals. Applied Radiation and Isotopes. 2017;127:1-6.
240. Camera L, Kinuya S, Garmestani K, Wu C, Brechbiel MW, Pai LH, McMurry TJ, Gansow OA, Pastan I, Paik CH. Evaluation of the serum stability and in vivo biodistribution of CHX-DTPA and other ligands for yttrium labeling of monoclonal antibodies. Journal of nuclear medicine. 1994;35(5):882-889.
241. Chong H-S, Milenic DE, Garmestani K, Brady ED, Arora H, Pfiester C, Brechbiel MW. In vitro and in vivo evaluation of novel ligands for radioimmunotherapy. Nuclear medicine and biology. 2006;33(4):459-467.
242. Barta P, Laznickova A, Laznicek M, Vera DRB, Beran M. Preclinical evaluation of radiolabelled nimotuzumab, a promising monoclonal antibody targeting the epidermal growth factor receptor. Journal of Labelled Compounds and Radiopharmaceuticals. 2013;56(5):280-288.
243. Perk LR, Visser GW, Vosjan MJ, Stigter-van Walsum M, Tijink BM, Leemans CR, Van Dongen GA. 89Zr as a PET surrogate radioisotope for scouting biodistribution of the therapeutic radiometals 90Y and 177Lu in tumor-bearing nude mice after coupling to the internalizing antibody cetuximab. Journal of Nuclear Medicine. 2005;46(11):1898-1906.
244. Cao Y, Gong Y, Liu L, Zhou Y, Fang X, Zhang C, Li Y, Li J. The use of human umbilical vein endothelial cells (HUVECs) as an in vitro model to assess the toxicity of nanoparticles to endothelium: a review. Journal of Applied Toxicology. 2017;37(12):1359-1369.
245. Lucke-Huhle C. Proliferation-dependent cytotoxicity of diethylenetriaminepentaacetate (DTPA) in vitro. Health physics. 1976;31(4):349-354.
246. Pissuwan D, Boyer C, Gunasekaran K, Davis TP, Bulmus V. In vitro cytotoxicity of RAFT polymers. Biomacromolecules. 2010;11(2):412-420.
247. Grappin L, Bérard P, Ménétrier F, Carbone L, Courtay C, Castagnet X, Le Goff J, Néron M, Beau P, Piechowski J. Exposure to actinides: report on Ca-DTPA injections in CEA-AREVA centres. Radioprotection. 2007;42(2):163-196.
248. Mitra A, Coleman T, Borgman M, Nan A, Ghandehari H, Line BR. Polymeric conjugates of mono-and bi-cyclic αVβ3 binding peptides for tumor targeting. Journal of controlled release. 2006;114(2):175-183.
249. Grémy O, Laurent D, Coudert S, Griffiths NM, Miccoli L. Decorporation of Pu/Am actinides by chelation therapy: new arguments in favor of an intracellular component of DTPA action. Radiation research. 2016;185(6):568-579.
250. Quan L-d, Yuan F, Liu X-m, Huang J-g, Alnouti Y, Wang D. Pharmacokinetic and biodistribution studies of N-(2-hydroxypropyl) methacrylamide copolymer-dexamethasone conjugates in adjuvant-induced arthritis rat model. Molecular pharmaceutics. 2010;7(4):1041-1049.
251. Wei X, Li F, Zhao G, Chhonker YS, Averill C, Galdamez J, Purdue PE, Wang X, Fehringer EV, Garvin KL. Pharmacokinetic and biodistribution studies of HPMA copolymer conjugates in an aseptic implant loosening mouse model. Molecular pharmaceutics. 2017;14(5):1418-1428.
252. Julyan PJ, Seymour LW, Ferry DR, Daryani S, Boivin CM, Doran J, David M, Anderson D, Christodoulou C, Young AM. Preliminary clinical study of the distribution of HPMA copolymers bearing doxorubicin and galactosamine. Journal of controlled release. 1999;57(3):281-290.
253. Rahman Y-E, Rosenthal MW, Cerny EA. Intracellular plutonium: removal by liposome-encapsulated chelating agent. Science. 1973;180(4083):300-302.
254. Sahay G, Alakhova DY, Kabanov AV. Endocytosis of nanomedicines. Journal of controlled release. 2010;145(3):182-195.
255. Boocock G, Danpure C, Popplewell D, Taylor D. The subcellular distribution of plutonium in rat liver. Radiation Research. 1970;42(2):381-396.

256. Gruner R, Seidel A, Winter R. The initial early distribution of monomeric 239Pu and 241Am in rat liver as determined by Triton WR 1339 injection. Radiation Research. 1981;85(2):367-379.

257. Seidel A, Wiener M, Krüger E, Wirth R, Haffner H. Studies on the lysosomal binding of 141Ce, 239Np, 239Pu and 241Am in rat and Syrian hamster liver using carrier-free electrophoresis. International Journal of Radiation Applications and Instrumentation Part B Nuclear Medicine and Biology. 1986;13(5):515-518.

258. Müller W, Linzner U, Schäffer E. Organ distribution studies of lutetium-177 in mouse. International journal of nuclear medicine and biology. 1978;5(1):29-31.

259. Nakamura Y, Tsumura Y, Tonogai Y, Shibata T, Ito Y. Differences in behavior among the chlorides of seven rare earth elements administered intravenously to rats. Toxicological Sciences. 1997;37(2):106-116.

260. Müller W, Schäffer E, Linzner U. Studies on incorporated short-livedβ-emitters with regard to the induction of late effects. Radiation and Environmental Biophysics. 1980;18(1):1-11.

261. Borgman MP, Coleman T, Kolhatkar RB, Geyser-Stoops S, Line BR, Ghandehari H. Tumor-targeted HPMA copolymer-(RGDfK)-(CHX-A ″-DTPA) conjugates show increased kidney accumulation. Journal of Controlled Release. 2008;132(3):193-199.

262. Liu GW, Prossnitz AN, Eng DG, Cheng Y, Subrahmanyam N, Pippin JW, Lamm RJ, Ngambenjawong C, Ghandehari H, Shankland SJ. Glomerular disease augments kidney accumulation of synthetic anionic polymers. Biomaterials. 2018;178:317-325.

263. Tang S, Meng Q, Sun H, Su J, Yin Q, Zhang Z, Yu H, Chen L, Gu W, Li Y. Dual pH-sensitive micelles with charge-switch for controlling cellular uptake and drug release to treat metastatic breast cancer. Biomaterials. 2017;114:44-53.

264. Du J-Z, Li H-J, Wang J. Tumor-acidity-cleavable maleic acid amide (TACMAA): a powerful tool for designing smart nanoparticles to overcome delivery barriers in cancer nanomedicine. Accounts of Chemical Research. 2018;51(11):2848-2856.

265. Cao B, Tang Q, Cheng G. Recent advances of zwitterionic carboxybetaine materials and their derivatives. J Biomater Sci Polym Ed. 2014;25(14-15):1502-1513.

266. Estephan ZG, Schlenoff PS, Schlenoff JB. Zwitteration as an alternative to PEGylation. Langmuir. 2011;27(11):6794-6800.

267. Wang M, Svatunek D, Rohlfing K, Liu Y, Wang H, Giglio B, Yuan H, Wu Z, Li Z, Fox J. Conformationally strained trans-cyclooctene (sTCO) enables the rapid construction of 18F-PET probes via tetrazine ligation. Theranostics. 2016;6(6):887.

268. Darko A, Wallace S, Dmitrenko O, Machovina MM, Mehl RA, Chin JW, Fox JM. Conformationally strained trans-cyclooctene with improved stability and excellent reactivity in tetrazine ligation. Chemical science. 2014;5(10):3770-3776.